ISTANBUL TECHNICAL UNIVERSITY ★ GRADUATE SCHOOL OF SCIENCE
ENGINEERING AND TECHNOLOGY

DESIGN OF MOBILITY, MANIPULATION AND VISION SYSTEM OF A CONCEPTUAL LUNAR MICRO-ROVER

M.Sc. THESIS

Necmi Cihan ÖRGER

Department of Aeronautical and Astronautical Engineering

Aeronautics and Astronautics Engineering Programme

Thesis Advisor: Assist. Prof. Dr. Turgut Berat KARYOT

JANUARY 2015

ISTANBUL TECHNICAL UNIVERSITY ★ GRADUATE SCHOOL OF SCIENCE ENGINEERING AND TECHNOLOGY

DESIGN OF MOBILITY, MANIPULATION AND VISION SYSTEM OF A CONCEPTUAL LUNAR MICRO-ROVER

M.Sc. THESIS

Necmi Cihan ÖRGER

511121214

Department of Aeronautical and Astronautical Engineering

Aeronautics and Astronautics Engineering Programme

Thesis Advisor: Assist. Prof. Dr. Turgut Berat KARYOT

JANUARY 2015

İSTANBUL TEKNİK ÜNİVERSİTESİ ★ FEN BİLİMLERİ ENSTİTÜSÜ

GEZİCİ MİKRO AY ROBOTUNUN HAREKETLİLİK, MANİPÜLASYON VE GÖRÜNTÜ İŞLEME SİSTEMLERİ TASARIMI

YÜKSEK LİSANS TEZİ

Necmi Cihan ÖRGER

511121214

Uçak ve Uzay Mühendisliği Anabilim Dalı

Uçak ve Uzay Mühendisliği Programı

Tez Danışmanı: Yrd.Doç.Dr. Turgut Berat Karyot

OCAK 2015

Necmi Cihan Örger, a M.Sc. student of ITU Aeronautics and Astronautics Engineering Programme of Graduate School Of Science Engineering and Technology Student ID 511121214, successfully defended the thesis entitled "**DESIGN OF MOBILITY, MANIPULATION AND VISION SYSTEM OF A CONCEPTUAL LUNAR MICRO-ROVER**", which he prepared after fulfilling the requirements specified in the associated legislations, before the jury whose signatures are below.

Thesis Advisor: **Assist. Prof. Dr. Turgut Berat KARYOT** ....
Istanbul Technical University

Jury Members: **Prof. Dr. Zerefşan KAYMAZ** ....
Istanbul Technical University

Prof. Dr. Hakan TEMELTAŞ ....
Istanbul Technical University

Date of Submission: 15 December 2014

Date of Defense: 21 January 2015

To my mother and sister,

FOREWORD

I would like to begin with expressing my deepest gratitude to my thesis advisor Assoc. Prof. Dr. Turgut Berat Karyot for his guidance, support and understanding throughout this study. Thanks to his support, I got an opportunity to expand my vision and knowledge in robotics.

I want to thank Prof. Dr. Zerefşan Kaymaz for her encouragements, guidance and support throughout my master study. I would also like to thank my beloved friend Yiğit Çay for his encouragements, advices and continuous help for whole the time being.

At last but not least, I thank my only parent, my mother and my sister for being a great source of energy and motivation.

January 2015 Necmi Cihan ÖRGER

TABLE OF CONTENTS

Page

FOREWORD ... **ix**
TABLE OF CONTENTS ... **xi**
ABBREVIATIONS ... **xiii**
LIST OF TABLES ... **xv**
LIST OF FIGURES ... **xvii**
SUMMARY ... **xix**
ÖZET ... **xxiii**
1. INTRODUCTION ... **27**
  1.1 The Definition of a Robot ... 27
  1.2 Space Robotics ... 28
  1.3 History of Rovers ... 30
  1.4 Lunar Micro-Rover ... 33
2. LUNAR ENVIRONMENT ... **35**
  2.1 Introduction ... 35
  2.2 Mission Proposal ... 36
  2.3 Lunar Dust and Plasma Environment ... 38
  2.4 Lunar Radiation Environment ... 42
3. LUNAR MICRO-ROVER PROTOTYPE DESIGN ... **45**
  3.1 Introduction ... 45
  3.2 Design Progress ... 46
  3.3 Mobility System ... 50
  3.4 Conclusion ... 56
4. ROBOTIC MANIPULATOR ARM ... **57**
  4.1 Structural and Mechanical Design ... 57
  4.2 Modeling of Robotic Manipulator Arm ... 59
    4.2.1 Forward Kinematics ... 60
    4.2.2 Robotic Manipulator Arm Pose Examples ... 62
    4.2.3 Trajectory Calculation ... 64
  4.3 Spatial Operator Algebra for Manipulator Modeling ... 66
    4.3.2 Calculation of Torques and Forces ... 74
  4.4 Conclusion ... 77
5. ENVIRONMENT RECOGNITION AND PATH PLANNING ... **79**
  5.1 Image Processing ... 79
  5.2 Triangulation ... 81
    5.2.1 Introduction ... 81
    5.2.2 Laser Triangulation ... 82
  5.3 Active Laser Triangulation System ... 82
    5.3.1 Formulization ... 85
    5.3.2 Surface Mapping ... 90
  5.4 Path Planning ... 92
    5.4.1 Introduction ... 92

5.4.2 Path Planning Algorithm Selection 93
5.5 Conclusion 102
6. CONCLUSION AND RECOMMENDATIONS 105
REFERENCES 109
CURRICULUM VITAE.. 113

ABBREVIATIONS

LRO	**:** Lunar Reconnaissance Orbiter
IMA	**:** Ion Mass Analyzer
DDE	**:** Dust Detector Experiment
SWP	**:** Solar Wind Particle
GCR	**:** Galactic Cosmic Ray
SEP	**:** Solar Energetic Proton
DH	**:** Denavit-Hartenberg

LIST OF TABLES

Page

Table 2.1 : Physical Properties of the Moon. 38
Table 4.1 : The Predicted Mass of the Robotic Arm Structural. 59
Table 4.2 : The DH Parameters Table of the Arm...62
Table 5.1 : Hazard Detection Types...83
Table 6.1 : Comparison of Greedy Search and A* Search Algorithms. 99

LIST OF FIGURES

Page

Figure 1.1 : A general representation of a robotic system……….………..…….27
Figure 1.2 : A Mars exploration rover (Image courtesy NASA)…...……………..29
Figure 1.3 : A robotic manipulator arm on Mars exploration rover……………...30
Figure 1.4 : Lunokhod 1 (Image courtesy NASA)...………………………………31
Figure 1.5 : NASA - JPL Sojourner Rover (Courtesy of NASA/JPL-Caltech)……32
Figure 1.6 : Mars rovers Spirit and Opportunity (Courtesy of NASA/JPL)……..…32
Figure 1.7 : Curiosity and previous rovers……………………………………....32
Figure 2.1 : The view of full Moon…….…………………………………………35
Figure 2.2 : Young volcanic rock deposits (Image courtesy NASA/GSFC/Arizona State University)……….…………………………………………….36
Figure 2.3 : Lunar rock sample example…..……………………………………...37
Figure 2.4 : Lunar crater example……...……………..…………………………...37
Figure 2.5 : Lunar dust and plasma environment (Image courtesy NASA)……....39
Figure 2.6 : Lunar orbit (Image courtesy NASA)……………………………….....41
Figure 2.7 : Lunar dust………..…………………………………………………42
Figure 3.1 : Cad drawing of lunar micro-rover design..……………………….…45
Figure 3.2 : Cad drawing of lunar micro-rover design 01…………...……………47
Figure 3.3 : Cad drawing of lunar micro-rover design 02……………………..…47
Figure 3.4 : Cad drawing of lunar micro-rover design 03……………………..…48
Figure 3.5 : 1U CubeSat example………………………………………………....48
Figure 3.6 : The final dimensions of lunar micro-Rover..………………………..49
Figure 3.7 : The suspension mechanism of LMR without wheels………………...50
Figure 3.8 : Cad drawing of the wheels…………………………………………...51
Figure 3.9 : Cad drawing of the LMR without the wheels………………………..51
Figure 3.10 : The distance between the rotational axis of the wheels……………52
Figure 3.11 : Hybrid bipolar stepping motor……………………………………...53
Figure 3.12 : Stepping motor dimensions in mm…………………………………54
Figure 3.13 : Stepping motor diagram…….………………………………………54
Figure 3.14 : Stepper motor driver. ………………………………………………55
Figure 3.15 : Terrain wheel for the LMR prototype………………………………55
Figure 3.16 : The battery of the LMR……………………………………………...56
Figure 4.1 : Robotic manipulator arm closed pose………………………………58
Figure 4.2 : Robotic manipulator arm assembly exploded view……………….58
Figure 4.3: Robotic manipulator arm tip tool design……………………………59
Figure 4.4: The axis assignment of the robotic arm with handling mechanism..62
Figure 4.5 : Ready state pose of the robotic arm in Robotic Toolbox…………63
Figure 4.6 : Sample retrieval pose of the robotic arm in Robotic Toolbox.……63
Figure 4.7 : Storing the rock sample of the robotic arm in Robotic Toolbox..64
Figure 4.8 : The positions of each joint……………………………….…………..65
Figure 4.9 : The velocities of each joint…………………………….……………66
Figure 4.10 : The accelerations of each joint…………………………...………66

Figure 4.11 : The representation for the differentiation of a vector……...………...69
Figure 4.12 : The representation of a link..……………………...…….…….....69
Figure 4.13 : The representation of a link..……………………..………..……73
Figure 4.14 : Simulink model of the robotic manipulator system……..…………..75
Figure 4.15 : Torques for each link with lunar gravity…………….………………75
Figure 4.16 : Torques for each link with gravity of Earth……..……………………..76
Figure 4.17 : Virtual Reality screenshot in Matlab. …………………………..……76
Figure 5.1 : Compressed rock image………………………………...………..79
Figure 5.2 : Rock sample example and image Processing……………....………80
Figure 5.3 : Triangulation configuration………………………………...……….81
Figure 5.4 : Active laser triangulation system on LMR……………………………83
Figure 5.5 : Obstacle detection by active laser triangulation….…………….……..84
Figure 5.6 : Top view of active laser triangulation system…………………...………84
Figure 5.7 : Hazard detection configuration……………….…………...……….85
Figure 5.8 : Hazard detection configuration………………………….………….86
Figure 5.9 : Hazard detection configuration and parameters…………….………..87
Figure 5.10 : Hazard detection and mapping algorithm flowchart………..…..……88
Figure 5.11 : Rough laser stripe emitting on the scene.……..……....……..………88
Figure 5.12 : Rough hollow detection example on the scene………….……………89
Figure 5.13 : Rough elevation detection example…..…………….……………89
Figure 5.14 : 15 x 15 gridded main map example……………………….…………90
Figure 5.15 : 30 x 30 gridded main map example……………………….…………90
Figure 5.16 : Main map updating representation…………………….…………91
Figure 5.17 : The future path-cost function representation…………………..……94
Figure 5.18 : 3D map example for obstacle and hollow……………….……….……95
Figure 5.19 : The detected nodes of hollow for possible hazards………….………..96
Figure 5.20 : Extended nodes of hollow for possible hazards…………...……..96
Figure 5.21 : The first algorithm with greedy search…………………….……….97
Figure 5.22 : Path planning and mapping algorithm flowchart……………………97
Figure 5.23 : A* search algorithm between two points without any obstacles..…99
Figure 5.24 : A* search algorithm between two points with obstacles…………100
Figure 5.25 : A* search algorithm between two points with denser obstacles…...100
Figure 5.26 : A* search algorithm for unreachable goal destination………..……..101
Figure 5.27 : A* search algorithm task example……..…………………………..101
Figure 5.28 : A* search algorithm task example……..…………………………..102

DESIGN OF MOBILITY, MANIPULATION AND VISION SYSTEM OF A CONCEPTUAL LUNAR MICRO-ROVER

SUMMARY

The research area for the lunar micro-rovers (LMR) is very extensive such as navigation, obstacle avoidance, path planning, rover platform design, field-testing, motion kinematics, slip models, and so on. Since there was no rover platform to work on within our faculty, the project started with designing a micro-rover platform to implement and test certain technologies not only during this project but during future projects as well. Therefore, the thesis presents a simple and versatile rover platform.

According to the future missions, the geology of the Moon, potential resources and the distribution of them are gaining attention internationally since the Moon itself is an important planetary body for exploration by both human and robotic missions. For this reason, lunar micro-rovers must be designed to make scientific research, which can support these missions by investigating the lunar environment and mission parameters. Multiple scientific areas such as planetary sciences and geology, plasma physics, astrobiology, astronomy, space science will be benefiting from the scientific outcomes of the future lunar missions. Therefore, performing scientific researches with an LMR and addressing multiple scientific goals are essential objectives.

Landing on the lunar surface can be expressed as another challenge; however, it is not one of the topics of this project. Many studies suggest orbital missions need to be coupled with surface investigations in order to validate the interpretation of data sets. In addition, surface data will show suitability for manned missions as well as validity of the models on the significant surface characteristics.

The mission is proposed to land on a determined area in South Polar region of the Moon since longer periods of solar illumination is available by reason of the low sun inclination is coupled with topographic highs. The main objective is to obtain a surface sample from the Moon and store it within the micro-rover to study in mini-laboratory, which is expected to be on the top of the LMR. The sample is desired to have a volume between 1-3 cm^3; therefore, the robotic arm tool is designed based on a handling mechanism with a surface geometry, which enables to tip tool grab a solid rock sample from the ground; however, this tool can also be replaced with a drill mechanism for subsurface sampling. The main interest of the research is chosen as investigating the ejecta areas on the lunar surface containing both meteor samples as well as Moon’s own material. The rover must be able to move to points of interest to make measurements with its onboard instruments and transmit data.

An LMR must be lightweight with high mobility, resistant to high radiation, extreme temperature variations, lunar dust etc. In design process, the most important considerations were mobility and weight limitations. The mass and inertia properties are derived from Solidworks after material selection. Most of the time in an LMR, power is generated using the solar panels and stored in the batteries while onboard computer would be performing multiple task and the reset capability in emergencies. All subsystems of LMR have to be protected from high radiation, vacuum and extreme temperature variance. First, a small lightweight rover provides significant savings in the launch and lunar landing thruster capabilities; therefore, size and weight have to be limited. For this reason, there is not enough room for complex ideas, so everything must be as simple as possible. In addition, the energy limitations require actuators to be chosen those consume very little power since there will be limited electrical power from solar panels. Lunar surface temperature varies from -240^{o}C at night to 121^{o}C during the day, and micro-rover will be operating in micro gravity environment. Onboard computer and battery is expected to keep the electronics warm in order to operate in that low temperature. The body structure is designed to have low volume; however, it must provide sufficient space for the onboard computer, scientific instruments, actuators, cameras, sensors etc.

The uneven lunar surface requires LMR to sense the obstacles as well as other hazards in order to get closer to the crater region, and it must be able to identify interesting sample candidates during the motion. Therefore, the primary technologies to be implemented within the LMR are chosen as local mapping, manipulation and sample handling, and path planning. The surface sampling activities will be commanded from Earth during the communication windows while the instruments within the mini laboratory analyze samples, and data of the environmental properties such as radiation, ionization, temperature will be gathered as well. The formal mission lifetime is expected to be couple of months if the LMR survives the lunar night that is approximately 13 days. The first phase of the mission will contain primary scientific activities and measurements before the lunar night period; therefore, if the LMR does not survive the lunar night, it will gather and transmit data before it malfunctions.

At the beginning, the design of the lunar micro-rover is chosen as a 6-wheel system with a rocker-bogie suspension that has a mechanism as passive rotary joint to attach two links called rocker and bogie. As wheels are free to move up and down on an uneven terrain with the rotary joint, each wheel carry the weight of the LMR equally, but it is much heavier than a 4-wheeled suspension, and each extra actuator means more energy consumption and higher hardware requirements.

By only giving input for the links' motions, the joints' torques are derived for the given system, and for the poses, which robotic manipulators cannot reach, the singularity of the Jacobian matrix is observed. The computational complexity of each iteration remained constant, and it grows in a linear fashion with the number of joints increases. In addition, a closed-form dynamic model is obtained which is the same as the one obtained by using DH parameters.

The inertia tensor matrix shows all mass and inertial properties of the robotic system, and it is very important to be derived for understanding the dynamics of the system since the inertia of the manipulator has to be surpassed in order to move the links. Therefore, the effect of Moon and Earth's gravity ratio is observed in the torques. Since the robotic arms' motion is determined to be slow, Coriolis Effect is not strong. Moreover, the profiles of the both torque graphs seem to be very similar; however, the magnitude of the torque's ratio is very close to the ratio of the gravity, which is approximately 1/6.

Active laser triangulation system operates by sensing the reflected red laser light from a surface; however, the ambient light variations and the reflectance properties of different surfaces are the main challenges of this system. The ambient light variations can be overcome by using optical filters according to the wavelength of the laser emitter to be used in outdoor environments more accurately. In addition, active laser triangulation system is desired to be low-cost, low power consuming while having high response speed and high sampling frequency, and it will be used for detecting hazards and mapping the rough terrain. In addition, a passive triangulation system such as stereo-based planner is a reliable choice, and it will be added to the LMR in the future; however, it cannot detect craters and shadow areas.

When the LMR uses its active laser triangulation system and captures a new image, the LMR's field of view is updated in the image space. The information of outside of the LMR's field of view is kept in memory, and the map data are implemented in the algorithm as 2D grid that shows the coordinates of the nodes and the height values corresponding to those nodes. Then, the updated image space is used to renew 3D main map. The LMR's field of view will be updated on the main map, and the rest information will be preserved in the memory unchanged. If the captured image is used to create a local map, and then it is used to update the current map, the new nodes cannot match the main map's nodes exactly. Therefore, the image space must be updated first in mm metric, and then the main 3D map must be updated.

Finally, greedy search algorithm and A* search algorithm are implemented in the main algorithm to compare their path planning performance. Different tasks are given to the path planning algorithms, and if there are no obstacles or hollows, which the robot cannot overcome, both algorithms found the reasonable path. On the other hand, the complication level is increased for the tasks, and A* search algorithm found the optimal path each time, if it exists at all. Therefore, A* search is chosen as the path planning algorithm instead of greedy search. The next step for this project is to build prototype for verification of the performance and to have a micro-rover platform to work on within our faculty.

GEZİCİ MİKRO AY ROBOTUNUN HAREKETLİLİK, MANİPÜLASYON VE GÖRÜNTÜ İŞLEME SİSTEMLERİ TASARIMI

ÖZET

Ay, Mars ve diğer gökcisimleri üzerindeki yüzey keşifleri, gün geçtikçe bilimsel açıdan önem kazanmaktadır. Jeolojik olarak ilgi çekici bölgelerde araştırma yapılması, gelecekte yapılması planlanan insanlı görevler gibi birçok bilimsel çalışma için katkı sağlamaktadır. Ayrıca, gezici mikro uzay robotu araştırma ve geliştirme çalışmaları son yıllarda birçok araştırma kurumunda yaygın bir şekilde gerçekleştirilmektedir. İnsanlı görevler ile karşılaştırıldığında robotik görevler birçok avantaj sağlamakla birlikte, robotların insanlı görevlerde yardımcı etmen olarak kullanılması öngörülmektedir. Bu çalışmada mikro boyutlarda olan hafif bir gezici Ay robot platformu tasarımı önerilmiştir.

Çalışmanın hedefi, Ay yüzeyindeki kraterler etrafında çarpışma sonrası oluşan dışa atım bölgelerinde araştırma yapabilecek bir aracın yüzeyden örnek alabilmesini sağlayacak manipülatörünün ve genel olarak aracın kendisinin tasarımının yapılmasıdır. Bir gezici mikro robot platformu tasarlandıktan sonra küçük değişiklikler yapılarak farklı görevlere uyarlanabilirliği, özgün tasarım tamamlandıktan sonra hızlı ve daha ucuz şekilde tekrar üretilebilirliği, fırlatma ve yere inişinin daha kolay yapılabilmesi gibi birçok avantaja sahiptir. Bu özellikteki mikro robotlar, grup halinde saha çalışması yaptıklarında daha yüksek oranda veri toplama ve daha karmaşık davranışlar sergileyerek daha zor görevleri tamamlayabilme özelliklerine sahiptir.

Ön tasarım aşamasında, gezici mikro robotun süspansiyon sistemi öndeki iki tekerleği döner bir ekleme bağlı olan altı tekerlekli bir yapı olarak öngörülmüştür, ancak bu boyutlardaki mikro bir aracın ağırlık ve enerji kısıtlamaları göz önüne alındığında daha hafif olan dört tekerlekli bir tasarıma geçilmiştir. Bu sayede her bir tekerleği dönme hareketi ile yönelimini değiştirebilen, sekiz hareketlilik derecesine sahip bir süspansiyon sistemi tasarlanmıştır. Bu tipte bir mikro robot, pozisyonunu değiştirmeden kendi etrafında dönerek yönelimini değiştirebilmekte, daha keskin açılı dönüşler yapabilmekte ve engeller etrafında daha rahat hareket edebilmektedir.

Tasarımı yapılan aracın süspansiyon sistemi hareket kabiliyeti konusundaki en önemli etmenlerinden biridir, bu yüzden tasarım sırasında tekerlekli sistemler gibi diğer mekanik sistemler de göz önünde bulundurulmuştur. Ancak, tekerlekli sistemler basit ve gelişmiş bir teknoloji olup, daha hafif ve düz yüzeyler üzerinde daha yüksek hızlarda yol alma kabiliyetine sahiptir. Ayrıca, daha düşük enerji tüketimine sahip olduğu gibi daha yüksek faydalı yük/mekanizma ağırlığı oranı sağlamaktadır. Dezavantaj olarak, tekerleklerin kaymasından kaynaklanan daha düşük tırmanma açısı ve yüksek engelleri aşamama gösterilebilir.

Gezici robotun ana görevi, keşif yaptığı alandaki yüzey örneklerini görsel olarak tanımlamak ve ardından robotik manipülatör kolunu kullanarak hacim ve kütle özellikleri uygun örnekleri gövdesinde bulunan hazneye aktarıp, bilimsel inceleme için saklamaktır. Yüzeyden alınan her bir örneğin 1-3 cm^3 arasında hacme sahip olması öngörülmektedir, bu yüzden robot kolunun uç organı yüzeye uzatıldığında yerden katı bir örneği mekanizması ile kavrayabilecek şekilde tasarlanmıştır. Robot manipülatör kolunun Solidworks kullanılarak 3 boyutlu çizimi, uç organ tasarımı, malzeme seçimi ve Denavit Hartenberg parametrelerinin belirlenmesinin ardından, robotun kinematik incelemesi yapılmış; dinamik modeli Matlab/Simulink üzerinde kurularak Ay çekimi ve yerçekimi değerleri kullanılarak eklemler üzerindeki torkların karşılaştırılması sunulmuştur. Yörüngelerin atanmasında beşince dereceden polinomlar kullanılarak hareketler sırasında eklemlerin titreşimi minimum seviyede tutulmaya özen gösterilmiştir. Hareketlerin görselleştirilmesi açısından Matlab Virtual Reality Toolbox'tan yararlanılmış, bu sayede tüm yörüngelerin görsel olarak da doğrulaması gerçekleştirilmiştir.

İlk çalışmalarda yüzeydeki kaya örnekleri, robot üzerindeki kamera ile alınan siyah beyaz görüntüler kullanılarak algılanabilmesi amaçlanmıştır. Öncelikle, yazılım kaya görüntülerini kullanarak histogramındaki dağılıma göre ayarlamalar yapmakta, böylece örnekteki kayanın karanlık olan yan yüzeyinin de gölge olarak algılanması önlenmektedir. Diğer bir sorun da Ay yüzeyindeki küçük gölge alanlarıdır, bu yüzden sisteme bu alanları temizlemek üzere bir filtre yazılmıştır. Güneş ışınlarının geliş açısı, gölgenin boyutları ve kameranın bakış açısı kullanılarak kayanın boyutuna ve (eğer örnek olarak alınacaksa) robot kolunun yüzeye yaklaşma açısına karar verilebilmesi amaçlanmıştır. Bu sistemin ana problemi, çukurların içindeki karanlık bölgelerle kayalar gibi yükseltilerden kaynaklanan gölgeleri birbirinden ayıramaması olarak gözlenmiştir. Bu yüzden, aktif laser üçgenleme sistemi ile çalışmaya devam edilmiştir.

Aktif laser üçgenleme sistemi; renkli kamera, laser kaynağı, silindirik mercek, laser huzmesinin yönelme hareketini sağlayan mekanizma ve mekanizmayı hareket ettirecek olan adım motorundan oluşmaktadır. Üçgenleme yöntemini aktif olarak kullanacak olan laser tarama sistemi, laser kaynağından gelen kırmızı renkli ışını silindirik mercekten geçirerek yüzeye çizgi halinde yansıtmaktadır. Bu şekilde, yüzeyin şeklini alan laser ışınının düzleminden gelen yansıma görüntülenmekte, hazırlanan yazılımla birlikte kırmızı pikseller algılanmaktadır. Bu sistem kullanılarak yüzey geometrisinin algılanmasında düşük hesaplama yükü ve enerji ile yüksek seviyede doğruluk oranı sağlanabilmektedir. Bu sistem için yüzey ve kamera arasındaki açı, laser ve yüzey arasındaki açı, laser ve kameranın yüzeyden yükseklikleri ve aracın duruş açıları bilinmesi gereken parametrelerdir.

Prototip üzerinde kullanılacak adım motoru, kamera sabitken laser ve silindirik mercekli mekanizmayı belirli bir açı ile döndürmesi öngörülmektedir. Bu şekilde, kameranın görüş açısındaki tüm alan tarandıktan sonra robotun kendi başına bir sonraki davranışına karar verebilmesi amaçlanmaktadır. Robot hareket halinde iken ışın düzlemini 20 santimetre önüne yansıtarak olası engelleri ve çukurları algılayabilecek, verilen hedefe doğru güvenli şekilde ilerleyebilecektir.

Tüm bu sistem ile algılanan yüzey geometrisi, robotun çevresinin 3 boyutlu olarak algılanıp haritalanmasında kullanılmaktadır. Robot hareket ederken engelleri ve çukurları algılayıp, gerekli gördüğünde durup yörüngesini yenileyecektir. Yörünge belirleme açısından "hırslı" (greedy search) planlama ve A* araştırma algoritmaları şeklinde iki farklı yapay zeka planlama algoritması denenmiş ve karşılaştırması yapılmıştır. Sonuç olarak, A* algoritması en uygun (optimal) sonucu verdiği için gezici ay mikro robotunda kullanılmaya uygun olarak seçilmiştir.

Bu çalışmada tasarlanan araç hareketli bir platform olmalı ve bulunduğu zeminde ilerleyerek yüzeyden örnek alabilmesini sağlayacak bir manipülatörü barındırmalıdır. Yapılan çalışmanın sonucunda dört tekerlekli bir gezici araç, bu araca tümleşik dört hareketlilik dereceli robotik bir manipülatör kol/uç organ tasarımı öngörülmektedir. Söz konusu aracın güvenli seyir edebilmesi için gerekli görülen çevre algılama, özellikle görüntüleme teknolojisinin gereklilikleri belirlenmiş olup üzerinde çalışma yapılmıştır. Bu çalışmalar sonucunda, yüzeydeki gölgelerden yararlanarak tanımlama yapan bir sistem ile bu sistemin eksiklikleri doğrultusunda geliştirilen aktif laser üçgenleme sistemi tanımlanmıştır. Bu sistemle birlikte kullanılmak üzere, çevre tanıma ve haritalama yapan bir yazılım geliştirilmiş ve yörünge belirleme algoritmaları ile test edilmiştir.

Sonuç olarak, keşif ve araştırma görevlerinde kullanılan gezici mikro uzay robotları daha büyük araçlara göre daha güvenli ve düşük maliyetli olma ve ayrıca tekrar üretilebilme nitelikleri ile ön plana çıkmaktadır. Bilimsel araştırmalar için de kullanılması planlanan bu araçlar farklı görevler doğrultusunda geliştirilerek, geçmişte kullanılmış daha büyük robotlardan daha hızlı bir şekilde göreve hazır hale getirilebilmektedir. Bu çalışmanın sonucunda; dört tekerlekli, hareket kabiliyeti yüksek, Ay yüzeyindeki kraterlerin etrafındaki dışa atım bölgelerinden yüzey örneği alabilecek bir araç tasarlamıştır. Araca yüklenmesi planlanan teknolojiler için gereklilikler ve hedefler belirlenmiş, üzerinde çalışılmış ve ilk örneğinin (prototip) ileriki aylarda üretilmesi ile birlikte araca yüklenmesi hedeflenmektedir.

1. INTRODUCTION

1.1 The Definition of a Robot

The actual word of robot was invented in a Czech science fiction play “Rossum’s Universal Robots” by Karel Čapek in 1921, and it was derived from the Czech word robota or robotnik meaning slave, servant, or forced labor [1]. Currently, the term robot means different things for different applications; therefore, there are many accepted definitions for it.

From space robotics perspective, it can be said that a robot is a goal-oriented machine that can sense its environment, get information about it and use that information to plan its actions and act towards a desired goal. These actions can be moving its manipulator arm, moving from an initial position to a goal position, interacting with its environment, or waiting for a new task. In order to plan and perform these actions/tasks, a robot must have a certain amount of intelligence that interprets the input sensor data and the mission statement and then creates the required commands to the hardware. It is shown in Figure 1.1 below.

Even though many robot designs are inspired by nature, the robots do not have to look and act like humans or animals but they do need to be adaptable in order to perform different tasks. There are some dangerous tasks to be performed by humans, and the robots can replace the humans in the assistance of performing those repetitive and dangerous tasks, which the humans prefer not to do, or are unable to due to the environmental conditions, size limitations, or even their physical power.

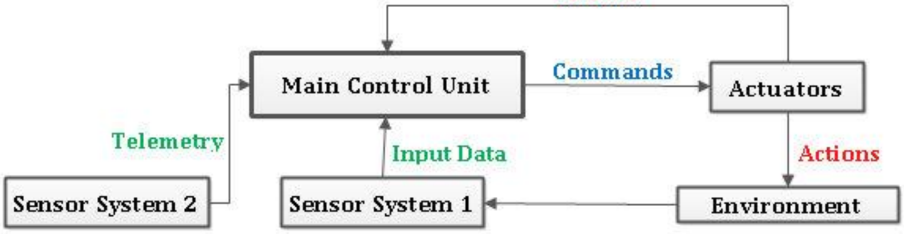

Figure 1.1 : A general representation of a robotic system.

The major components of a robotic system:

- A main body structure
- Actuators to move the mechanical parts and particular tools
- A sensory system that receives information about the external world
- A sensory system that observes the robot’s functions and condition
- A data processing and decision generating system, which includes the hardware and the software, that processes sensory information, plans the actions and controls the actuators
- A power source to activate the actuators and supplies power to sensors and the command and data handling system

A robotic system is composed of these major components to provide the stability, mobility and dexterity. It is certain that robotics is an important technology, and they will appear in the houses, streets and workplaces. By considering outer space conditions, they are an important asset of the current space missions as well as the future missions. Space robots present critical challenges as field and service robots do since these robots must operate in a changing, complex and severe environments (e.g. on Mars, Moon or orbit) despite not having an accurate map in advance of their operations. These topics are explained further in the next chapters.

1.2 Space Robotics

Space robotics is the development of robots which are capable of surviving in the space environment, at least for a time period, to perform exploration, assembly, inspection, maintenance, servicing, construction, scientific data collection or other critical tasks. To perform a task while being controlled by an operator, a space robot will be experiencing either non-negligible speed-of-light delays as in the Mars exploration or essentially zero speed-of light delay as in the Space Shuttle’s robotic manipulator arm [2]. For the case of Mars exploration, non-negligible speed-of-light delays point out the importance of the autonomous capabilities of a space robot since it cannot influence the environmental conditions. If the robot’s environment is not changing, it can make decisions more accurately; however, the information about the environment obtained from the sensory data must be understood and used efficiently in order to perform the tasks and survive while performing them.

Another challenge for these types of robots is that they must operate safely in the presence of astronauts. Manufacturing robots on Earth are high-speed robots, and the safety of humans is achieved by excluding them from the work places on Earth; however, the case differs for the future space missions. They will operate amongst the people, help to build and assembly a structure, or carry the astronauts to a mission area. Therefore, developing and improving required technologies are essential, and they have long been of interest to space robotics researchers. Examples are given in Figure 1.2 and Figure 1.3.

Figure 1.2 : A Mars exploration rover (Image courtesy NASA).

The important issues for a space robot can be expressed as:

- Surviving and operating under extreme environmental conditions
- Using arms and tools to perform tasks
- Interacting with its environment and the worksite elements accurately and safely
- Having navigational autonomy
- Allowing a time delayed control
- Moving safely to a desired position without collisions and hazards

Space robots are generally designed to do multiple tasks such as assembly, sample retrieval, inspection, planetary exploration, scientific measurements, and so on. The risky missions for humans can be accomplished by using these robots, and they can perform these complex tasks less expensively. On the other hand, a critical malfunction of the robot can terminate the main mission completely while there is no way to repair the robot. In addition, space robots wait in sleep mode until their missions begin to preserve their battery. Another important factor of these missions is that the robot is left in the operational area in the end of the mission.

There are four main concerns for space robotics [2]:

- Mobility
- Manipulation
- Extreme environmental conditions
- Time delay

Robots can perform many risky missions that humans are not allowed to do without being tired, and the robotic missions are less expensive than manned missions are. For these reasons, space robots became more attractive for many missions.

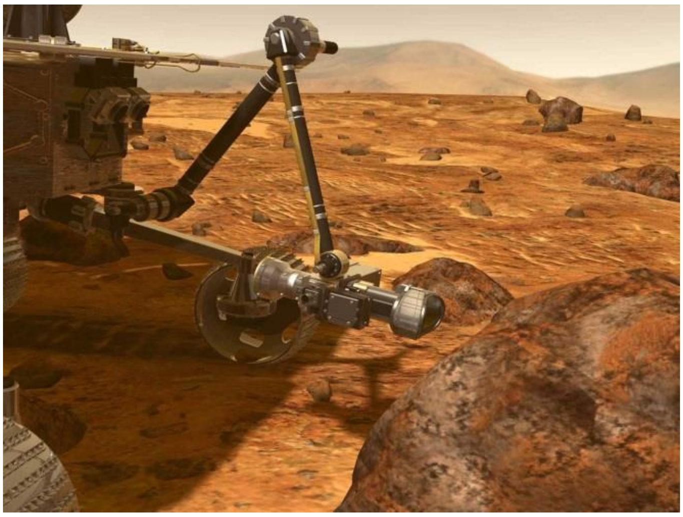

Figure 1.3 : A robotic manipulator arm on Mars exploration rover.

1.3 History of Rovers

There have been an increasing number of space mission programs involving planetary rovers. It has been proven that these robots have enlarged the operational areas for the planetary exploration successfully while achieving several missions such as the investigation of the origin of life, water and the solar system or in-situ resource utilization for the future.

The first lunar rover Lunokhod 1 landed on Moon in November 1970 by Soviet Union, which was controlled remotely in Figure 1.4. The rover was driven by solar energy captured by photovoltaic panels during the daytime, and it was equipped with a cone-shaped antenna, a directional helical antenna, four television cameras, an X-ray spectrometer, an X-ray telescope, cosmic ray detectors and a laser device. It must be noted that Lunokhod was operational more than 10 months even though it was expected to operate for 3 months, and it traveled a total distance exceeding 10 km. In addition, it sent more than 20,000 images and 206 high-resolution panoramas.

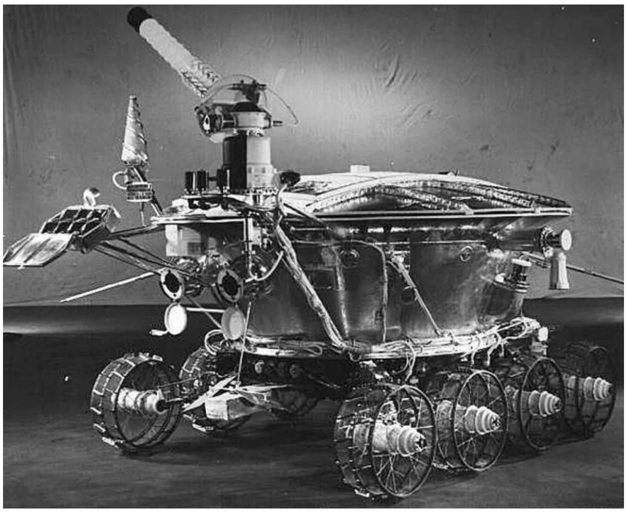

Figure 1.4 : Lunokhod 1 (Image courtesy NASA).

Moreover, Lunokhod 2 was the second remotely controlled rover that landed on the lunar surface. Since it was very similar to Lunokhod 1, it was also driven with eight wheels that contain independent suspension, electric motor and brake. The rover had a wide variety of scientific instruments such as a soil mechanics tester, solar X-ray experiment, and astrophotometer to measure visible and UV light levels, a magnetometer, a radiometer, a photo detector and a French-supplied laser corner reflector. In addition, the rover contained four panoramic cameras mounted on the top, and the energy was supplied by solar panels. Lunokhod 2 holds the record for the distance traveled on a planetary body that is 37 km on the lunar surface.

The Sojourner rover was the first planetary rover to successfully land on another planet. It was a six-wheel vehicle, which sent more than 500 images to the Earth, and it analyzed chemical properties of different locations on the planetary surface of Mars in Figure 1.5. Its weight was 10.6 kg, and its dimensions were 65 cm x 48 cm x 30 cm. It traveled about 500 meters from its lander. In addition, it had a maximum speed around 1.0 cm/s.

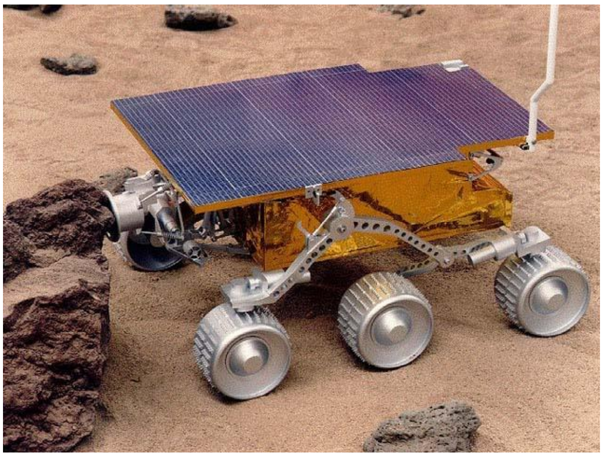

Figure 1.5 : NASA - JPL Sojourner Rover (Courtesy of NASA/JPL-Caltech).

Both Spirit and Opportunity rovers also investigated the Martian surface and geology, and on January 2004, they landed on Mars. They can be seen in Figure 1.6 and Figure 1.7. The rovers had six-wheel suspension and the dimensions of 1.5 m x 2.3 m x 1.6m. Their weight was 180 kg. During their missions, Opportunity found clues of the water flow presence in the past on the Martian surface.

Figure 1.6 : Mars rovers Spirit and Opportunity (Courtesy of NASA/JPL)

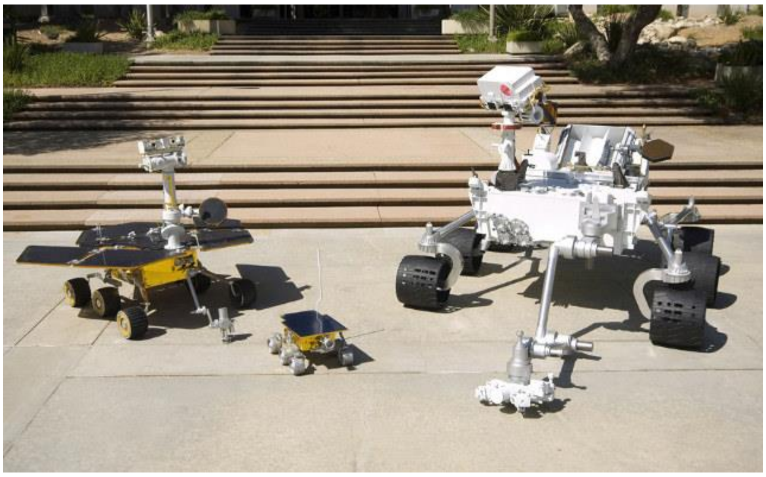

Figure 1.7 : Curiosity and previous rovers (Image courtesy NASA).

Curiosity rover is a part of NASA’s Mars Science Laboratory mission. It has scientific objectives such as investigation of the Martian climate and geology, the planetary habitability studies in preparation for manned missions, the investigation of the water flow in the past and the conditions for the microbial life. Both Sojourner and Spirit/Opportunity were powered by solar cells; however, Curiosity is using a radioisotope thermoelectric generator as a power source. The design of Curiosity will be used as the basis for the planned Mars 2020 rover mission. In addition, Curiosity completed a Martian year (687 Earth days) after finding that Mars once had environmental conditions favorable for the microbial life according to NASA’s news. Curiosity is 2.9 m long, 2.7 m wide and 2.2 m in height, which shows that it is larger than the previous Mars Exploration Rovers.

Corresponding to the results of the planetary rover missions, the space agencies and universities all over the world are researching and developing robotic vehicles for planetary exploration mission.

1.4 Lunar Micro-Rover

A lunar micro-rover is a small competent spacecraft that is capable of autonomous operation, local navigation, manipulation and control on the Moon. Therefore, it is desired to have some properties such as:

- high mobility
- low energy consumption
- simplicity to be embedded in a small body
- light weight
- low volume
- low cost

According to NASA, there is a need to have an economical solution to use a robotic spacecraft, which can be easily assembled, repaired, and customized for the interstellar missions. Further development of an LMR requires technology developments of miniaturized instruments such as which are used on CubeSats. Different kinds of mission programs involving lunar and planetary exploration are increasing in number because of scientific and commercial interests. After orbital exploration is performed, robotic vehicles can be used for surface exploration to investigate a wider area. Then, it is expected to deliver samples to Earth for further investigation.

An lunar micro-rover (LMR) is a design of a light and small rover that is used for lunar exploration, micro-payload support, remote operation and scientific measurement. Recently, mobile robotic systems such as micro-rovers are gaining attention based on the scientific importance of the Moon. In addition, finding the fundamental resources for the future missions such as manned mission or a sample return from the lunar surface to Earth requires exploring interesting geological areas such as craters by the lunar rovers [3]. A group of micro-rovers can accomplish missions that are more complex by gathering more data while operating and sharing their data [4].

All planetary rovers must move safely and accurately from an initial pose to a goal point without collisions and hazards. In addition, space robots often contain robotic manipulator arms, handling mechanisms and different tip tools to interact with their surroundings. Therefore, the required forces and torques are calculated in the simulations during the design process.

A lunar micro-rover needs to operate despite hard vacuum, lunar dust contamination, a wide range of temperature variations, significant radiation exposure, and so on. Operating in the lunar environment poses additional challenges to the LMRs. First, the robots must be able to discriminate and avoid obstacles that can cause them to tip-over or be stuck. In addition, the robots have to achieve sensor processing and planning with limited processing power and thus these actions must be as efficient as possible. For these reasons, a robotic system must be developed based on a small robot that operates in an open and dangerous environment such as the lunar surface.

2. LUNAR ENVIRONMENT

2.1 Introduction

Previous Lunar missions and new scientific results have shown that operating in the lunar environment and exploring the Moon still have major challenges for manned and robotic missions. Regarding lunar surface and its environment, the effects of them are still unknowns scientifically; however, scientific data are available from the recent missions to have an idea for preparing for future exploration.

The future exploration activities require addressing some of the environmental issues. Lunar plasma, dust, radiation, regolith, charge, temperature differences and their effects must be investigated, researched and considered carefully. The view of full Moon is given in Figure 2.1.

Figure 2.1 : The view of full Moon**.**

In the decades following the Apollo and Luna exploration era of the 1960s and 1970s the Moon fell somewhat out of the international spotlight but a multitude of recent missions from the USA, Europe, Japan, China and India have reignited interest in our nearest celestial neighbor.

2.2 Mission Proposal

According to the future missions, the geology of the Moon, potential resources and the distribution of them are gaining attention internationally since the Moon itself is an important planetary body for exploration by both human and robotic missions. For this reason, lunar micro-rovers must be designed to make scientific research that can support these missions by investigating the lunar environment and mission parameters.

As Carpenter states on his report, the scientific results obtained through the Apollo program are great enough in magnitude to eclipse those of every other planetary mission to date and are a cornerstone for our understanding of the Moon [5, 6]. Recent missions, however, have shown that our understanding of the Moon is far from complete; the Moon is far more complex than imagined and further investigations must be held.

For instance, researches previously believed that lunar volcanic activity ended a billion years ago; however, new data from NASA's Lunar Reconnaissance Orbiter (LRO) suggests that lunar lava flowed perhaps less than 100 million years ago. It is seen in Figure 2.2. John Keller, LRO project scientist at NASA's Goddard Space Flight Center in Greenbelt, Maryland, stated that this finding is actually going to make geologists edit the textbooks about the Moon.

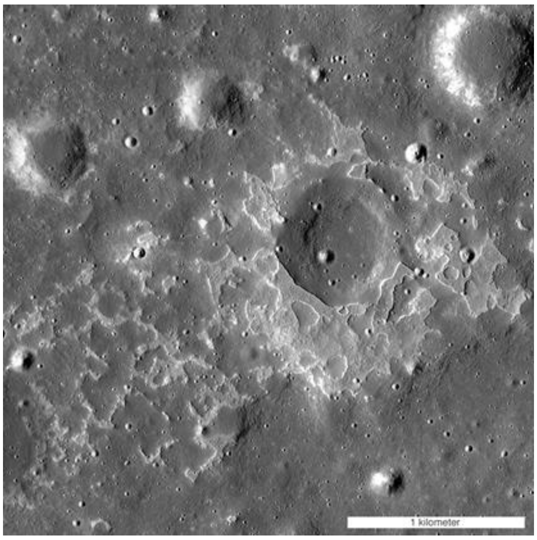

Figure 2.2 : Young volcanic rock deposits (Image courtesy of NASA/GSFC/Arizona State University).

Multiple scientific areas such as planetary sciences and geology, plasma physics, astrobiology, astronomy, space science will be benefiting from the scientific outcomes of the future lunar missions. Therefore, performing scientific researches with an LMR and addressing multiple scientific goals are important objectives.

Figure 2.3 : Lunar rock sample example.

The mission is desired to land within a determined area in South Polar region of the Moon since longer periods of solar illumination is available by reason of the low sun inclination is coupled with topographic highs [7]. For this reason, one lunar day will be longer while enabling using solar power and batteries. A significant characteristic of this region can be shown as shorter periods of darkness, which is beneficial since surviving very low temperatures such as 100K poses thermal and power subsystem challenges [7]. A lunar crater example is given in Figure 2.4 below.

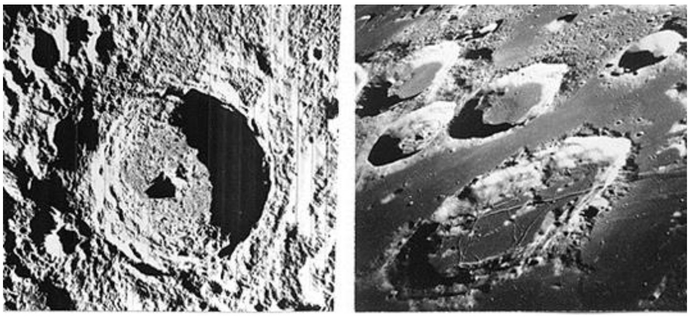

Figure 2.4 : Lunar crater example.

The main objective is to obtain a surface sample from the Moon and store it within the micro rover to study in mini laboratory, which is expected to be on the top of the LMR. The sample is desired to have a volume between 1-3 cm^3; therefore, the arm tool is designed based on a handling mechanism with a surface geometry, which enables tip tool to grab a solid rock sample from the ground; however, this tool can also be replaced with a drill mechanism for subsurface sampling. The main interest of the research is chosen as investigating the ejecta areas on the lunar surface that contains both meteor samples as well as Moon’s own material.

The uneven surface requires LMR to sense the obstacles as well as other hazards in order to get closer to the crater region, and it must be able to identify interesting sample candidates during the motion. Therefore, the primary technologies to be implemented within the LMR are chosen as local mapping, manipulation and sample handling, and path planning. The surface sampling activities will be commanded from Earth during the communication windows while the instruments within the mini laboratory analyze samples, and data of the environmental properties such as radiation, ionization, temperature will be gathered as well. The formal mission lifetime is expected to be couple of months if the LMR survives the lunar night. The first phase of the mission will contain primary scientific activities and measurements before the lunar night period; therefore, if the LMR does not survive the lunar night, it will gather and transmit data before it malfunctions.

Landing on the lunar surface can be expressed as another challenge; however, it is not one of the topics of this project. Many studies suggest orbital missions need to be coupled with surface investigations in order to validate the interpretation of data sets. In addition, surface data will show suitability for manned missions as well as validity of the models on the significant surface characteristics.

Table 2.1 : Physical properties of the Moon.

Physical Property	Parameter Value
Lunar Gravity	1.6222 m/s^2 (~g_{Earth}/6)
Lunar Vacuum	~1x 10^{-12} mm Hg
Lunar Atmosphere	10^4molecules/cm^3 day and $2\ x\ 10^5$molecules/$cm^3 night$
Surface Temperature	$121^oC\ and\ -240^oC$
Sidereal Rotation Time	27.322 days
Inclination of Equator/Orbit	$6^o41'$

2.3 Lunar Dust and Plasma Environment

Moon does not have an intrinsic atmosphere or a global magnetic field; however, it is seen that the dust particles are flowing around near the ground level due to the gravitational and the magnetic affections during the investigations of the exterior lunar surface [8]. The surface is directly facing the solar wind particles providing potential to investigate the solar interactions from the surface. A lunar rover could collect the environmental data needed by its on-board magnetometers and plasma instruments, and the restored data would be useful for the determination of the lunar surface conditions. Lunar dust and plasma environment is represented in Figure 2.5.

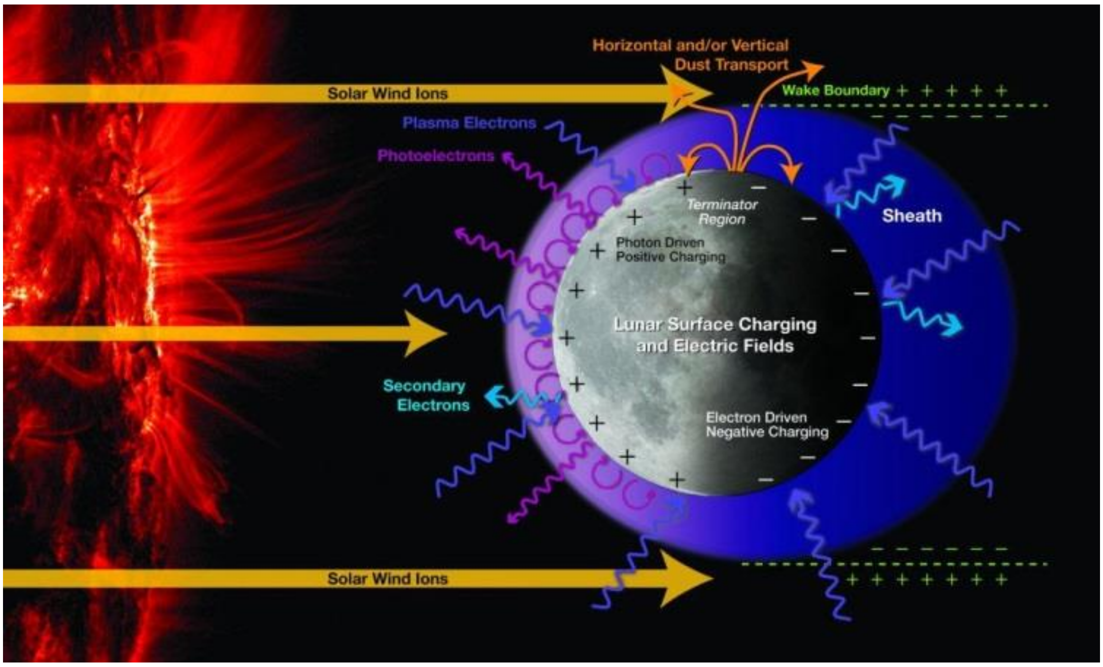
Horizontal and/or Vertical
Dust Transport
Solar Wind Ions
Wake Boundary
Plasma Electrons
Photoelectrons
Terminator Region
Sheath
Photon Driven Positive Charging
Lunar Surface Charging and Electric Fields
Secondary Electrons
Electron Driven Negative Charging
Solar Wind Ions

Figure 2.5 : Lunar dust and plasma environment (Image courtesy NASA).

As Saito et al. include in their article, Lunar Prospector satellite has unveiled the plasma interactions with crustal magnetic fields, surface charging and wake structure of the lunar plasma environment by its three axis measurements after the 1990s [8]. In 2000s, several missions investigated the lunar environment. Recent in-situ measurements of Kaguya (SELENE) spacecraft have revealed the dynamics of lunar plasma environment. The low energy ions measured around the Moon made by MAP-PACE (MAgnetic field and Plasma experiment – Plasma energy Angle and Composition Experiment) on Kaguya has been used for the investigations. Launch of the Kaguya was successfully held on 14 September 2007 by the H2A launch vehicle [8]. Although there are several more missions like Chang’E-1 of China, Chandrayaan-1 of India and LAIDEE of NASA that measures low energetic ions, the information gathered by the Kaguya’s data are going to be presented in order to comprehend the lunar plasma environment on a basis.

Kaguya has found four evidently distinct ion distributions on the dayside of the Moon by its 100 km altitude: (1) solar wind ions backscattered at the lunar surface, (2) solar wind ions reflected by magnetic anomalies on the lunar surface, (3) ions that are originating from the solar wind ions reflected/scattered at the lunar surface and are picked up and accelerated by the solar wind convection electric field, and (4) ions emerging from the lunar surface/lunar exosphere [8].

Although there is an expectation that the all of the ions are absorbed by the surface of the Moon, Saito et al. have discovered that about 0.1% to 1% of the incident solar wind ions were backscattered. These backscattered protons were found losing their energies and did not contain alpha particles, which were mostly consisted of the solar wind, because of the collisions at the lunar surface. Also, it has been seen that there is a gradual decrease of the backscattered ions going from the equator to the poles indicating that the more vertical collisions were creating more backscattering [8].

Secondly, Kaguya also spotted several magnetic anomalies on the surface where the protons having more energy than the backscattered and incoming solar wind particles. The scientists, who are investigating these anomalies, claim that these abnormal particle reflections could be caused by regional closed field lines created by the magnetically dense regions on the surface or by the electric field occurring from the wake side to the night side of the Moon, creating a magnetic field also [8].

Third ion population found by the sensors of Kaguya is solar wind ions backscattered or magnetically reflected, then accelerated. The solar wind creates and magnetic and electric fields alongside of the surface that could accelerate the backscattered ions coming with the right angle. Saito has called this mechanism as "self-pickup acceleration" [8].

Finally, Yokota et al. observed the alkali ions originating from the lunar surface from the same mission [9]. Solar wind conducting electric field on the surface accelerates the ions generated from the surface by solar wind sputtering, solar photon stimulated desorption, or micro-meteorite vaporization. Heavy ions including C+, O+, Na+, K+ and Ar+ have been found by the IMA (Ion Mass Analyzer) of Kaguya. Even though the particles inside of the Earth's magnetic field are not energetic as the solar wind ions, the backscattering of the heavy ions was observed. When Moon enters to the magnetosphere lobes, it was expected not to observe these heavy ions but Tanaka et al. have been confirmed there were samples found by IMA data and believed that the reason for this mechanism is either photon stimulated desorption or the potential between the lunar surface and Kaguya [9,10].

Both solar wind and magnetospheric plasmas are incident on the Moon’s surface, and since the Moon is in the magnetotail, which it means passing through the magnetosphere for around 25% of its orbit, the solar wind composes the most of the incident particles. These particle interactions are needed to be measured in order to gain further understanding the dust, radiation and plasma environment on the lunar surface by providing additional data to the present. As seen in the space environment models and spacecraft’s scientific instrument data, solar wind particles (SWP) are naturally regarded as cold plasma where magnetospheric plasma have greater energies with lower density compared to SWPs. Therefore, the measurement of the velocity, energy and distribution of these particles can be chosen as a significant mission objective for the LMR. Lunar orbit can be seen in Figure 2.6.

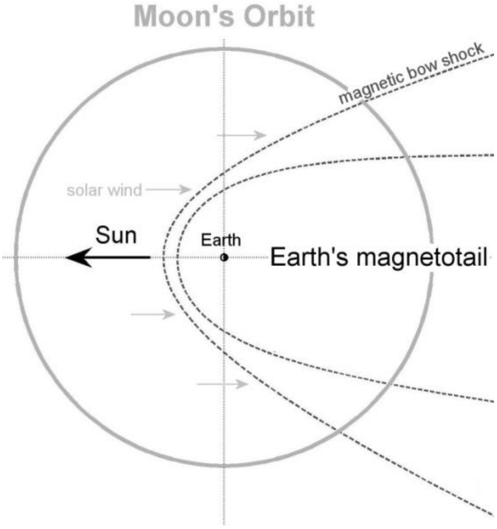

Figure 2.6 : Lunar orbit (Image courtesy NASA).

Additionally, during Apollo missions on the Moon, it was seen that the lunar dust can be a significant problem for the robotic missions as well as manned missions since it reduces visibility and covers the surfaces of the equipment and instruments. It is stated that re-analysis of data from the Dust Detector Experiments (DDEs) showed that lunar dust prevented the Apollo 11 module may have failed because of the lunar dust contamination during ascent of the Apollo 11 module [11,12].

In addition, the clothing of the astronauts was affected by lunar dust contamination, and it should be noted that breathing the dust particles is adversely affects the human health as seen in Apollo mission. Moreover, it is also found that the dust prevented decent sealing of the containers since none of them, which contains rock samples, was able to hold vacuum after returning to Earth [13]. It is shown in Figure 2.7.

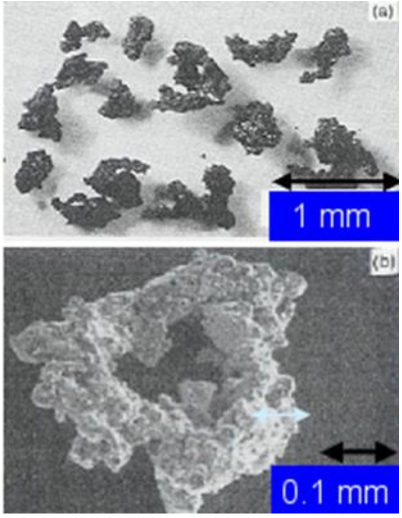

Figure 2.7 : Lunar dust.

2.4 Lunar Radiation Environment

Different kinds of radiation on the lunar surface are a significant risk for the LMR as well as humans. Four specific populations are dominating sources on the surface of the Moon such as [12]:

- low energy Solar Wind Particles (SWPs)
- high energy Galactic Cosmic Rays (GCRs)
- occasional high energy particles released during Solar Energetic Proton (SEP) events
- Secondary radiation generated by the interactions of the surface and subsurface of the Moon and the first three sources

Particle interactions with materials in the LMR would generate secondary radiation as well as the interaction with the lunar surface and subsurface. Understanding the radiation environment and the techniques of the radiation protection is necessary for the LMR mission as well as the future missions. There are recent studies for the radiation protection of interstellar CubeSat and other miniature spacecraft such as the LMRs. The radiation environment influences spacecraft electronic instruments such as single event effect, displacement damage and total ionization dose, and the chosen electronics of the LMR must also be considered according to their radiation tolerance from their data sheet. The electronic instruments which are sensitive to radiation can be placed together in order to use local radiation shield, also it must be stated that different materials are needed in order to stop different kind of particles such as protons, electrons, photons etc.

Aluminum is an acceptable option due to its density and shielding properties. Further studies indicated that since the light materials reduces the energy of the protons better, using low density materials reduces the risk of producing secondary particles; however, increasing the shield thickness would become essential. On the other hand, weakening the energy of electrons and photons by high-density materials is superior to those low density materials; however, increasing the high-density material thickness would cause many secondary particles. Therefore, multi-layered radiation protection with high density and low-density materials is optimal radiation shield due to different radiation effects [14]. Further investigation on radiation shielding for the LMR will be done in the future for this project according to the environment.

3. LUNAR MICRO-ROVER PROTOTYPE DESIGN

3.1 Introduction

The primary mission objectives determine not only the tasks performed by the LMR, but also the system requirements that define completely the micro-rover's abilities, and the research area for the lunar micro-rovers (LMR) is extensive such as navigation, obstacle avoidance, path planning, rover platform design, field-testing, motion kinematics, slip models, and so on. Since there was no rover platform to work on in our faculty, the project started with designing a micro-rover platform to implement certain technologies for testing not only during this project but during the future projects as well.

A small lightweight rover provides significant benefits in the launch and landing since the size and the weight of the vehicle is limited. For this reason, there is not enough room for complex ideas. In addition, the energy limitations require actuators to be chosen those consume less power since there is limited electrical power from the solar panels. Most of the time in an LMR, power is generated using the solar panels and stored in the batteries whereas the onboard computer performs multiple tasks and plans the actions. In the design process, the most important considerations were mobility and weight limitations. The final design can be seen in Figure 3.1.

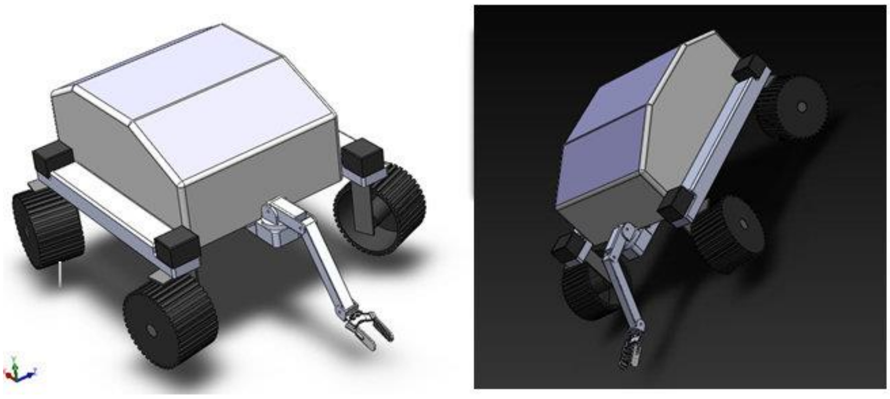

Figure 3.1 : Cad drawing of lunar micro-rover design.

An LMR design is lightweight with high mobility, energy efficient and resistant to hard vacuum, lunar dust contamination, a wide range of temperature variations, significant radiation exposure, and so on. The body structure generally has low volume; however, it must provide sufficient space for all the subsystems. Therefore, the rover platform must be simple and versatile as much as possible.

The mass and inertia properties are derived from Solidworks after material selection. The material of the suspension and the main body is predicted to be Al 2219-T87 alloy, which was successfully used for the Apollo mission, Saturn V, and Space Shuttle; therefore, it has already proved its reliability for the extreme lunar environment as well as outer space.

The rover must be able to move to goal points to make measurements with its onboard instruments and transmit the data; therefore, the development of intelligent and autonomous motion guidance is important as much as the mobility system of the prototype. In addition, the micro-rover must be able to provide images of the Moon, telemetry data for the scientific uses and high-resolution panoramic imagery of the lunar terrain while the micro-rover safeguards itself during operations against the local hazards and survives radiation environment during transfer to the Moon as on the lunar surface.

The lunar surface temperature varies from -240^{o}C at night to 121^{o}C during the day, and the onboard computer and batteries can keep the electronics warm in order to operate in that low temperature. The next step for this project is to build prototype for verification of the performance and to have a micro-rover platform to work on in our faculty.

3.2 Design Progress

Previously, it is said that the primary mission objectives determine not only the type of tasks performed by the LMR, but also the system requirements that define exactly the rover’s abilities. These properties were then utilized to determine the subsystem requirements for the LMR system.

At the beginning, the design of the lunar micro-rover was a 6-wheel system with a rocker-bogie suspension that has a mechanism as passive rotary joint to attached two links called rocker and bogie as in Figure 3.2. As wheels are free to move up and down on uneven terrain with the rotary joint, each wheel carry the weight of the LMR equally, but it is much heavier than a 4-wheel suspension, and each extra actuator causes more energy consumption and higher hardware requirements.

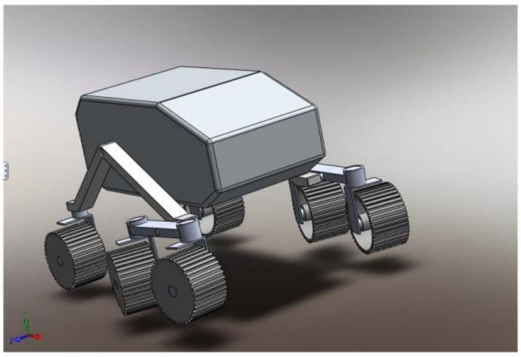

Figure 3.2 : Cad drawing of lunar micro-rover design 01.

Overall architecture of the LMR contains mechanical hardware, electronics, computing hardware, sensors, actuators, real-time onboard software, mission operations software and mission tools.

After considering easier and quicker production value and the simplicity, the design was adjusted to have a different suspension. The following design is used to compare the suspension system of the rover, which is shown in Figure 3.2 above. LMRs move most of their time on roughly even surfaces where wheeled mechanisms have maximum performance, and the micro-rovers avoid obstacles and highly uneven surfaces most of the time. Further considerations and trade-off work lead the design to have a 4-wheel suspension since the suspension system is the key design issue for the mobility, which is detailed in the mobility section. The chosen final design is shown in Figure 3.4.

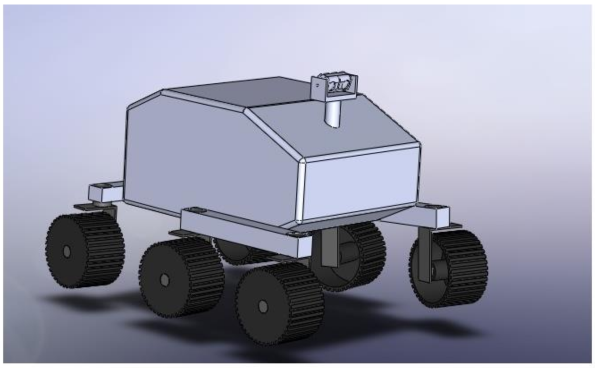

Figure 3.3 : Cad drawing of lunar micro-rover design 02.

Considering that, LMRs travel most of their time on roughly even surfaces where wheeled mechanisms have maximum performance, a wheeled drive system has some advantages as having better speed on even terrain, being simple and a mature technology, having adequate mobility, providing high ratio of payload to micro-rover's weight, consuming relatively low power and therefore being energy efficient. On the other hand, the disadvantages can be shown as having relatively low slope climbing capacity due to wheel slippage and obstacle traverse capability that is relatively less compared to other concepts.

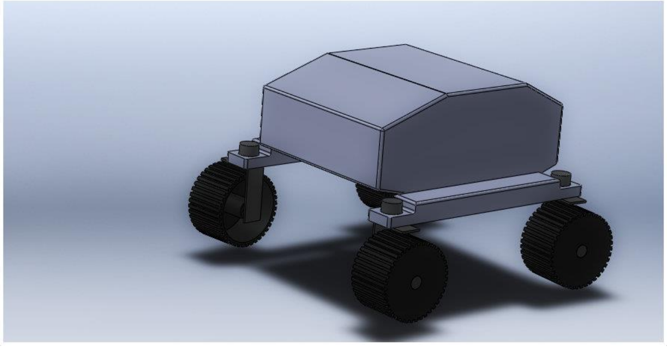

Figure 3.4 : Cad drawing of lunar micro-rover design 03.

The final design of the LMR is desired to use CubeSat architecture since interplanetary CubeSat missions are gaining attention increasingly in the recent years, and miniaturized instruments are being developed as their radiation resistance increases. A CubeSat platform is a type of a miniaturized satellite for space missions, and it can support scientific research while being inexpensive and using mostly commercial off-the-shelf components for its electronics. The final design of the LMR is determined to contain at least 4U CubeSat while benefiting from the knowledge of interplanetary CubeSat designs and missions especially for radiation protection and temperature variations. A CubeSat example is given in Figure 3.5.

Figure 3.5 : 1U CubeSat example.

The CubeSat standard has been extensively used to implement science missions with low cost with many purposes. Many factors such as low complexity, low mass and volume motivate the development, and the micro-rover will benefit the properties such as reusability of the components, extendibility of the platform with no changes, short development timelines, available hardware. In addition, the similarities between a micro-rover and CubeSat are limitations of payload sizes, short life expectancy, being ideal platforms for technology demonstrations.

Mission and system requirements can be listed as:

- Mission Target: Moon
- Dimensions (mm): 365 x 575 x 575
- Maximum weight: 10 kg
- Maximum speed: 5 cm/sec
- Payload: Robotic Manipulator Arm, Mini Lab, several scientific instruments for environment
- Surface properties: flat, rocky, crater, regolith, steep slopes
- Power source: Solar panels and battery
- Sample collection: handling from the ground, subsurface (if drill mechanism is added)
- Locomotion: 4 wheel suspension (independently steered and driven wheels)
- Mapping: Active Laser Triangulation System
- Hazard Detection: Active Laser Triangulation System

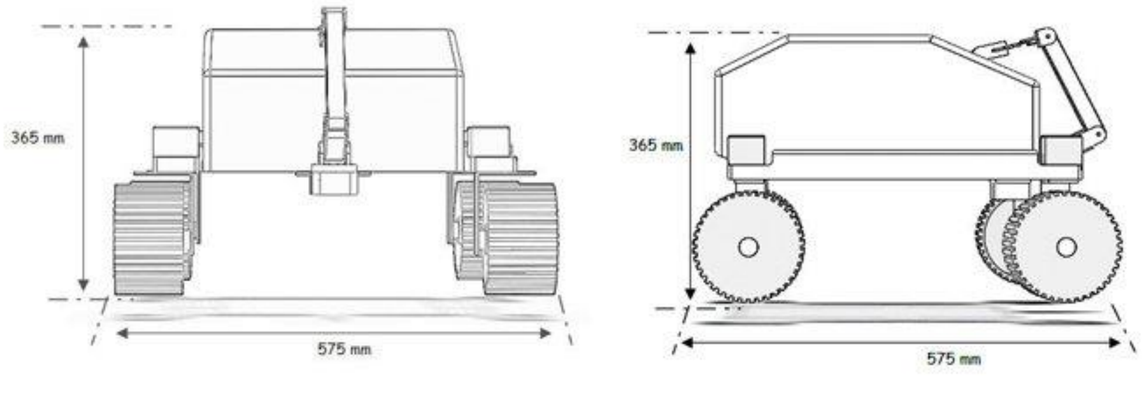

Figure 3.6 : The final dimensions of lunar micro-rover.

A design concept is chosen after considering different design configurations. The locomotion subsystem consists of a four-wheel suspension with all four wheels independently steered and driven to increase terrainability. The thermal system is expected to be mostly passive, and the heat produced by the onboard computer and batteries is utilized. Another additional choice can be heat-generating devices placed to control the temperatures of the critical hardware components.

3.3 Mobility System

There are some choices for mobility system for a wheeled lunar micro-rover such as:

- 3 wheeled drive system
- 4 wheeled drive system
- Multi wheel drive system (6 and more wheeled suspension)
- Rocker-bogie suspension
- A mechanism and rocker bogie suspension

For a micro rover, a 4-wheel suspension mechanism has some features as simplicity, easier to build, lightweight, having less actuator but no mechanism to improve the mobility of LMR. It is shown in Figure 3.7.

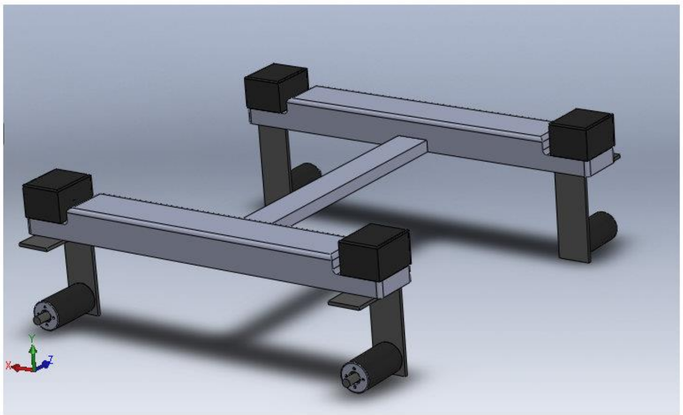

Figure 3.7 : The suspension mechanism of the LMR without the wheels.

While determining the wheel properties, the wheels with smaller diameter have less surface area in contact with the lunar surface, and it causes less friction when the micro-rover moves and steers on the terrain. Therefore, lunar micro-rover will be able to navigate rough terrain better. The wheels in Figure 3.8 are expected to have a diameter of 7.5 cm, and stripped design would help in moving on the lunar regolith.

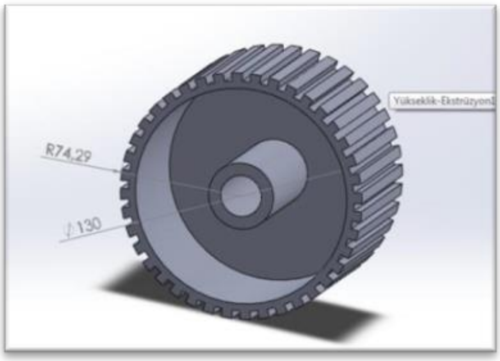

Figure 3.8 : Cad drawing of the wheels.

The suspension mechanism allows the LMR to have different drive modes such as turning in one place, crab movement, passive or active wheel. According to the final design, the velocity is determined to be between 3-5 cm/sec, and each wheel is steered and driven independently. The maximum obstacle clearance in front of the LMR is expected to be around 20 cm, and the rover is free of obstacles with less height of around 16.4 cm, which means it can pass those obstacles without hitting the bottom.

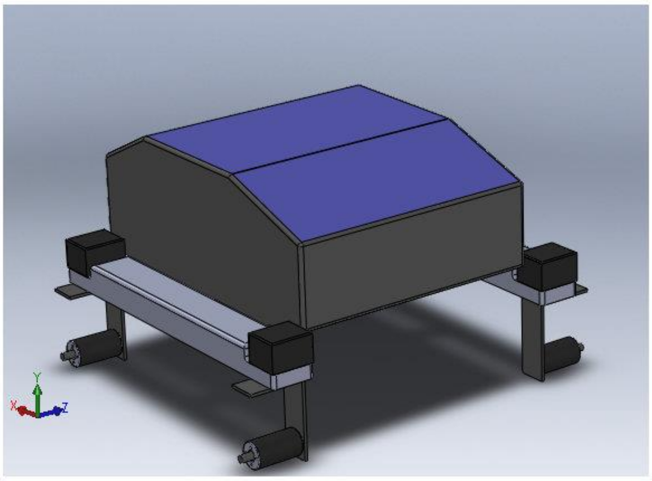

Figure 3.9 : Cad drawing of the LMR without the wheels.

According to the final design, the LMR requires eight step motors for driving and steering its wheels independently. Multiple mobility modes such as turn-in a single place, crab motion are useful during the path planning since it uses the kinematic limitations of the LMR.

As seen in the design process, the micro-rover prototype design was using the rocker-bogie suspension system; however, it is not a suitable system for our LMR even though it provides higher degree of mobility and ability to smoothly climb rocks 1.5 times its wheel diameter vertically [1]. The rocker-bogie suspension needs six wheels and ten actuators which is the meaning of increasing weight. Moreover, another problem occurs when using attached links such as strong stresses would be applied on the links and the joints even if a small force were acted on the wheels contacting the lunar surface or an obstacle. Therefore, it would require being produced thicker, consequently heavier to endure that stress [1]. For these reasons, the final prototype design contains four wheels, which the load of the weight is distributed equally to them, and the wheels are broadened in the design according to sinkage considerations.

Overall mechanical and structural properties can be given as:

- 10 kg-class
- 365 mm height, 575 mm width, 575 mm length
- 75 mm wheel diameter
- 420 mm distance between wheel centers
- 4-wheel suspension, independently driven and steered wheels
- 50 mm/sec maximum speed
- 200 mm maximum obstacle clearance
- 164 mm ground clearance
- Multiple mobility modes (turn-in place, “crab”, passive active wheel)
- 5 D.O.F. fully actuated and instrumented front science arm
- 4U CubeSat can be accommodated inside the main body

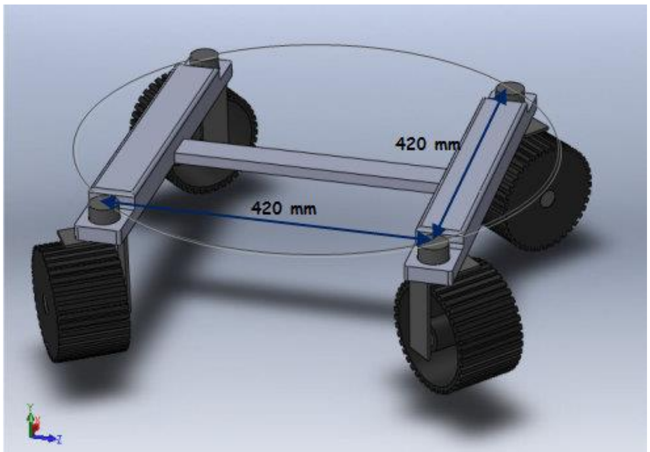

Figure 3.10 : The distance between the rotational axis of the wheels.

The actuator and wheel selection is made by considering the project cost and ability to acquire commercial off-the-shelf components in Istanbul, Turkey. Therefore, the most suitable choice was NEMA 14-size hybrid bipolar stepping motor, which has a 1.8° step angle. According to actuator specifications, each phase draws 280 mA at 7.4 V, allowing for a holding torque of 650 g-cm. The motor has four color-coded wires terminated with bare leads: black and green connect to one coil; red and blue connect to the other. It can be controlled by a pair of suitable H-bridges (one for each coil), but it is recommend using a bipolar stepper motor driver. 5 mm universal mounting hub can be used to mount objects on the stepper motor’s 5 mm-diameter output shaft for attaching to the wheels and the rotational links on the suspension.

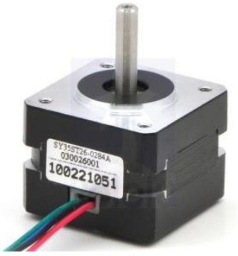

Figure 3.11 : Hybrid bipolar stepping motor.

Actuator Specifications:

- Size: 35 mm square × 26 mm, not including the shaft
- Weight: 130 g
- Shaft diameter: 5 mm “D”
- Steps per revolution: 200
- Current rating: 280 mA per coil
- Voltage rating: 7.4 V
- Resistance: 26 Ω per coil
- Holding torque: 650 g-cm
- Inductance: 19.2 mH per coil
- Lead length: 30 cm

Figure 3.12 below shows the stepper motor dimensions in mm. The dimension labeled “length” is 26 mm. The output D-shaft has a length of 21 mm and a 5 mm diameter with a section that is flattened by 0.5 mm. This shaft works with our 5 mm universal mounting hub.

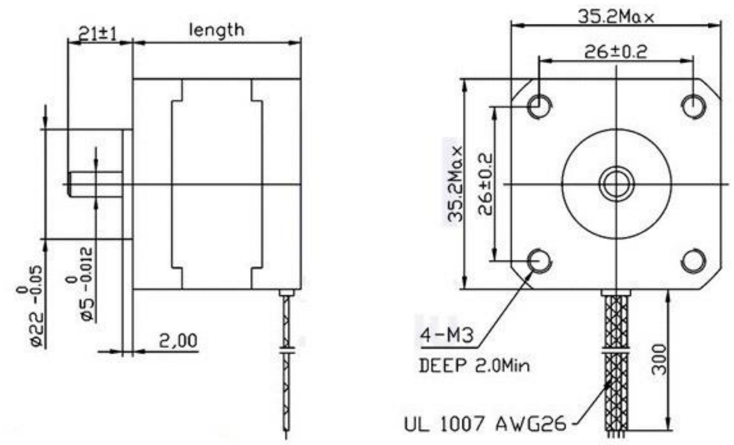

Figure 3.12 : Stepping motor dimensions in mm.

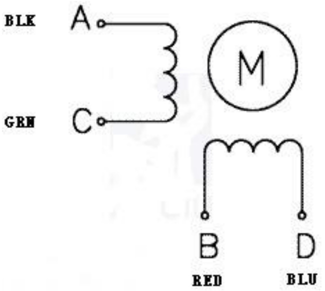

Figure 3.13 : Stepping motor diagram.

EasyDriver Stepper Motor Driver in Figure 3.14 is the hardware choice for the actuator control as shown in Figure 3.13 above. It is stated that the EasyDriver is a simple to use stepper motor driver, compatible with anything that can output a digital 0 to 5V pulse or 0 to 3.3V pulse if it is soldered SJ2 closed on the EasyDriver. It requires a 7V to 20V supply to power the step motor and can power any voltage of stepper motor. It provides much more flexibility and control over the stepper motor, when compared to older versions. The micro step select pins of the A3967 are broken out allowing adjustments to the micro stepping resolution. The sleep and enable pins are broken out for further control. The EasyDriver has an onboard voltage regulator for the digital interface that can be set to 5V or 3.3V. Precision motor control is obtained by connecting a 4-wire stepper motor and a microcontroller.

EasyDriver Stepper Motor Driver Features:

- A3967 micro stepping driver
- MS1 and MS2 pins broken out to change micro stepping resolution to full, half, quarter and eighth steps (defaults to eighth)

- Compatible with 4, 6, and 8 wire stepper motors of any voltage
- Adjustable current control from 150mA/phase to 750mA/phase
- Power supply range from 7V to 20V

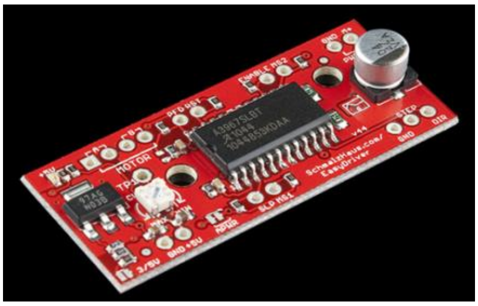

Figure 3.14 : Stepper motor driver.

There is not a variety of wheel models to select for the prototype. The closest choice to be found in dimensions is 125 mm x 58 mm strong terrain wheel as seen in the Figure 3.15.

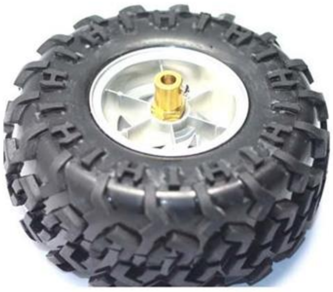

Figure 3.15 : Terrain wheel for the LMR prototype.

Battery selection is also made considering the project cost and ability to acquire commercial off-the-shelf components in Istanbul, Turkey. Therefore, the most suitable choice was LiPo 2S 7.4V 4100mAh 25C as shown in Figure 3.16 below. It is suitable for the projects such as quadrocopter, model planes, robots etc., and it requires a proper battery charger. It is chosen according to the actuators, which consumes most of the electrical power from the LMR prototype.

Figure 3.16 : The battery of the LMR.

LiPo Battery Specifications:

- Dimensions: 138 x 46 x 24 mm
- Weight: 255g
- Charge Rate: 1C (4.1A)
- Continuous Discharge: 25C (102.5A)
- Max Burst Rate: 40C (164A)
- Max Volts Per Cell: 4.2V
- Max Pack Voltage: 8.4V
- Min. Discharge Volts: 6.0V
- Watt Hours: 30.34

3.4 Conclusion

The objective of this study is to design a four-wheeled micro-rover with high mobility, which can investigate the ejecta areas on lunar surface that contains both meteor samples as well as Moon’s own materials. Building the LMR prototype will start on a breadboard with using the components, which are listed above after the presentation of the thesis. As it is stated, a micro-rover has some advantages over bigger rovers since they are more robust, more adaptable to different tasks with minor modifications, faster and cheaper to be reproduced after the completion of the original design and easier to launch and land on the lunar surface. A 4-wheel suspension is preferred in order to have a light weighted, simple and less power consuming suspension instead of the rocker-bogie mechanism. Some technologies, which will be integrated in the rover explained in the next sections, are determined and presented.

4. ROBOTIC MANIPULATOR ARM

4.1 Structural and Mechanical Design

To design a robotic manipulator arm that can be mounted on a mobile micro-rover, robotic arms must be lightweight with high mobility, and the position of the robotic arm must be considered carefully. Since the robotic arm would be used for sample gathering from the lunar surface, it is placed on the front side of the micro-rover, and it is chosen to be in the middle of the sample container of the mini-lab that is predicted to be on the top of the rover and the lunar surface. Meanwhile, the robotic arm must provide sufficient space for the actuators, cameras, sensors etc. The actuators on the arm are used for positioning of the links, and the final actuator on the tip tool is used for handling small rock samples from the lunar surface.

In design process, the most important considerations were mobility and weight limitations. The mass and inertia properties are derived from Solidworks after material selection. The materials are predicted to be Aluminum alloy, which was successfully used for the Apollo mission, Saturn V and Space Shuttle etc.; therefore, the chosen Al 2219-T87 alloy, which has a density of 2840 kg/m^3, already proved its reliability for the extreme lunar environment as well as outer space. The design is shown in Figure 4.1 and Figure 4.2.

Mechanical Design Objectives

- To have a suitable robotic manipulator arm system for a micro-rover
- To have sufficient degrees of freedom
- To maximize the operating space
- To minimize additional mass for to the LMR(Lunar micro-rover)
- To have enough space for actuators, sensors
- To minimize the risk of contact or collision of the arm’s link with each other as well as other surfaces
- To be able to reach to the lunar surface and the top of the LMR

While considering the mass and volume properties of the robotic arm, the main objective is chosen as reaching ground to have a surface sample from the Moon and store it within the micro-rover. The sample is desired to have a volume between 1-3 cm^3; therefore, the arm tool is designed based on a handling mechanism with a surface geometry that enables tip tool to grab a solid rock sample from the ground in Figure 4.3.

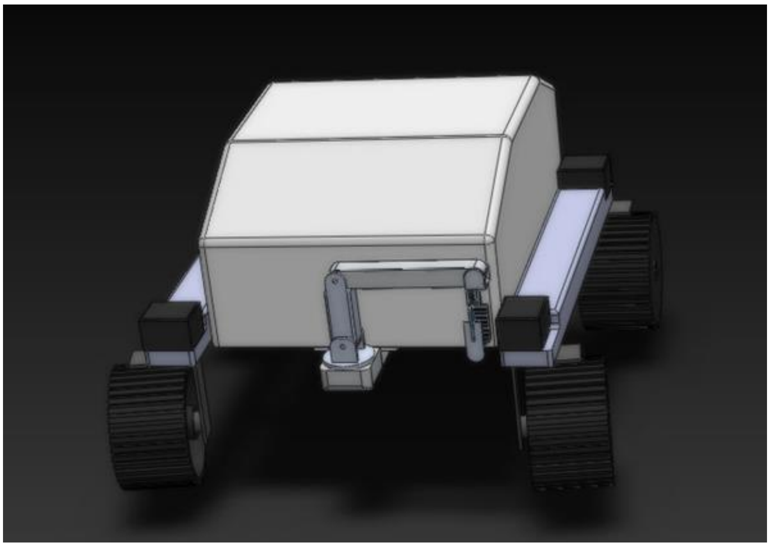

Figure 4.1 : Robotic manipulator arm closed pose.

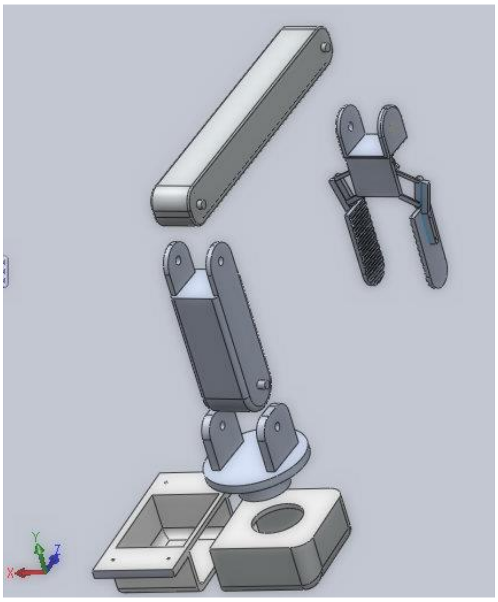

Figure 4.2 : Robotic manipulator arm assembly exploded view.

Each part of the robotic arm is designed by examining commercially available hardware, which is low cost and attainable. Even though the chosen components of the hardware, which were taken as an example, were not resistant for outer space conditions, they can be replaced with radiation-proof ones. In addition, they can be produced and ordered specially for specific mission conditions. Typically, this includes conditions of lunar gravity, hard vacuum and extreme temperature variations etc.

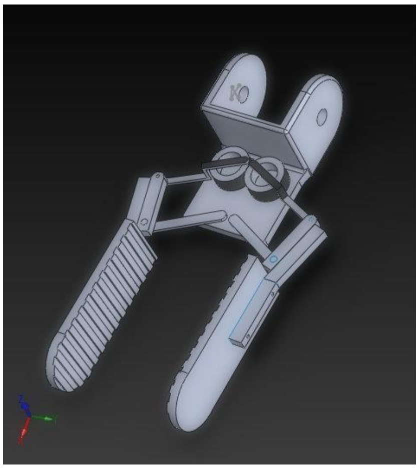

Figure 4.3 : Robotic manipulator arm tip tool design.

Table 4.1 : The predicted mass of the robotic arm structural.

Part Name	Mass(gr)
Base	92.70
Link 1	94.50
Link 2	92.49
Link 3	98.86
Tip tool	14.22
Total	**392.97**

4.2 Modeling of Robotic Manipulator Arm

Kinematics is the branch of classical mechanics that studies the motion of points, bodies and systems of bodies without consideration of its mass or the forces acting on them [20]. A robotic arm comprises a chain of mechanical links and joints that allow actuators to be mounted on its structure. Every link is connected by joints while the base of the chain is generally fixed and the other end, which holds the end effector and needed tools, is free to move in workspace. Each joint has one degree of freedom, either prismatic or rotational, which specifies the movement type. During arm motions, the relative angles or positions of its neighboring links changes, and each joint can move its outward adjoining links and move by its inward adjoining links.

For this project, Denavit-Hartenberg convention is used for kinematics solution of the designed robotic manipulator arm as well as spatial operator algebra. In addition, the trajectories are determined by using Matlab, and it is crosschecked by using Matlab Robotic Toolbox. The dynamics model is implemented with the trajectories saved in the Matlab workspace.

4.2.1 Forward Kinematics

Jacques Denavit and Richard Hartenberg introduced a convention in order to standardize the coordinate frames for linkages in 1955 [20]. A robot manipulator with n+1 links has n joints in order to connect all the links being used. For instance, a robotic system with two links must have one joint to attach them. If the joints are numbered from 1 to n, and the links are numbered from 0 to n starting from the base, the joint 1 will connect the link 0 and the link 1. Meanwhile, a reference frame must be assigned considering the base. In many systems, the base is fixed; however, it is different for planetary or orbital missions. Moreover, when joint n is actuated, the link n will be moving, and it must be considered that the location of the joint n is fixed with respect to the link n–1.

Transformation matrix calculation

The joint n connects the link n-1 to the link n, and the transformation from the link coordinate frame i-1 to frame i is defined in terms of elementary rotations and translation as:

$$H_{i-1,i}(\theta_i, b_i, \alpha_i, a_i) = T_{Rz}(\theta_i) * T_z(b_i) * T_x(a_i) * T_{Rx}(\alpha_i) \tag{4.1}$$

$$H_{i-1,i} = \begin{bmatrix} \cos(\theta_i) & -\sin(\theta_i) * \cos(\alpha_i) & \sin(\theta_i) * \sin(\alpha_i) & a_i * \cos(\theta_i) \\ \sin(\theta_i) & \cos(\theta_i) * \cos(\alpha_i) & -\cos(\theta_i) * \sin(\alpha_i) & a_i * \mathrm{s}\,in(\theta_i) \\ 0 & \sin(\alpha_i) & \cos(\alpha_i) & b_i \\ 0 & 0 & 0 & 1 \end{bmatrix} \tag{4.2}$$

Assignment of the coordinate systems

- z_n: it is along the axis of joint n + 1. For a revolute joint, the joint axis is along the axis of rotation. For a prismatic joint, the joint axis is along the axis of translation.
- x_n: It is pointing along the common perpendicular of z_{n-1} and z_n pointing towards the next joint. If z_{n-1} and z_n intersect, then x_n can be chosen to be pointing towards to the tip of the robotic arm. For x_0, it is preferred to point towards to outward of the robotic manipulator arm.
- y_n: It should be chosen according to the right hand rule for coordinate systems.
- O_n point is chosen as the location where the perpendicular axes of z_{n-1} and z_n intersect. If z_{n-1} and z_n are parallel, it is chosen as b_n being zero. At first the common perpendicular between z_{n-1} and z_n should be identified, or point of intersection. At the point of intersection, or at the point where the common perpendicular meets the nth axis, the frame origin must be assigned [21].

The Denavit–Hartenberg parameters, which are also called DH parameters, are the four parameters associated with a particular convention for attaching reference frames to the links of a spatial kinematic chain or a robot manipulator.

Assignment of the DH parameters

- a_n: the distance between the origin of the n^{th} coordinate system and the intersection point of the n^{th} link's perpendicular and z_{n-1} axis measured along x_n.
- α_n: the angle between z_{n-1} and z_n axes measured around x_n.
- b_n: the distance the origin of the $n\text{-}1^{th}$ coordinate system and the intersection point of the nth link's perpendicular and z_{n-1} axis measured along z_{n-1}.
- θ_n: the angle between x_{n-1} and x_n axes measured around z_{n-1}.

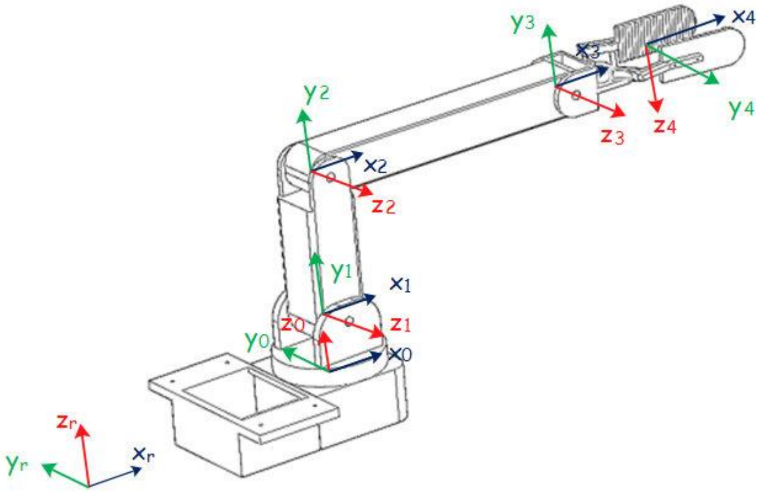

Figure 4.4 : The axis assignment of the robotic arm with handling mechanism.

Table 4.2 : The DH parameters table of the arm.

	a	**α**	**b**	**Ready-state value**
R ← 0	220 mm	0^o	164 mm	-
0 ← 1	0	90^o	30 mm	0^o
1 ← 2	80 mm	0^o	0	90^o
2 ← 3	160 mm	0^o	0	0^o
3 ← 4	91 mm	90^o	0	0^o

4.2.2 Robotic Manipulator Arm Pose Examples

- **The Ready-State Pose**

The ready state of the arm ([1.57 1.57 -1.57 -1.57](rad)) is chosen as closed position in front of the robot's structure as seen in Figure 4.5 below, and then the homogenous matrix is calculated not from the rover's base but the robotic arm base part.

$$Transformation\ Matrix: \quad H_{14} = \begin{bmatrix} 0 & 1 & 0 & 0 \\ 0 & 0 & -1 & 160 \\ -1 & 0 & 0 & 14 \\ 0 & 0 & 0 & 1 \end{bmatrix} (mm)$$

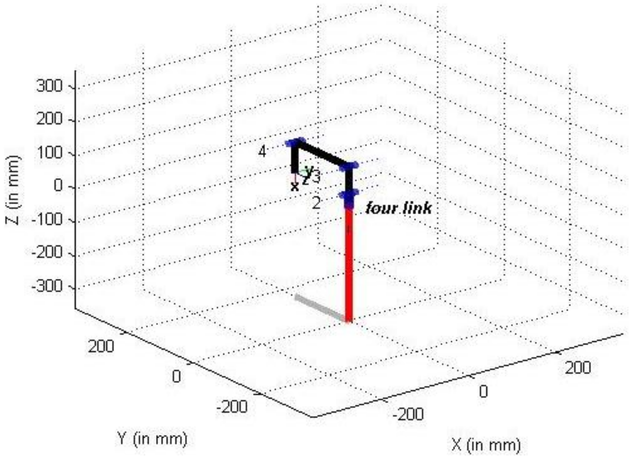

Figure 4.5 : Ready state pose of the robotic arm in Robotic Toolbox.

- **Sample Retrieval Pose**

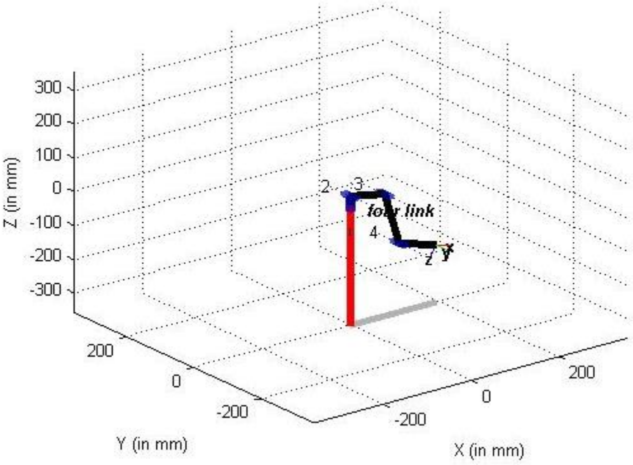

Figure 4.6 : Sample retrieval pose of the robotic arm in Robotic Toolbox.

$$Transformation\ Matrix: \quad H_{14} = \begin{bmatrix} 0.92 & 0 & -0.39 & 194.31 \\ 0 & -1 & 0 & 0 \\ -0.39 & 0 & -0.92 & -187.77 \\ 0 & 0 & 0 & 1 \end{bmatrix} (mm)$$

An example of reaching the ground pose ([0 -0.26 -1.10 0.96] (rad)) for sample retrieval is represented in Figure 4.6. The arm reaches approximately 19.4 cm front and 18.7 cm below the robotic arm base.

- **Storing the Rock Sample Pose**

After holding the sample, the robotic arm will reach the container entrance on the top of the rover main structure, and the final position is presented for ([0 0.45 1.57 1.31] (rad)) in Figure 4.7.

$$Transformation\,Matrix:\quad H_{14}=\begin{bmatrix}-0.98 & 0 & -0.19 & -86.83\\ 0 & -1 & 0 & 0\\ -0.19 & 0 & 0.98 & 186.86\\ 0 & 0 & 0 & 1\end{bmatrix}$$

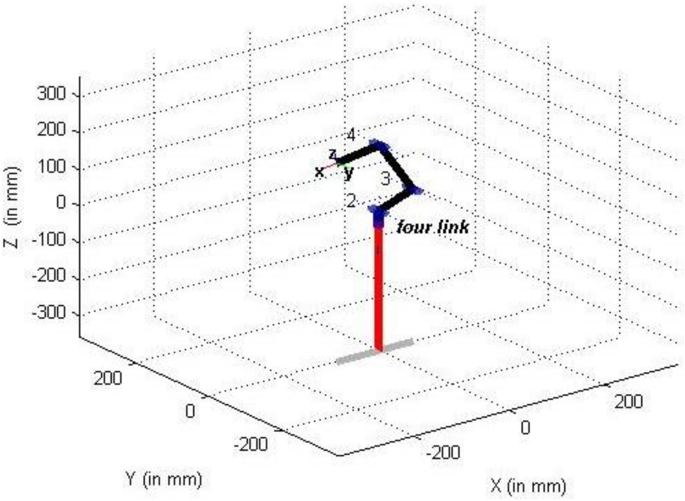

Figure 4.7 : Storing the rock sample of the robotic arm in Robotic Toolbox.

All DH parameters are defined on Matlab Robotic Toolbox, and the robotic arm geometries are created. By using the forward kinematics, the visualization of the arm links' poses are provided, and the animation of the motion is retrieved for crosschecking.

4.2.3 Trajectory Calculation

A path is a spatial construct that leads robotic manipulator arm's links from an initial position to a final position. A trajectory is a path with specified timing or steps. Similarly, positions and orientations of the robotic manipulator arm's links varying smoothly with time is an important characteristic of a trajectory. In the project, it is desired to generate smooth trajectories within the workspace of the robot by using the example poses in the previous section. After retrieving the trajectories, they are imported from Matlab workspace to Simulink model in order to be used in dynamic model to calculate the torques to move robotic arm's links.

Typically, radial velocity and acceleration are required to be continuous. Polynomial function of time is used to retrieve the positions, velocities and acceleration among the example poses. Their derivatives should be continuous in order to vary smoothly by time. These polynomials are simple to compute, and the required boundary conditions and smoothness can be provided. A quintic (fifth-order) polynomial is used in order not to have unexpected vibrations during the arm's motions and they can be expressed as [20]:

$$S(t) = At^5 + Bt^4 + Ct^3 + Dt^2 + Et + F \tag{4.3}$$

$$\dot{S}(t) = 5At^4 + 4Bt^3 + 3Ct^2 + 2Dt + E \tag{4.4}$$

$$\ddot{S}(t) = 20At^3 + 12Bt^2 + 6Ct + 2D \quad where\ time\ t \in [0, T] \tag{4.5}$$

The boundary conditions t = 0 and t = T, which can be derived from the example poses, gives six equations that we can write in general matrix form as:

$$\begin{bmatrix} s_0 \\ s_f \\ \dot{s}_0 \\ \dot{s}_f \\ \ddot{s}_0 \\ \ddot{s}_f \end{bmatrix} = \begin{bmatrix} 0 & 0 & 0 & 0 & 0 & 1 \\ T^5 & T^4 & T^3 & T^2 & T & 1 \\ 0 & 0 & 0 & 0 & 1 & 0 \\ 5T^4 & 4T^3 & 3T^2 & 2T & 1 & 0 \\ 0 & 0 & 0 & 2 & 0 & 0 \\ 20T^3 & 12T^2 & 6T & 2 & 0 & 0 \end{bmatrix} \begin{bmatrix} A \\ B \\ C \\ D \\ E \\ F \end{bmatrix} \tag{4.6}$$

By using this formulation, the following trajectories that consist of positions, velocities and accelerations of each link can be given as:

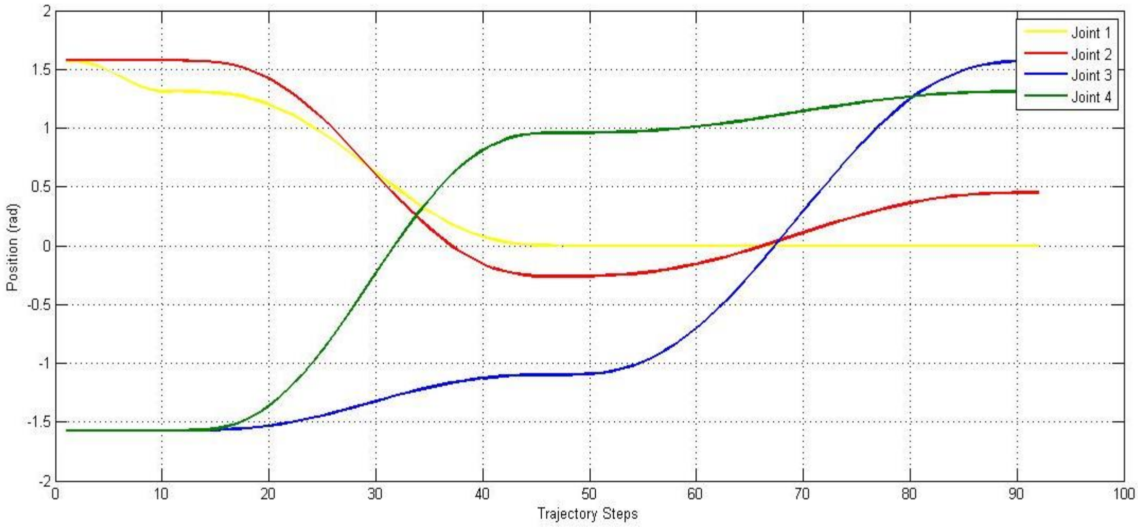

Figure 4.8 : The positions of each joint.

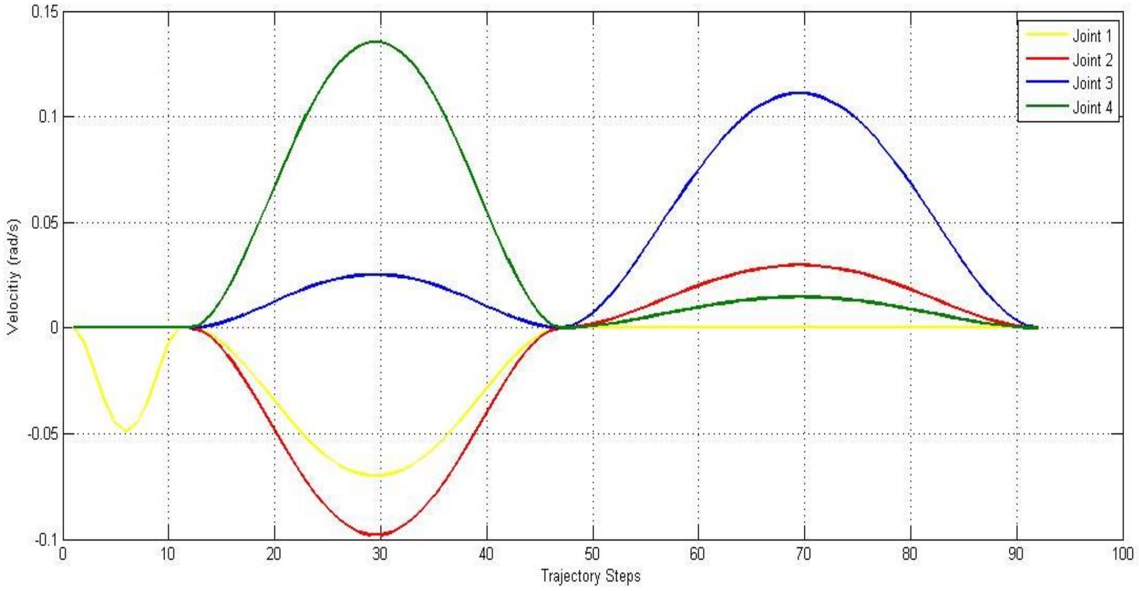

Figure 4.9 : The velocities of each joint.

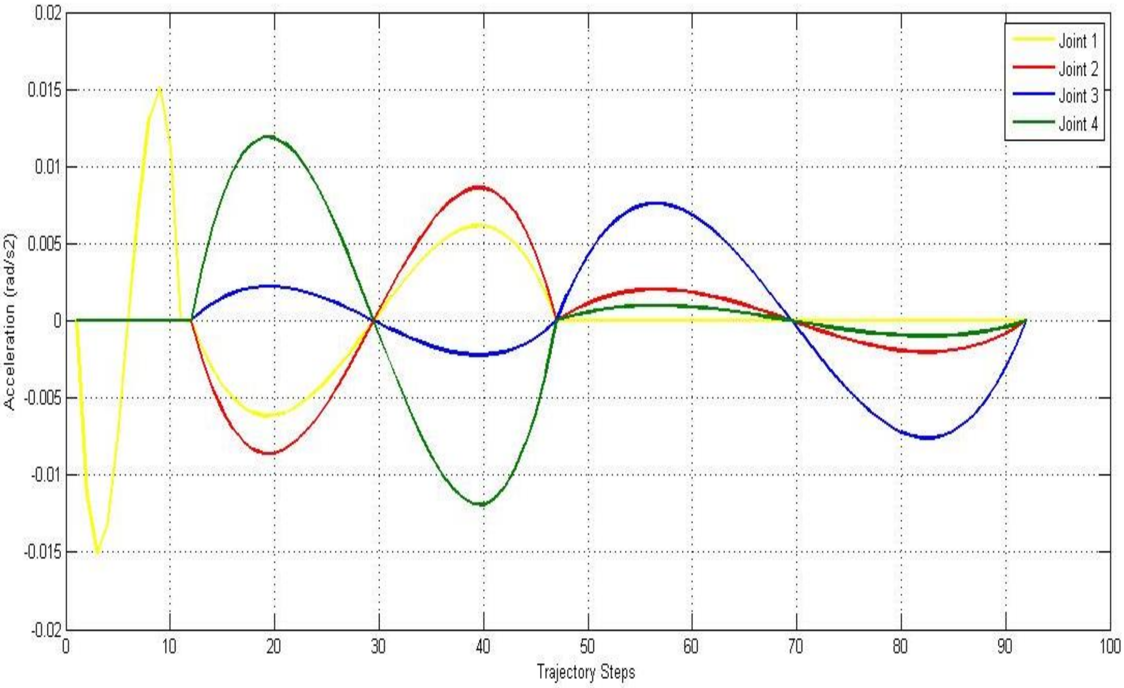

Figure 4.10 : The accelerations of each joint.

4.3 Spatial Operator Algebra for Manipulator Modeling

The Spatial Operator Algebra is a new approach to the mathematics of serial link manipulators as well as multi-body systems. While it reduces mathematical complexity, it eliminates the calculation complications of the high number of symbols. This is the reason why Spatial Operator Algebra is used for modeling instead of continuing with DH convention. In addition, it is easier to use on very complex systems such as multiple robot cooperation tasks.

While the complexity and calculation load is reduced, no information about the system is lost in this approach. The tip velocities and forces can be calculated, and by using dynamics, the system response can easily be seen by the user.

The velocities, forces and accelerations propagate through one rigid body to another, and it is obtained from well-known equivalence between the Lagrangian and recursive Newton-Euler approaches to manipulator dynamics [19].

The Jacobian matrix can be solved numerically after each iteration, and by using Virtual Reality on Matlab, the singularity situations can easily be detected. In addition, it can be seen if there is a problem with the formulization by checking the eigenvalues of the inertia tensor matrix.

In kinematics, the propagation is performed from the base to the tip by using the joint velocities; however, the propagation is made from tip tool to the base in dynamics that can be seen in next sections.

Properties of the Rotation Matrix

The relationship between skew-symmetric matrix and rotation matrix can be given as:

$$\mathrm{R} = (\mathrm{I} - \mathrm{S})^{-1}(\mathrm{I} + \mathrm{S}) \tag{4.7}$$

Since $(AB)^T = B^T A^T$ is known, this relationship can be described as:

$$R^T = (I + S)^T((I - S)^T)^{-1} \tag{4.8}$$

$$R^T = (I - S)\,(I + S)^{-1} \tag{4.9}$$

$$RR^T = (I - S)^{-1}(I + S)(I - S)\,(I + S)^{-1} = I \tag{4.10}$$

Therefore; it can be said that R Є SO (3), and a matrix which shows the rotation about x axis is taken to show the properties of the rotation matrix. It can be written as:

$$R_x(\emptyset) =:= e^{\bar{x}\emptyset} = \begin{bmatrix} 1 & 0 & 0 \\ 0 & cos\emptyset & -sin\emptyset \\ 0 & sin\emptyset & cos\emptyset \end{bmatrix} \quad \textbf{(4.11)}$$

The properties of the rotation matrix can be written as [17]:

- R is normalized: the squares of the elements in any row or column sum to 1.
- R is orthogonal: the dot product of any pair of rows or any pair of columns is 0.
- The rows of R represent the coordinates in the original space of unit vectors along the coordinate axes of the rotated space.

The columns of R represent the coordinates in the rotated space of unit vectors along the axes of the original space.

Rotation matrix preserves the distance and orientation, and determinant of the rotation matrix can be written as:

$$detR = r_1^T(r_2 \text{ x } r_3) \quad \textbf{(4.12)}$$

$$r_2 \text{ x } r_3 = r_1 \quad \textbf{(4.13)}$$

$$detR = r_1^T r_1 = +1 \quad \textbf{(4.14)}$$

Since the columns are mutually orthonormal, it can be written as:

$$r_i^T r_j = \{ \begin{matrix} 0 & if\ i \neq j \\ 1 & if\ i = 1 \end{matrix} \quad \textbf{(4.15)}$$

By taking the columns of the $R_x(\emptyset)$ and applying the rule, it can be shown as:

$$r_1^T r_1 = [1 \quad 0 \quad 0]^T [1 \quad 0 \quad 0] = 1 \quad \textbf{(4.16)}$$

$$r_2^T r_2 = [0 \quad cos\emptyset \quad sin\emptyset]^T [0 \quad cos\emptyset \quad sin\emptyset] = 1 \quad \textbf{(4.17)}$$

$$r_1^T r_3 = [1 \quad 0 \quad 0]^T [0 \quad -sin\emptyset \quad cos\emptyset] = 0 \quad \textbf{(4.18)}$$

$$r_3^T r_3 = [0 \quad -sin\emptyset \quad cos\emptyset]^T [0 \quad -sin\emptyset \quad cos\emptyset] = 1 \quad \textbf{(4.19)}$$

$$r_1^T r_2 = [1 \quad 0 \quad 0]^T [0 \quad cos\emptyset \quad sin\emptyset] = 0 \tag{4.20}$$

$$r_2^T r_3 = [0 \quad cos\emptyset \quad sin\emptyset]^T [0 \quad -sin\emptyset \quad cos\emptyset] = 0 \tag{4.21}$$

The relationship is also the same for the rows. Therefore, when calculating a rotation matrix, it is useful to check the sum the squares of any row or column. If the result is not 1, then surely something is wrong with the calculation.

The relationship between the velocities of two links can be derived from:

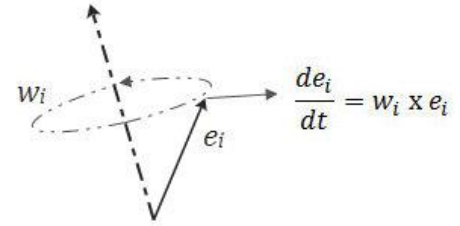

Figure 4.11 : The representation for the differentiation of a vector.

$$\vec{w} \text{ x } \vec{e} = \begin{bmatrix} w_x \\ w_y \\ w_z \end{bmatrix} \text{x} \begin{bmatrix} e_x \\ e_y \\ e_z \end{bmatrix} = \hat{w}.\vec{e} = \begin{bmatrix} 0 & -w_z & w_y \\ w_z & 0 & -w_x \\ -w_y & w_x & 0 \end{bmatrix} . \begin{bmatrix} e_x \\ e_y \\ e_z \end{bmatrix} \tag{4.22}$$

$$\hat{w} = \begin{bmatrix} 0 & -w_z & w_y \\ w_z & 0 & -w_x \\ -w_y & w_x & 0 \end{bmatrix} \quad skew - symmetric\ matrix \tag{4.23}$$

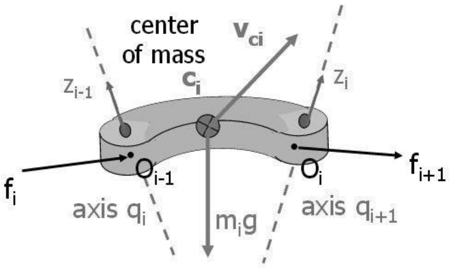

Figure 4.12 : The representation of a link.

$$\vec{w}_i = \vec{w}_{i-1} + \dot{\theta}_i \vec{h}_i \tag{4.24}$$

$$\vec{V}_i = \vec{V}_{i-1} + \vec{w}_{i-1} \text{ x } \vec{l}_{i-1,i} = \vec{V}_{i-1} - \vec{l}_{i-1,i} \text{ x } \vec{w}_{i-1} \tag{4.25}$$

$$\vec{\vec{V}}_i = \begin{bmatrix} \vec{w}_i \\ \vec{V}_i \end{bmatrix} = \begin{bmatrix} I_{(3x3)} & 0_{(3x3)} \\ -\hat{l}_{i-1,i} & I_{(3x3)} \end{bmatrix} . \begin{bmatrix} \vec{w}_{i-1} \\ \vec{V}_{i-1} \end{bmatrix} + \begin{bmatrix} \vec{h}_i \\ 0_{(3x1)} \end{bmatrix} . \dot{\theta}_i \qquad \textbf{(4.26)}$$

$\vec{h}_i$ shows the rotation axis of the ith joint with respect to the reference axis, and it can be retrieved from the relevant column of the rotation matrix. It should be noted that $\begin{bmatrix} \vec{h}_i \\ O_{(3x1)} \end{bmatrix}$ is taken for the rotational joints, and it should be taken as $\begin{bmatrix} O_{(3x1)} \\ \vec{h}_i \end{bmatrix}$ for the translational joints. $\emptyset_{i,i-1}$ is propagation matrix between the serial manipulator links which takes the distance vectors into account.

$$\emptyset_{i,i-1} = \begin{bmatrix} I_{(3x3)} & 0_{(3x3)} \\ -\hat{l}_{i-1,i} & I_{(3x3)} \end{bmatrix} \quad and \;\; H_i = \begin{bmatrix} O_{(3x1)} \\ \vec{h}_i \end{bmatrix} \quad or \quad \begin{bmatrix} \vec{h}_i \\ O_{(3x1)} \end{bmatrix} \qquad \textbf{(4.27)}$$

$$\vec{\vec{V}}_1 = \begin{bmatrix} \vec{w}_1 \\ \vec{V}_1 \end{bmatrix} = \emptyset_{1,base} \vec{\vec{V}}_{base} + H_1 \dot{\theta}_1 \qquad \textbf{(4.28)}$$

$$\vec{\vec{V}}_2 = \emptyset_{21} \vec{\vec{V}}_1 + H_2 \dot{\theta}_2 = \emptyset_{21} \emptyset_{1,base} \vec{\vec{V}}_{base} + \emptyset_{21} H_1 \dot{\theta}_1 + H_2 \dot{\theta}_2 \qquad \textbf{(4.29)}$$

$$\begin{aligned} \vec{\vec{V}}_3 &= \emptyset_{32} \vec{\vec{V}}_2 + H_3 \dot{\theta}_3 = \emptyset_{32} [\left(\emptyset_{21} \emptyset_{1,base} \vec{\vec{V}}_{base} \right) \\ &\quad + (\emptyset_{21} H_1 \dot{\theta}_1 + H_2 \dot{\theta}_2)] + H_3 \dot{\theta}_3 . \end{aligned} \qquad \textbf{(4.30)}$$

This can be written in matrix form as:

$$\begin{bmatrix} \vec{\vec{V}}_1 \\ \vec{\vec{V}}_2 \\ \vec{\vec{V}}_3 \\ \vec{\vec{V}}_4 \end{bmatrix} = \begin{bmatrix} I & 0 & 0 & 0 \\ \emptyset_{21} & I & 0 & 0 \\ \emptyset_{31} & \emptyset_{32} & I & 0 \\ \emptyset_{41} & \emptyset_{42} & \emptyset_{43} & I \end{bmatrix} . \begin{bmatrix} \vec{\vec{H}}_1 & 0 & 0 & 0 \\ 0 & \vec{\vec{H}}_2 & 0 & 0 \\ 0 & 0 & \vec{\vec{H}}_3 & 0 \\ 0 & 0 & 0 & \vec{\vec{H}}_4 \end{bmatrix} . \begin{bmatrix} \dot{\theta}_1 \\ \dot{\theta}_2 \\ \dot{\theta}_3 \\ \dot{\theta}_4 \end{bmatrix} \qquad \textbf{(4.31)}$$

Tip point velocities can be calculated by using:

$$\vec{V}_t = \begin{bmatrix} \vec{0} & \dots & \vec{0} \begin{bmatrix} I_{(3x3)} & 0_{(3x3)} \\ -\hat{l}_{4t} & I_{(3x3)} \end{bmatrix} \\ \vec{0} & \dots & \vec{0} \end{bmatrix} . \begin{bmatrix} I & 0 & 0 & 0 \\ \emptyset_{21} & I & 0 & 0 \\ \emptyset_{31} & \emptyset_{32} & I & 0 \\ \emptyset_{41} & \emptyset_{42} & \emptyset_{43} & I \end{bmatrix} \qquad \textbf{(4.31)}$$

$$\cdot\begin{bmatrix} \overset{\rightrightarrows}{H}_1 & 0 & 0 & 0 \\ 0 & \overset{\rightrightarrows}{H}_2 & 0 & 0 \\ 0 & 0 & \overset{\rightrightarrows}{H}_3 & 0 \\ 0 & 0 & 0 & \overset{\rightrightarrows}{H}_4 \end{bmatrix} \cdot \begin{bmatrix} \dot{\theta}_1 \\ \dot{\theta}_2 \\ \dot{\theta}_3 \\ \dot{\theta}_4 \end{bmatrix}$$

Therefore, the Jacobian Matrix for a single manipulator is retrieved from:

$$J = \left[\begin{matrix} \vec{0} \ldots \vec{0} \\ \vec{0} \ldots \vec{0} \end{matrix} \begin{bmatrix} I_{(3x3)} & 0_{(3x3)} \\ -\hat{l}_{4t} & I_{(3x3)} \end{bmatrix}\right] \cdot \begin{bmatrix} I & 0 & 0 & 0 \\ \emptyset_{21} & I & 0 & 0 \\ \emptyset_{31} & \emptyset_{32} & I & 0 \\ \emptyset_{41} & \emptyset_{42} & \emptyset_{43} & I \end{bmatrix} \cdot \begin{bmatrix} \overset{\rightrightarrows}{H}_1 & 0 & 0 & 0 \\ 0 & \overset{\rightrightarrows}{H}_2 & 0 & 0 \\ 0 & 0 & \overset{\rightrightarrows}{H}_3 & 0 \\ 0 & 0 & 0 & \overset{\rightrightarrows}{H}_4 \end{bmatrix} \quad \textbf{(4.32)}$$

Jacobian Matrix for Two Serial Manipulators on a Mobile Platform can be written as:

$$\overset{\rightrightarrows}{V}_t = J\dot{\theta} + \emptyset_{tb}\overset{\rightrightarrows}{V}_b \quad \textbf{(4.33)}$$

$$\begin{bmatrix} \overset{\rightrightarrows}{V}_b \\ \overset{\rightrightarrows}{V}_t \end{bmatrix} = [\emptyset_{tb} \quad J] . \begin{bmatrix} \overset{\rightrightarrows}{V}_b \\ \dot{\theta} \end{bmatrix} \quad \textbf{(4.34)}$$

$\emptyset_{tb} = \emptyset_t \, \emptyset \, \emptyset_b \quad : the\ propogation\ matrix\ from\ base\ to\ tip\ point$

$$\emptyset_{tb} = \left[\begin{matrix} \vec{0} & \ldots & \vec{0} \\ \vec{0} & \ldots & \vec{0} \end{matrix} \begin{bmatrix} I_{(3x3)} & 0_{(3x3)} \\ -\hat{l}_{bt} & I_{(3x3)} \end{bmatrix}\right] \cdot \begin{bmatrix} I & 0 & 0 & 0 \\ \emptyset_{21} & I & 0 & 0 \\ \emptyset_{31} & \emptyset_{32} & I & 0 \\ \emptyset_{41} & \emptyset_{42} & \emptyset_{43} & I \end{bmatrix} \cdot \begin{bmatrix} \emptyset_{1b} \\ 0 \\ \vdots \\ 0 \end{bmatrix} \quad \textbf{(4.35)}$$

In the compact form, this can be written as:

$$V_t = J\dot{\theta} \quad and\ \dot{\theta} = J^{\#}\, V_t \quad \textbf{(4.36)}$$

$$J^{\#} = J^T(J.J^T)^{-1} \quad \textbf{(4.37)}$$

Therefore, when tip point velocities or accelerations are given, the joint velocities can be derived by using Jacobian matrix. In singularity situations, the Jacobian matrix loses rank and the modelling cannot work orderly, and it was observed within the output on Virtual Reality while arm motions were senseless since the given point was not reachable.

The tip point velocities can be dependent on the motion of the carried load, and by giving a motion to the carried rock sample in Simulink model; the tip forces and velocities can be derived by using the formulas:

$$\vec{\vec{V}}_t = \emptyset_{tc}\vec{\vec{V}}_c \quad and \quad \vec{\vec{F}}_t = \emptyset_{tc}\vec{\vec{F}}_c \tag{4.38}$$

It is seen that the propagation matrix $\emptyset_{tc}$ is needed if the tip tool axis and the carried rock sample origin axis are in different places; however, the rock sample origin axis and the tip tool axis are taken in the same spot in our model since it would be inside of the handling mechanism.

Therefore, the force and velocity relations will be simplified as:

$$\vec{\vec{V}}_t = \vec{\vec{V}}_c \quad and \quad \vec{\vec{F}}_t = \vec{\vec{F}}_c \quad \text{where } \emptyset_{tc} \; is\ a\ unit\ matrix \tag{4.39}$$

The Range Space and Null Space

If we consider a vector space X of dimension n and a vector space Y of dimension m with $m \leq n$, the linear transformation between the vectors belong to the X and Y vector spaces have a relation as:

$$y = Ax \tag{4.40}$$

We can describe A term as a linear operator which pairs the vectors from the space X of dimension n and the space Y of dimension m. Therefore, it can be described as the matrix A of dimensions (m x n).

$$\mathcal{R}(A) = \{y : \; y = Ax, \quad x \in X\} \quad \subseteq Y \tag{4.41}$$

On the other hand, the null space of the transformation is the subspace which can be described as:

$$\mathcal{N}(A) = \{x : Ax = 0, \quad x \in X\} \quad \subseteq X \tag{4.42}$$

While a matrix A of dimensions (m x n) is given, it can be given as:

$$\rho(A) = \dim(\mathcal{R}(A)) \tag{4.43}$$

$$\rho(A) + \dim\big(\mathcal{N}(A)\big) = n \tag{4.44}$$

As it is seen in the previous equation, the dimension n can be found as the sum of range space and null space dimensions. It is stated in ITU Modelling and Control of Robot Manipulators lecture that if $x \in \mathcal{N}(A)$ and $y \in \mathcal{R}(A^T)$, then $y^T x = 0$. It can be described further as the vectors in the null space of A are orthogonal to each vector in range space of the transpose of matrix A. Therefore, the set of vectors orthogonal to each vector of the range space of A^T coincides with the null space of A. This statement can be shown as:

$$\mathcal{N}(A) \equiv \mathcal{R}^{\perp}(A^T) \tag{4.45}$$

Moreover, the set of vectors orthogonal to each vector in the null space of A^T coincides with the range space of A. This statement also can be shown as:

$$\mathcal{R}(A) \equiv \mathcal{N}^{\perp}(A^T) \tag{4.46}$$

4.3.1 Dynamics

The acceleration of translational and rotational velocities can be expressed as:

$$\dot{\vec{w}}_k = \dot{\vec{w}}_{k-1} + \vec{h}_k \ddot{\theta}_k + \vec{w}_{k-1} x\, \vec{w}_k \tag{4.47}$$

$$\dot{\vec{V}}_k = \dot{\vec{V}}_{k-1} - \vec{l}_{k-1,k}\; x\; \dot{\vec{w}}_{k-1} + \vec{w}_{k-1} x (\vec{w}_{k-1}\; x\; \vec{l}_{k-1,k}) \tag{4.48}$$

To write the accelerations in a compact form, the propagation matrix can be used as:

$$\begin{bmatrix} \dot{\vec{w}}_k \\ \dot{\vec{V}}_k \end{bmatrix} = \begin{bmatrix} I_{(3x3)} & 0_{(3x3)} \\ -\hat{l}_{k,k-1} & I_{(3x3)} \end{bmatrix} \cdot \begin{bmatrix} \dot{\vec{w}}_{k-1} \\ \dot{\vec{V}}_{k-1} \end{bmatrix} + \begin{bmatrix} \vec{h}_i \\ O_{(3x1)} \end{bmatrix} \ddot{\theta}_k + \begin{bmatrix} \vec{w}_{k-1} \mathrm{x}\, \vec{w}_k \\ \vec{w}_{k-1} x (\vec{w}_{k-1}\; \mathrm{x}\; \vec{l}_{k-1,k}) \end{bmatrix} \tag{4.49}$$

$$\vec{\vec{V}}_k = \emptyset_{k,k-1} \vec{\vec{V}}_{k-1} + \vec{\vec{H}}_k \ddot{\theta}_k + \vec{\vec{a}}_k \tag{4.50}$$

$$\vec{\vec{a}}_k = \begin{bmatrix} \vec{w}_{k-1} \mathrm{x}\, \vec{w}_k \\ \vec{w}_{k-1} x (\vec{w}_{k-1}\; \mathrm{x}\; \vec{l}_{k-1,k}) \end{bmatrix} \tag{4.51}$$

$$\begin{bmatrix} \dot{V}_1 \\ \dot{V}_2 \\ \dot{V}_3 \\ \dot{V}_4 \end{bmatrix} = \begin{bmatrix} I & 0 & 0 & 0 \\ \emptyset_{21} & I & 0 & 0 \\ \emptyset_{31} & \emptyset_{32} & I & 0 \\ \emptyset_{41} & \emptyset_{42} & \emptyset_{43} & I \end{bmatrix} \cdot \left\{ \left(\begin{bmatrix} \vec{\vec{H}}_1 & 0 & 0 & 0 \\ 0 & \vec{\vec{H}}_2 & 0 & 0 \\ 0 & 0 & \vec{\vec{H}}_3 & 0 \\ 0 & 0 & 0 & \vec{\vec{H}}_4 \end{bmatrix} \cdot \begin{bmatrix} \ddot{\theta}_1 \\ \ddot{\theta}_2 \\ \ddot{\theta}_3 \\ \ddot{\theta}_4 \end{bmatrix} + \begin{bmatrix} \vec{\vec{a}}_1 \\ \vec{\vec{a}}_2 \\ \vec{\vec{a}}_3 \\ \vec{\vec{a}}_4 \end{bmatrix} \right) \right\} \tag{4.52}$$

4.3.2 Calculation of Torques and Forces

$$\vec{\tau}_k = \tau_{k+1} + \vec{l}_{k,k+1} \text{ x } \vec{f}_{k+1} + \vec{l}_{k,c} \text{ x } \dot{\vec{v}}_k m_k + \frac{d}{dt}(I_k \vec{w}_k) \qquad \textbf{(4.53)}$$

Torque vector of k^th^ joint = torque vector of k+1^th^ link + torque vector resulting from the k+1^th^ joint's force + torque resulting from the link's own translational motion + torque resulting from the joints own rotational motion (Euler Equation).

$$\vec{f}_k = f_{k+1} + m_k \frac{d}{dt}(\vec{V}_k + \vec{w}_k \text{ x } \vec{l}_{k,c}) \qquad \textbf{(4.53)}$$

Force vector of k^th^ joint = Force vector of k+1^th^ link + force resulting from the joints' own motions (Newton equation).

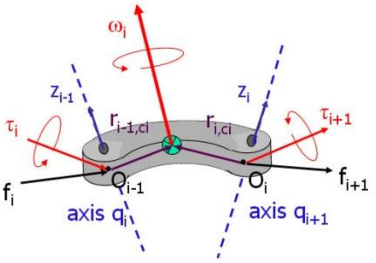

Figure 4.13 : The representation of a link.

All forces and torques can be written in a compact form as:

$$\begin{bmatrix} \vec{\tau}_k \\ \vec{f}_k \end{bmatrix} = \begin{bmatrix} I_{(3x3)} & \hat{l}_{k,k+1} \\ O_{(3x3)} & I_{(3x3)} \end{bmatrix} \cdot \begin{bmatrix} \vec{\tau}_{k+1} \\ \vec{f}_{k+1} \end{bmatrix} + \begin{bmatrix} I_k & m_k \hat{l}_{kc} \\ -m_k \hat{l}_{kc} & m_k . I_{(3x3)} \end{bmatrix} \cdot \begin{bmatrix} \dot{\vec{w}}_k \\ \dot{\vec{V}}_k \end{bmatrix} + \begin{bmatrix} \vec{w}_k \text{ x } I_k \vec{w}_k \\ m_k \vec{w}_k \text{x}(\vec{w}_k \text{ x } \vec{l}_{k,c}) \end{bmatrix} \qquad \textbf{(4.54)}$$

$$\vec{\vec{F}}_k = \emptyset_{k,k-1}{}^T \, \vec{\vec{F}}_{k+1} + M_k \dot{\vec{\vec{V}}}_k + \vec{\vec{b}}_k \qquad where\ \vec{\vec{b}}_k = \begin{bmatrix} \vec{w}_k \text{ x } I_k \vec{w}_k \\ m_k \vec{w}_k \text{x}(\vec{w}_k \text{ x } \vec{l}_{k,c}) \end{bmatrix} \qquad \textbf{(4.55)}$$

Throughout to degree of freedom, the translated torques and forces are equal to zero. Unless they are equal to zero, there should be some force affecting the system, which can be attempting a motion against the actuators.

$$\begin{bmatrix} \vec{\vec{F}}_1 \\ \vec{\vec{F}}_2 \\ \vec{\vec{F}}_3 \\ \vec{\vec{F}}_4 \end{bmatrix} = \begin{bmatrix} I & \emptyset_{21} & \emptyset_{31} & \emptyset_{41} \\ 0 & I & \emptyset_{32} & \emptyset_{42} \\ 0 & 0 & I & \emptyset_{43} \\ 0 & 0 & 0 & I \end{bmatrix} \cdot \left\{ \begin{bmatrix} M_1 & 0 & 0 & 0 \\ 0 & M_2 & 0 & 0 \\ 0 & 0 & M_3 & 0 \\ 0 & 0 & 0 & M_4 \end{bmatrix} \cdot \begin{bmatrix} \dot{V}_1 \\ \dot{V}_2 \\ \dot{V}_3 \\ \dot{V}_4 \end{bmatrix} + \begin{bmatrix} b_1 \\ b_2 \\ b_3 \\ b_4 \end{bmatrix} \right. \tag{4.56}$$

$$\left. + \begin{bmatrix} 0 \\ 0 \\ 0 \\ \emptyset_{4t}^T \end{bmatrix} \vec{\vec{F}}_t \right\}$$

Since $\tau = H^T F$ and $\vec{\vec{V}}_k = \emptyset_{k,k-1} \vec{\vec{V}}_{k-1} + \vec{\vec{H}}_k \ddot{\theta}_k + \vec{\vec{a}}_k$ are known, this can be written in a compact form as:

$$F = \emptyset^T M \emptyset H \ddot{\theta} + \emptyset^T M \emptyset a + \emptyset^T b + \emptyset^T \emptyset_t^T F_t \tag{4.57}$$

$$\tau = H^T \emptyset^T M \emptyset H \ddot{\theta} + H^T \emptyset^T (M \emptyset a + b) + H^T \emptyset^T \emptyset_t^T F_t \tag{4.58}$$

The elements of the Dynamics Equations [18, 22]:

$$Inverse\ Dynamics\ Model: \qquad \tau = M\ddot{\theta} + C + J^T F_t \tag{4.59}$$

$$Forward\ Dynamics\ Model: \qquad \ddot{\theta} = M^{-1}[\tau - C - J^T F_t] \tag{4.60}$$

$$Coriolis\ matrix: \qquad C = H^T \emptyset^T (M \emptyset a + b) \tag{4.61}$$

$$Inertia\ Tensor\ Matrix: \qquad M = H^T \emptyset^T M\, \emptyset\, H \tag{4.62}$$

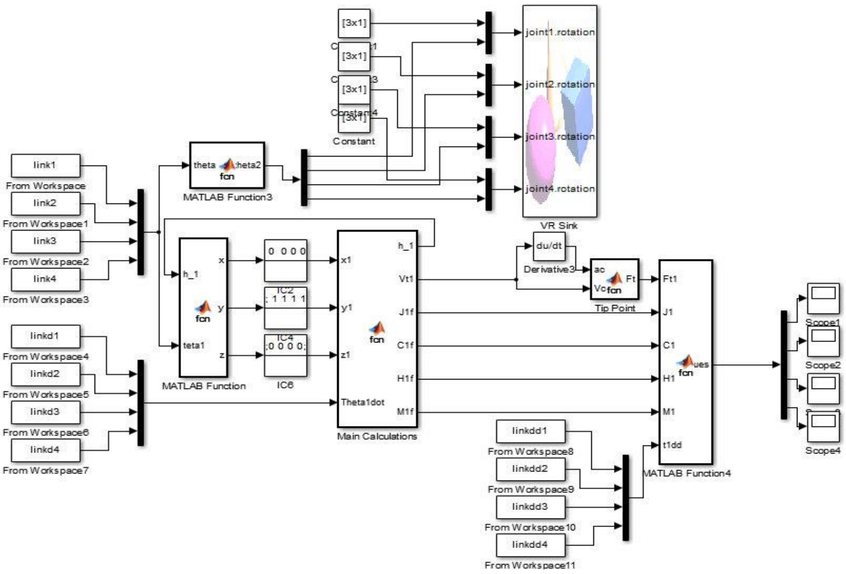
[3x1]
[3x1]
[3x1]
[3x1]
Constant4
Constant
joint1.rotation
joint2.rotation
joint3.rotation
joint4.rotation
VR Sink
link1
From Workspace
link2
From Workspace1
link3
From Workspace2
link4
From Workspace3
linkd1
From Workspace4
linkd2
From Workspace5
linkd3
From Workspace6
linkd4
From Workspace7
theta
theta2
fcn
MATLAB Function3
h_1
teta1
x
y
z
MATLAB Function
0 0 0 0
IC2
; 1 1 1 1
IC4
;0 0 0 0;
IC6
x1
y1
z1
Theta1dot
h_1
Vt1
J1f
C1f
H1f
M1f
Main Calculations
du/dt
Derivative3
ac
Vc
Ft
Tip Point
Ft1
J1
C1
H1
M1
t1dd
ues
MATLAB Function4
linkdd1
From Workspace8
linkdd2
From Workspace9
linkdd3
From Workspace10
linkdd4
From Workspace11
Scope1
Scope2
Scope4

Figure 4.14 : Simulink model of the robotic manipulator system.

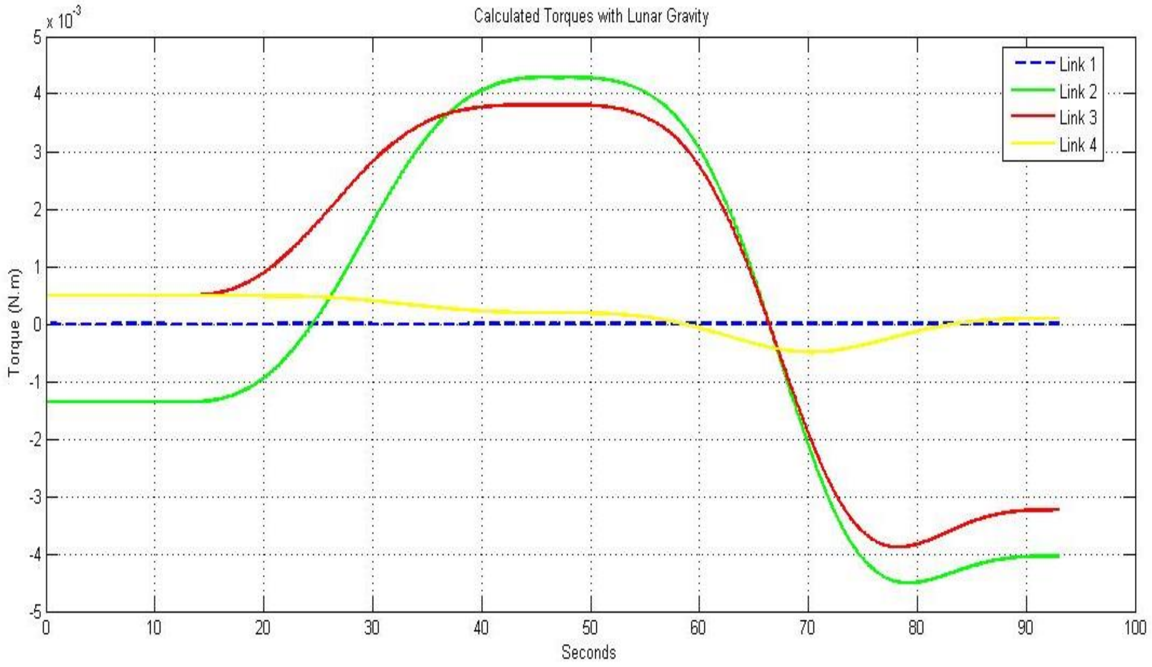

Figure 4.15 : Torques for each link with lunar gravity.

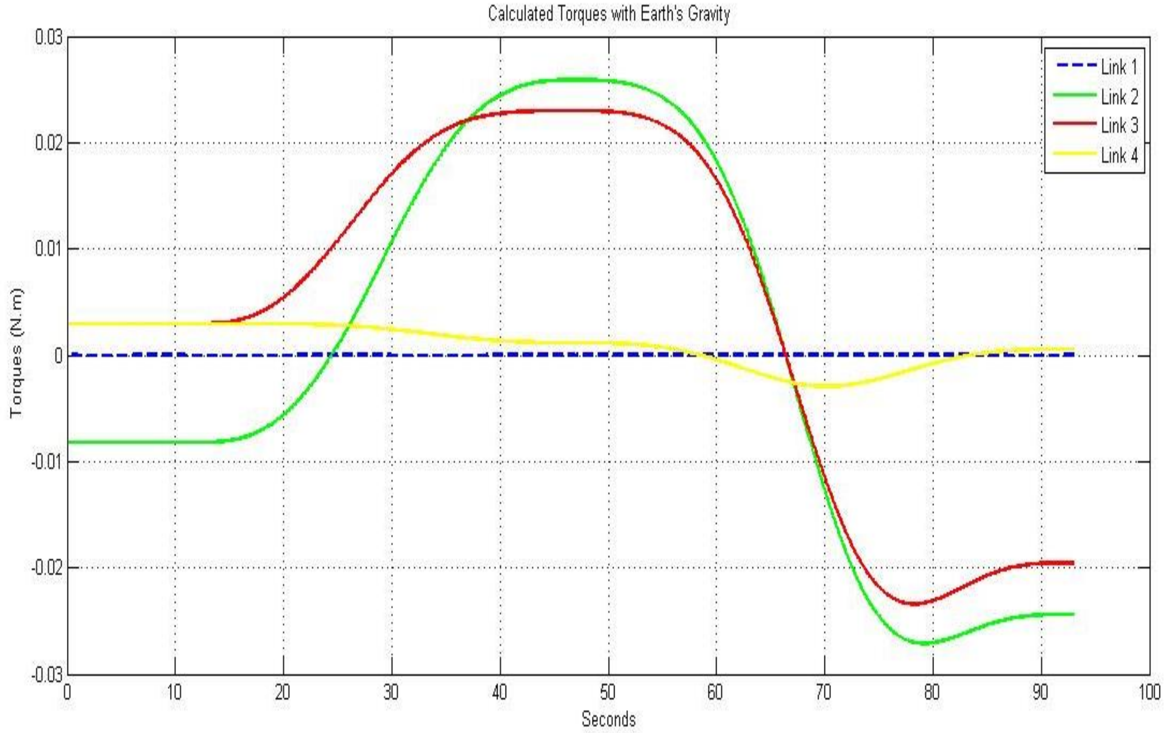

Figure 4.16 : Torques for each link with gravity of Earth.

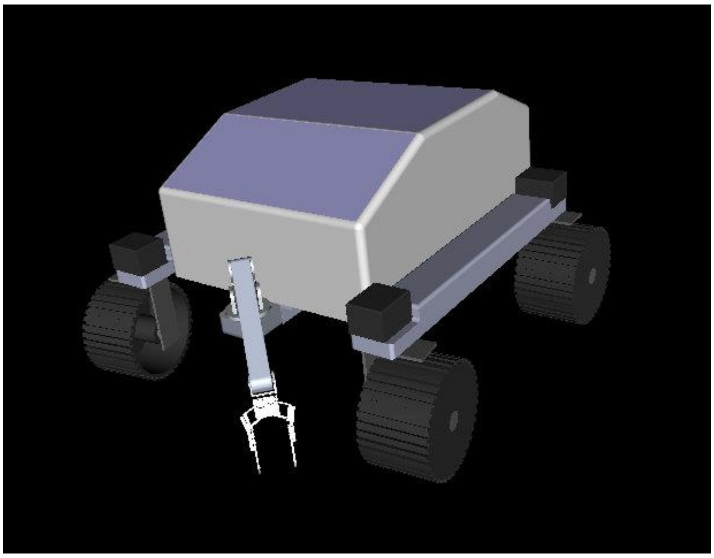

Figure 4.17 : Virtual reality screenshot in Matlab.

4.4 Conclusion

By only giving input for the links' motions, the joints' torques are derived for the given system, and for the poses, which robotic manipulators cannot reach, the singularity of the Jacobian matrix is observed. The computational complexity of each iteration remained constant, and it grows in a linear fashion with the number of joints increases. It is strongly recommended for real-time use in some studies, especially when the number of joints is large. In addition, a closed-form dynamic model is obtained which the same to the one is obtained by using DH parameters.

The inertia tensor matrix shows all mass and inertial properties of the robotic systems, and it is very important to be derived for understanding the dynamics of a robotic system since the inertia of the manipulator should be surpassed in order to move the links. Therefore, the effect of Moon and Earth's gravity ratio is observed in the torques. Since the robotic arms' motion is determined to be slow, Coriolis Effect is not strong. Moreover, the profile of the torque graphs seems to be very similar; however, the magnitude of the torque's ratio is very close to the ratio of the gravity, which is approximately 1/6.

5. ENVIRONMENT RECOGNITION AND PATH PLANNING

5.1 Image Processing

Image processing is a computational process within the robot, which transforms the scene of the environment to an output digital image. The process of the feature extraction is one of the important aspects of the understanding the environment, and due to noise, reflection, shadows and lunar dust on the camera lens creates imperfect images.

A lunar micro rover is a small self-sufficient robot that is capable of autonomous local navigation; therefore, the rover needs to retrieve a detailed map of its environment and sense the objects in order to decide its actions carefully. To achieve these abilities, rover must have sensors, instruments and processing power as well as electrical power. For the lunar micro-rover perception of the environment, the first step would be forming and capturing the images to have information before starting to operate as seen in Figure 5.1. From these images, the robot can comprehend the size, the shape and the position of the objects around itself. By using a digital camera, it forms a digital image by using its light sensitive parts, and it involves the projection of three-dimensional world onto a two-dimensional image. Therefore, the depth information would be lost, and the robot would not be able to decide the sizes and distances of the objects around it.

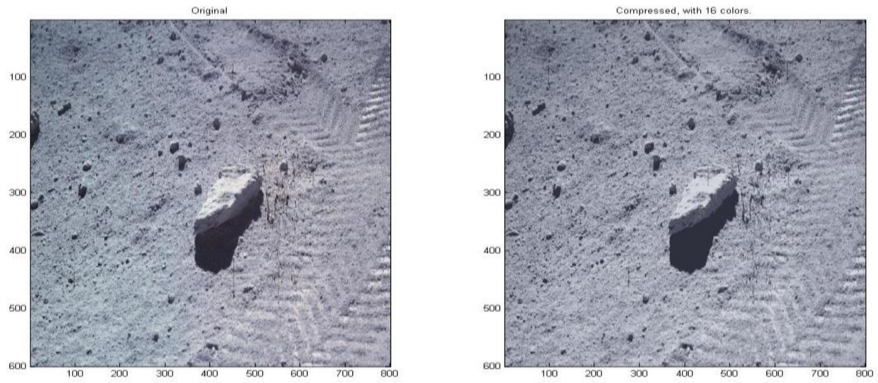

Figure 5.1 : Compressed rock image.

Surface rock samples were intended to be detected with black and white camera images at first by using their shadows. The software would use the images and histogram distribution, and the dark side of the rock sample would not be confused with the shadow on the surface in Figure 5.2. In addition, a filter was added to the software to clear the small dark areas on the surface before the feature extraction. *Sun elevation angle*, the *sizes of the shadows*, and the *angle of the camera* were planned to be used to spot the rock samples and to calculate *approach angle* to the surface if the sample would be retrieved.

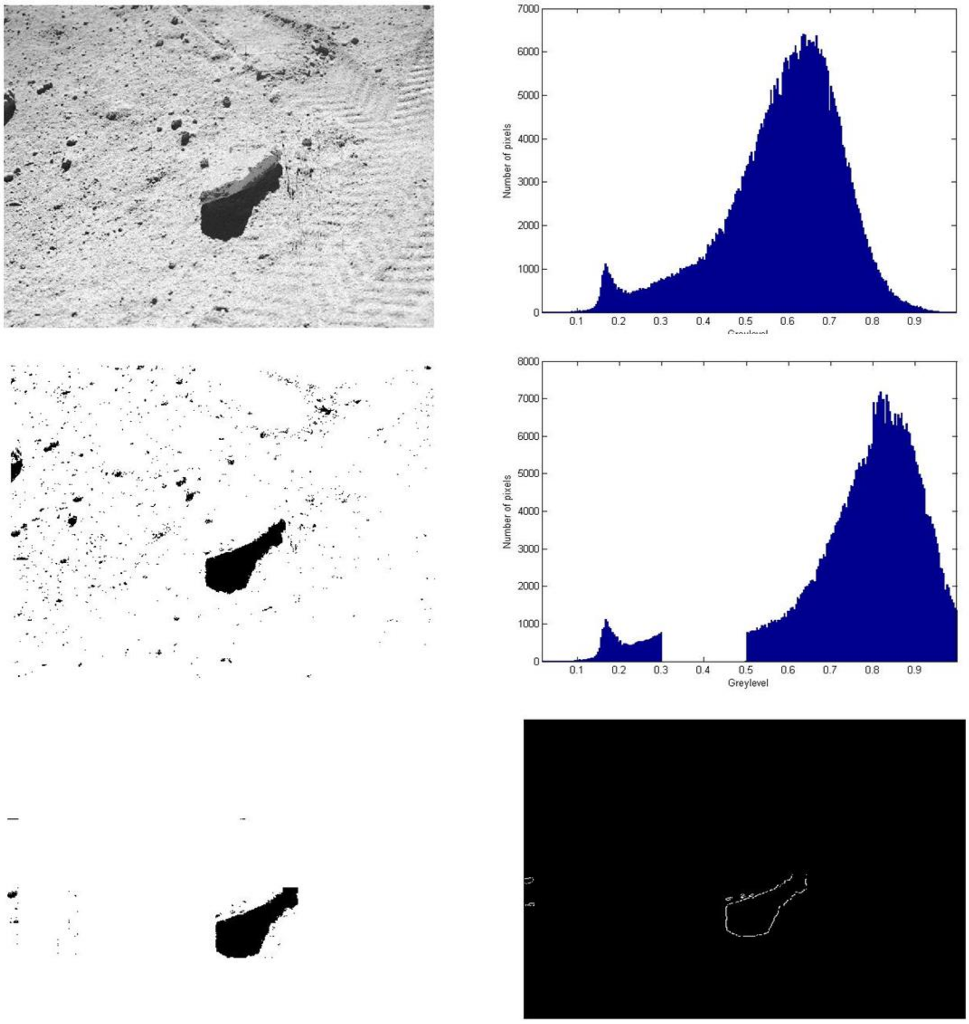

Figure 5.2 : Rock sample example and image processing.

The black and white image of the possible rock sample was used in the Matlab code. By using the histogram distribution, the side of the rock is also turned closer to white since the program would estimate it as shadow because it does not reflect the sunlight as much as the upper surface as seen in Figure 5.2. In addition, the rock image is compressed to save computation time and power as seen in Figure 5.1.

The main problem and risk of this system is that it cannot classify the shadow areas whether they are caused by an obstacle (rocks, rises etc.) or a hollow [23]. For this reason, an additional system is needed such as an active laser triangulation system.

5.2 Triangulation

5.2.1 Introduction

Triangulation can be described as estimating the position of an unknown point by measuring the relative angles from each of the known points [24]. Rather than measuring the distances to the unknown point directly, triangulation process measures the angles to it from known points to determine the location of that point. It is represented in Figure 5.3.

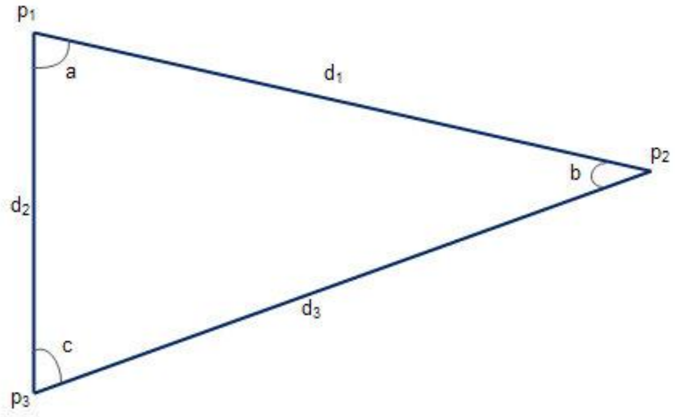

Figure 5.3 : Triangulation configuration.

$$d_1 = d_2 \frac{sinc}{sinb} = d_2 \frac{sinb}{\sin(a+b)} \qquad \textbf{(5.1)}$$

An optic triangulation sensor can be either passive or active. Passive triangulation or stereoscopic systems, which are only using the ambient light of the scene, use two cameras to capture the interested scene, and the triangles with a fixed baseline are defined by the lens central points of each camera along with each point on the scene. The interior angles can be calculated if the focal distances of both cameras are known [25].

Considering the main problem of passive triangulation systems as the identification of the corresponding points, active triangulation systems uses a projecting light source instead of second camera. Using a laser beam and identifying those points by using a CCD or CMOS camera could be a simple choice [25].

5.2.2 Laser Triangulation

The laser triangulation system is used to determine the depth of a point of the environment. The system typically consists of a low-power laser diode to point an object of interest and a CMOS or CCD camera to detect the reflection of the laser from the surface [26]. A laser dot or line can be used in the detection of an object, and how far away the laser reflects on the surface changes positions of appearance in the camera’s field of view. In addition, the deformation of the laser line on a surface could be analyzed to understand the surface properties such as inclination, height, depth etc. This kind of sensor can be used as an “eye” of the lunar micro-rover.

The positions of the camera, the laser emitter and the point of interest forms a triangle; therefore, the triangulation technique can be used in the robotic system. By sweeping the laser stripe across an object, the features of the object can be retrieved by the camera and a proper algorithm; however, the parameters of the system such as *the distance between camera and laser emitter, the laser emitter angle with respect to the surface* must be known. The National Research Council of Canada was among the first institutes to develop the triangulation based laser scanning technology in 1978 [27].

5.3 Active Laser Triangulation System

A triangulation based range sensor may be constructed by adding a laser stripe projector and a top-mounted camera on the micro-rover, and the laser beam must be tilted down since the laser stripe is desired to sweep the terrain ahead of the lunar micro-rover. Then, the robot can sense the hazards and map the terrain ahead at the same time.

Active laser sensors offer more reliable terrain perception than most of the vision based approaches, and they consumes usually a small portion of the computing power that required by passive vision [28]. While 3D laser scanners are bulky, power consuming and expensive, active laser triangulation sensors are miniature, lightweight and low-cost, which means it is suitable for a lunar micro-rover.

Stereo-based planner is reasonably reliable; however, the main deficiency is that stereo vision often cannot detect craters while reporting them as unknown areas. In addition, small obstacles may be overlooked; therefore, it can cause problems, and the vehicle can hit the bottom of itself [23].

Objectives:

- Being low-cost
- Providing hazard detection
- Mapping terrain
- Consuming low power
- Being light weight
- Having a high response speed
- Having a high sampling frequency

Challenges:

- Measurement uncertainties
- Light variations (the ambient light)
- Different reflective surface properties

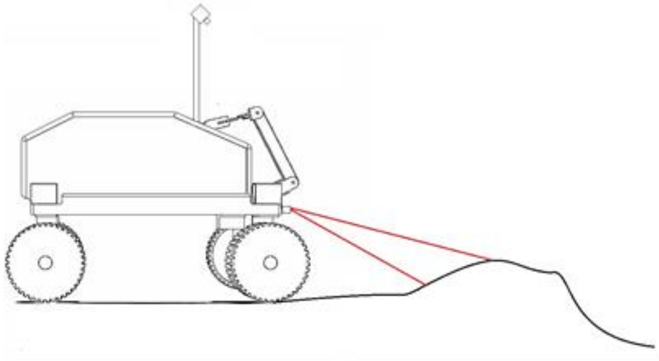

Figure 5.4 : Active laser triangulation system on LMR.

Table 5.1 : Hazard detection types.

LMR Limits	Possible Hazards
Inclination	Various sized rocks, step in terrain
Declination	Craters, trenches, cracks on the rock surfaces
Hitting the Bottom of LMR	Objects on the peak of slopes

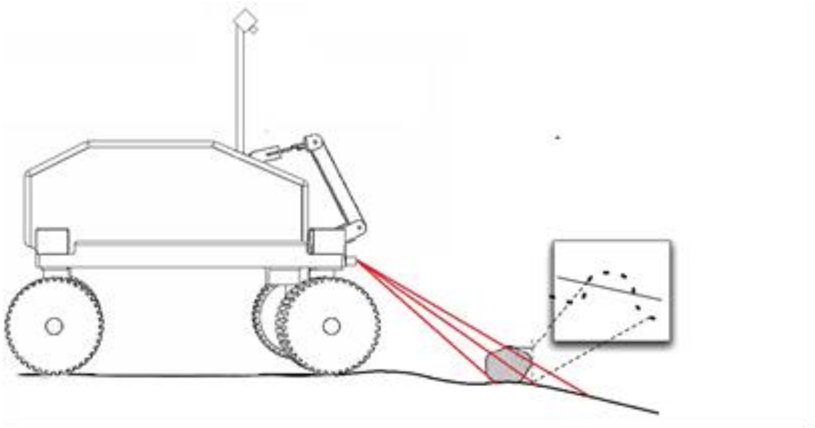

Figure 5.5 : Obstacle detection by active laser triangulation.

An optical filter can help to overcome the ambient light variations in outdoor environments according to the wavelength of the laser emitter. In addition, the ambient light variations can be detected by using a sun sensor. On the lunar surface, there will not be weather changes as on Earth, and it will be easier to adapt the system to the ambient light variations than on Earth. The side and top view of the system is represented in Figure 5.5 and Figure 5.6.

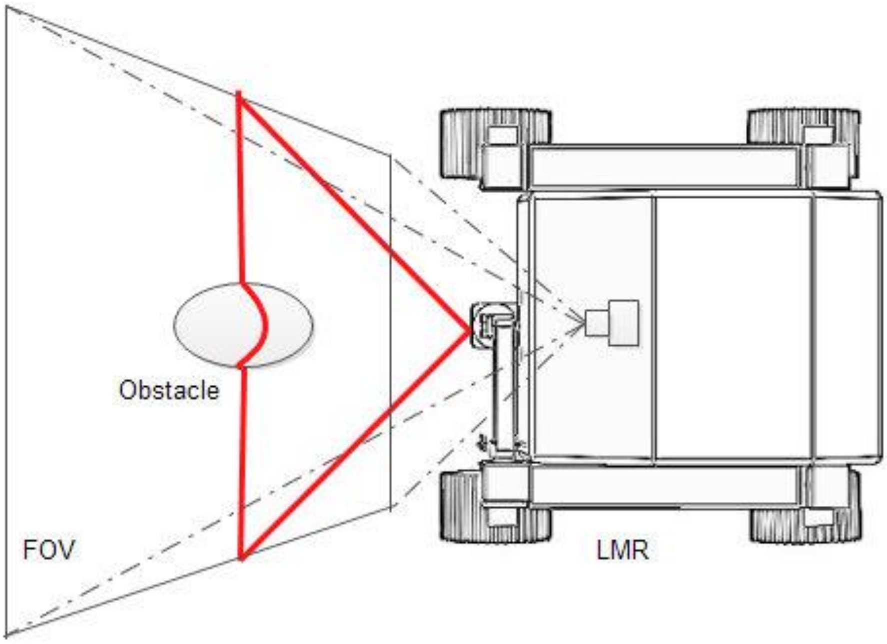

Figure 5.6 : Top view of active laser triangulation system.

5.3.1 Formulization

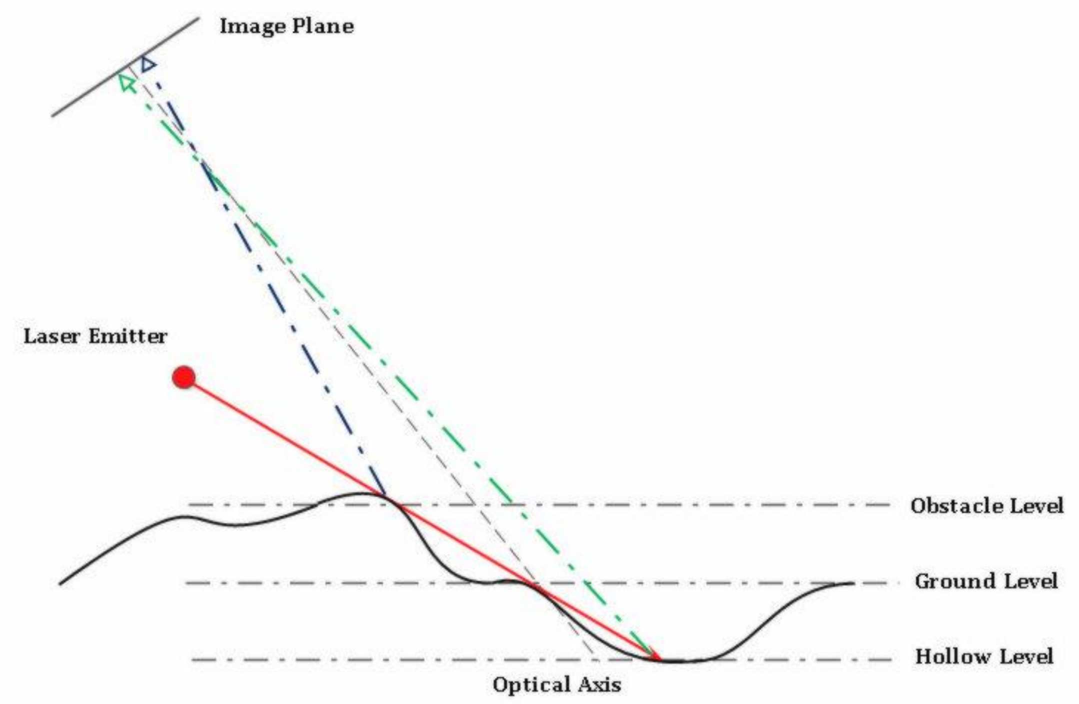

Figure 5.7 : Hazard detection configuration.

The active laser triangulation system is represented with a laser emitter and a camera placed at a certain lateral distance in Figure 5.7 above, and the main challenge of the active triangulation system is how to detect the laser reflection from the lighted surfaces in the camera. Ideally, the red color pixels in the image plane would correspond to the laser reflection. The distance and the height of the surfaces that are illuminated by laser can be calculated by the geometrical equations after the calibration. If the image plane is divided into two planes from the center pixels, hollows would be detected on the downside whereas the obstacles would be detected on the upside plane.

The lateral distance between the laser emitter and the camera sensor, the angles of the laser line and optical axis with respect to the ground level, the height of the camera sensor and *the laser emitter* are the parameters that must be determined at first. The height and angle of the laser emitter is related to the interested area in front of the lunar micro-rover as well as the camera sensor parameters. Since the CCD camera has an angle with the ground plane, it would see the front view with a perspective; therefore, the width of the observed area would increase with distance from the micro-rover. Hazard detection configuration is represented in Figure 5.8.

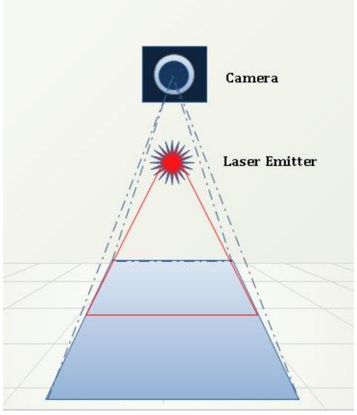

Figure 5.8 : Hazard detection configuration.

There is a linear relationship between the distance of an object and the position of its projection on the image plane when lighted with a laser line, and this relation can be used to calibrate the active laser triangulation system. Two different known distances have to be determined and measured on the image plane. The parameter *p* would be the pixel number of the measured reflection where the parameter *x* would be the distance of the object relative to the optical axis of the camera sensor [29].

$$\mathrm{X_{unknown}} = \frac{(\mathrm{p_1} - \mathrm{p_2})\mathrm{x_1 x_2}}{\mathrm{p_{detected}}(\mathrm{x_2} - \mathrm{x_1}) - (\mathrm{p_2 x_2} - \mathrm{p_1 x_1})} \quad [29] \tag{5.2}$$

For obstacle detection:

$$r_1 = \frac{x_2 - x_1}{\cos(\emptyset - \alpha)} = \frac{x_2 - x_1}{\cos\varphi} \tag{5.3}$$

$$h_1 = \frac{x_2 - x_1}{\cos(\emptyset - \alpha)}\, sin\alpha = \frac{x_2 - x_1}{\cos\varphi}\, sin\alpha = r_1 sin\alpha > 0 \tag{5.4}$$

$$\begin{aligned} d_1 &= x_1\, cos\emptyset - \frac{x_2 - x_1}{\cos(\emptyset - \alpha)}\, cos\alpha = x_1\, cos\emptyset - \frac{x_2 - x_1}{\cos\varphi}\, cos\alpha \\ &= x_1\, cos\emptyset - r_1 cos\alpha \end{aligned} \tag{5.5}$$

For hollow detection:

$$r_2 = \frac{x_3 - x_2}{\cos(\emptyset - \alpha)} = \frac{x_3 - x_2}{\cos\varphi} \tag{5.6}$$

$$h_2 = \frac{x_3 - x_2}{\cos(\emptyset - \alpha)}\, sin\alpha = \frac{x_3 - x_2}{\cos\varphi}\, sin\alpha = r_2 sin\alpha\; < 0 \tag{5.7}$$

$$d_3 = x_2\,cos\emptyset + \frac{x_3 - x_2}{\cos(\emptyset - \alpha)}\,cos\alpha = x_2\,cos\emptyset + \frac{x_3 - x_2}{\cos\varphi}\,cos\alpha$$
$$= x_2\,cos\emptyset + r_2 cos\alpha \qquad \textbf{(5.8)}$$

For the hazard detection system, the angle parameters are constant; however, the angle of α changes if the system is used for mapping. It is represented in Figure 5.9, and the flowchart is given in Figure 5.10.

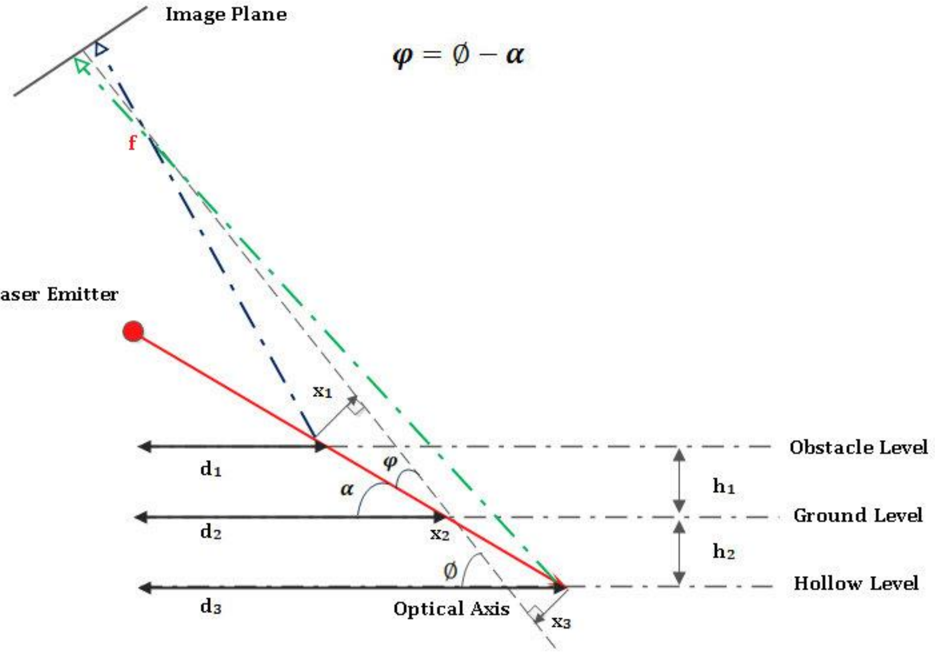
Image Plane
$\varphi = \emptyset - \alpha$
f
Laser Emitter
x1
Obstacle Level
d1
φ
α
h1
Ground Level
d2
x2
h2
$\emptyset$
Hollow Level
d3
Optical Axis
x3

Figure 5.9 : Hazard detection configuration and parameters.

Hazard Detection and Mapping Algorithm Steps

1. Opening and checking laser stripe
2. Taking image of the scene with laser emitter on
3. Image processing; taking the red scaled image from the RGB color image
4. Finding the red pixels and saving pixel rows and columns
5. Triangulation process to detect the height and distances
6. Detect possible hazards for obstacles and hollows by checking wheel and body areas differently
7. Interruption of the rover movement or safe signal to continue
8. 3D reconstruction of the scene
9. Updating the previous map
10. Store the current map and update the rover position
11. Return to Step 1

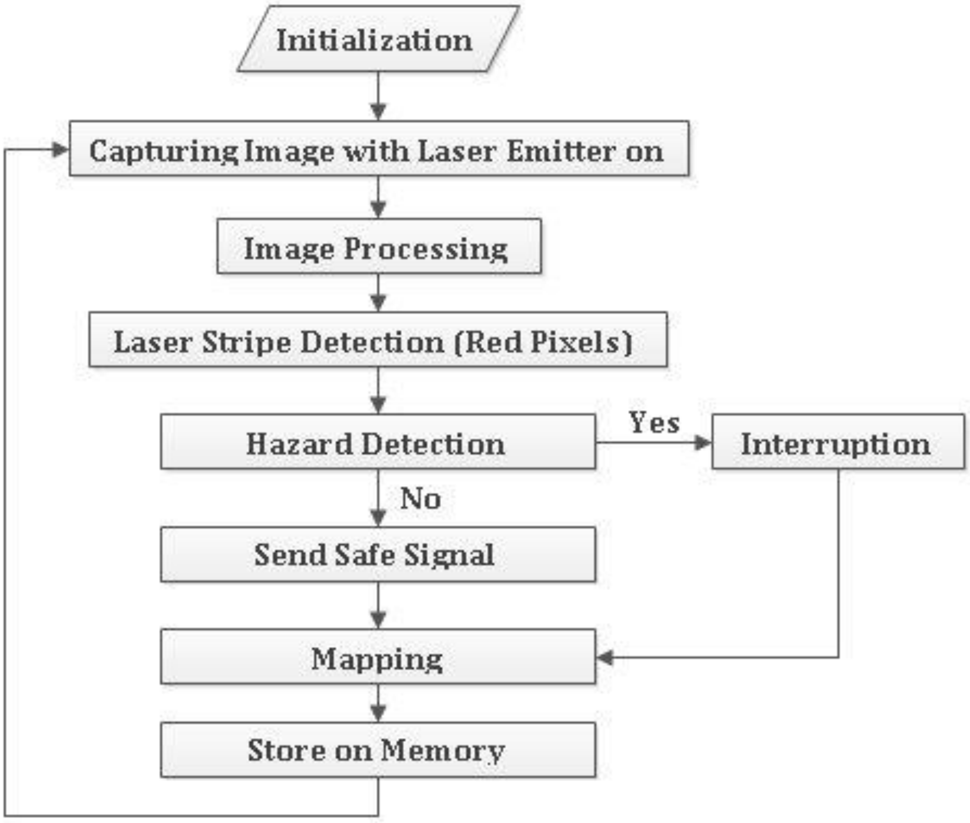
Initialization
Capturing Image with Laser Emitter on
Image Processing
Laser Stripe Detection (Red Pixels)
Hazard Detection
Yes
Interruption
No
Send Safe Signal
Mapping
Store on Memory

Figure 5.10 : Hazard detection and mapping algorithm flowchart.

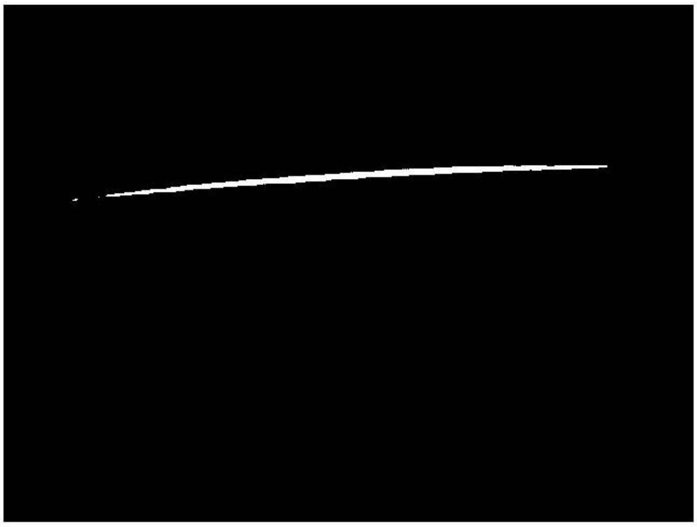

Figure 5.11 : Rough laser stripe emitting on the scene.

A simple laser line is used to represent the illuminated surfaces of a hollow by the laser emitter in Figure 5.11. Figure above shows the detected red color pixels of a red-scaled image, and the laser line is on the top half of the image plane as expected. Then, 3D reconstruction of the scene is made by using the written code to show the sensed depth of the hollow. An example is given in Figure 5.12.

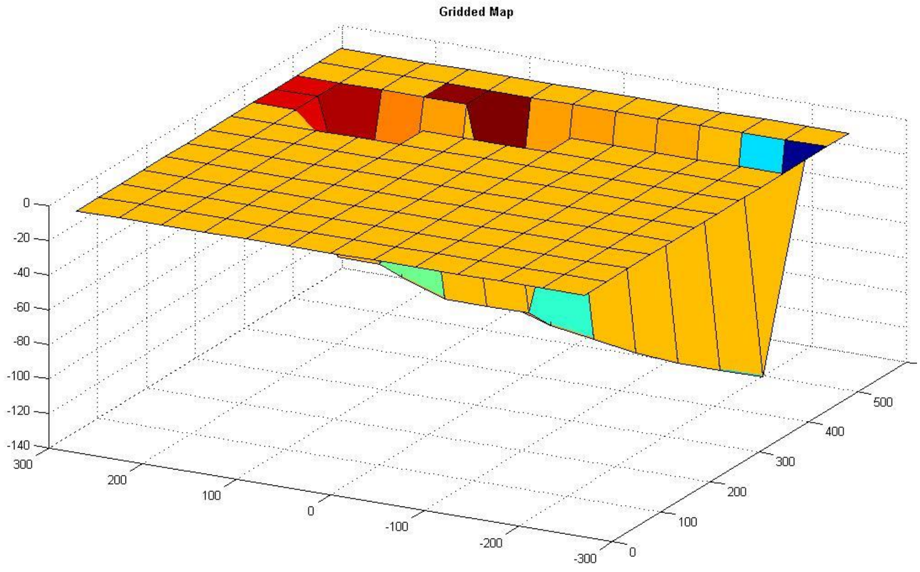

Figure 5.12 : Rough hollow detection example on the scene.

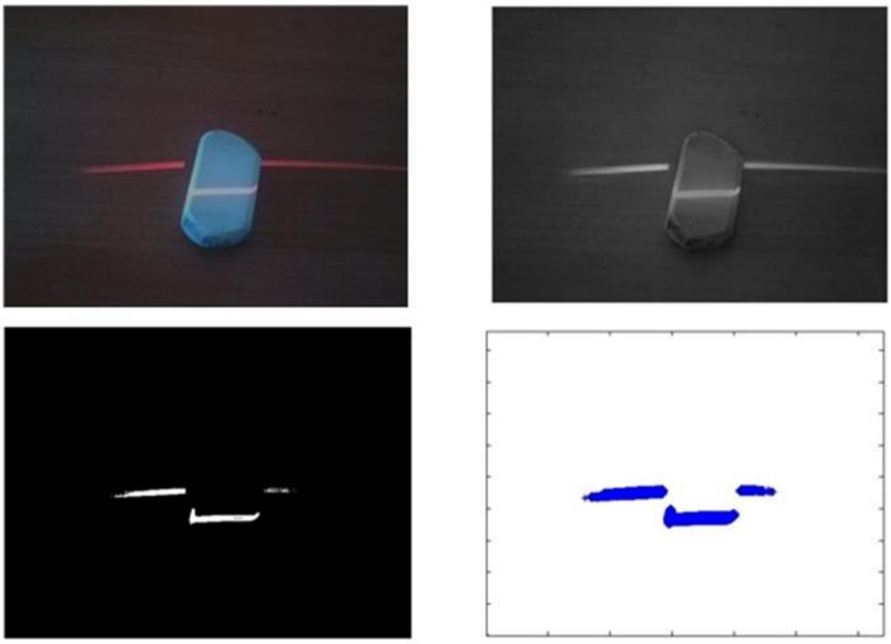

Figure 5.13 : Rough elevation detection example.

A simple eraser in Figure 5.13 above is used to see if the written code can sense and represent the illuminated surfaces by the laser emitter. The image shows the red-scaled image of the scene, and then the program detects the red color pixels. The last image shows the plot of the sensed pixels to show how the final works. The plot shows the laser lines thicker than the actual since the plot element is chosen dots denser than the actual pixel size.

5.3.2 Surface Mapping

Mapping can be described as visualization of surface features by using data from the active laser triangulation system. The depth information from the taken image is used to interpret the distance and pose of the certain features, and the accuracy of the information is dependent on the active laser triangulation system directly. An example is represented in Figure 5.14. Each measurement can be used to update the main map around the lunar micro-rover systematically since the micro rover need information about its surroundings to find a path to reach its goal destination.

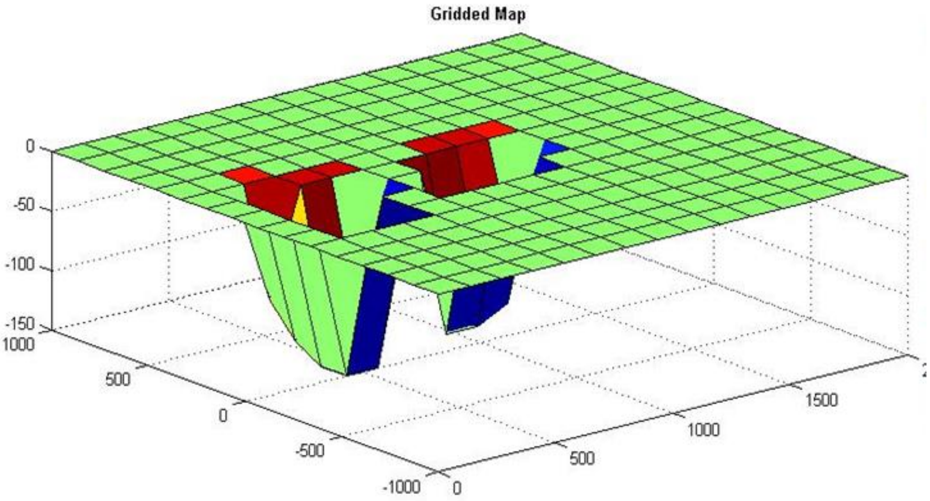

Figure 5.14 : 15 x 15 gridded main map example.

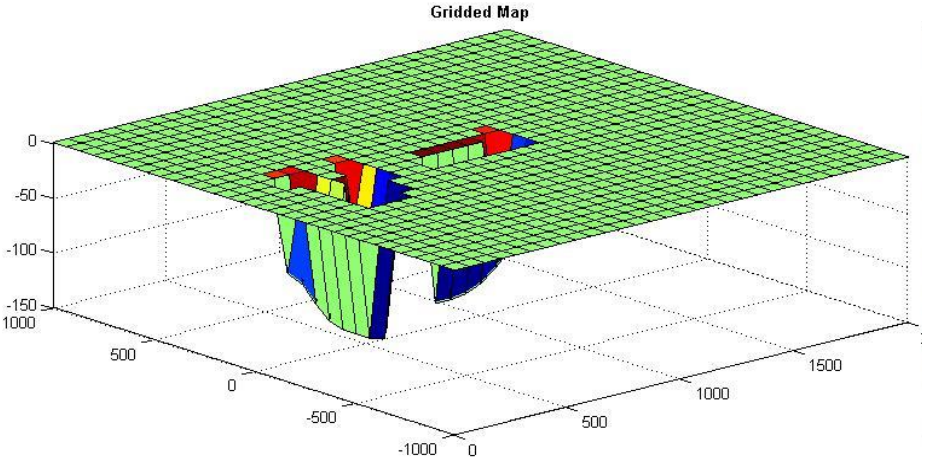

Figure 5.15 : 30 x 30 gridded main map example.

A Matlab code has been written to create a main map in order to be updated by using each measurement, and the surrounding of the LMR has been chosen as 2 m x 2 m.

The map updating code uses image space data as the taken measurement is used with its *x* and *y* coordination and its angle *θ.* This information is converted with respect to the reference frame, and it is used to update the image space data according to the pose, which can be seen in Figure 5.16 below.

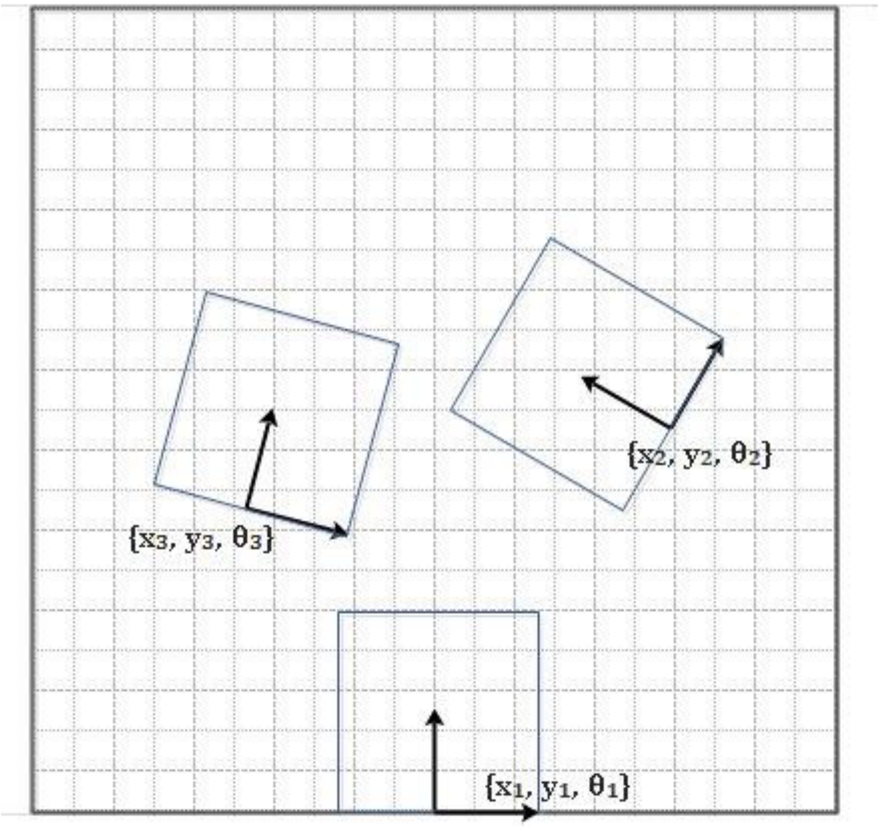

Figure 5.16 : Main map updating representation.

Each measurement would add new information on the surrounding of the micro rover, and this information would help to find an optimal path as well as to avoid hazards and obstacles.

The main map-updating algorithm uses a transformation with respect to the reference frame where an initial pose and goal destination can be represented. There are some parameters, which Matlab code uses while creating the 3D reconstruction of the image data around the micro rover:

- *Grid numbers in x-y plane*
- *The width and length of the main map*
- *The reference height from the initial pose*

When the grid numbers are increased into a certain amount, the features of the surface geometry are preserved more accurately, which can be seen in the Figure 5.14 and 5.15; however, it would increase the response time of the overall algorithm including the path planning. To increase the performance, the grid numbers could be limited in an optimum point where the features of the surface geometry will be retained in an efficient extent. On the other hand, the width and length of the main map are other parameters that would affect the performance of the system. The optimum grid number is highly related to them, and these parameters would be determined during the experiments by evaluating the performance.

5.4 Path Planning

5.4.1 Introduction

In robotics, path planning is the process of arranging a desired movement task from an initial position to a goal position with considering obstacles, robot size and kinematic limitations by optimizing some determined criteria such as time, energy consumption etc. For instance, navigating a mobile robot on a rough terrain or inside a building to a goal position is a path-planning problem. It should use its sensors to observe its environment or a given map to decide its movements.

Lunar micro rover will be working in unknown and rough terrain, or with minimum knowledge of its surroundings. A key functionality required for being able to perform certain tasks; therefore, it requires navigational autonomy. The mapping algorithm will be updating surrounding characteristics and keeping it in the memory in a certain extent. If available memory is low, it will delete the most distant terrain information relative to the LMR position. The micro rover must use its sensors to navigate safely and autonomously to the desired position, and while the LMR moves to the goal position according to main map or global map, it needs to correct its trajectory according to surrounding objects, obstacles and hollows.

Path planning algorithms for planetary rovers have several key characteristics such as [30]:

- Considering no prior knowledge of the surroundings
- Being sensor-based

- Being robust, complete and correct

Additionally, they must be performing their tasks under some constraints of power, computational capacity and available onboard memory [30]. Therefore, the planned algorithm is being developed and enhanced considering this limitations. It must be noted that the path planning will be performed with incomplete information about the environment, and as seen in Figure 5.16, the LMR will observe its front side and update its main map and previously planned path.

Most of the path planning work can be classified in three main categories such as classic path planners, heuristic planners, and “complete and correct” sensor based path planners. Classic path planners assume complete knowledge of the surroundings, and they are complete where heuristic path planners generally based on a set of “behaviors”, and they are suitable for unknown environments; however, they are not guarantee reaching the goal will be achieved. The last category, which is sensor-based and complete, is the most suitable for the autonomous path planning [30].

In previous section, mapping algorithm is described as visualization of surface features by using data from the active laser triangulation system, and each measurement is used to update the main map around the lunar micro-rover. For path planning, each grid is used as a waypoint to be investigated to find a path to reach the goal destination. The path-planning algorithm is described in the next section.

5.4.2 Path Planning Algorithm Selection

One of the fundamental problems in path planning is navigating in a rough terrain and finding the optimal path to a goal position; however, there are many approaches to this problem, A* search is the most common and widely known algorithm.

Nils Nilsson proposed a heuristic approach for Shakey the Robot to navigate through a room with some obstacles in 1968, which was a faster version Dijkstra’s algorithm to find the shortest path in graphs [31]. A* search algorithm uses a best-first search and follows the path with the minimum cost or distance. While it preserves alternate path branches in the memory if one of the segments have a lower cost than the current path, it switches from the present one to that segment with lower cost.

A*search algorithm uses the distance between the initial location of the LMR and the goal position. Then, it moves to the waypoint that has the smallest distance. Therefore, identifying the successor waypoint is the key in this method. The LMR's mapping method uses a 3D grid map to represent its environment; therefore, the cost function must be chosen as the Euclidean distance between two points. The Euclidean distance formula can be written as:

$$d(a,b) = \sqrt{(a_1 - b_1)^2 + (a_2 - b_2)^2 + \cdots + (a_n - b_n)^2} \qquad \textbf{(5.9)}$$

The total cost function f(n) is the sum of two functions which are the past path-cost function, and future path-cost function. The past path-cost function g(n) can be described as the sum of the known cost from the starting node to the current node n, in other words, it is the sum of the known costs between each nodes in the currently planned path. The future path-cost function is an estimate of the distance from node n to the goal position.

$$f(n) = g(n) + h(n) \qquad \textbf{(5.10)}$$

$$h(n) \leq h(n+1) + d(n, n+1) \qquad \textbf{(5.11)}$$

The future path-cost function must be an admissible heuristic that means it cannot estimate the cost to the goal more than its actual value. This can be shown as in Figure 5.17 below.

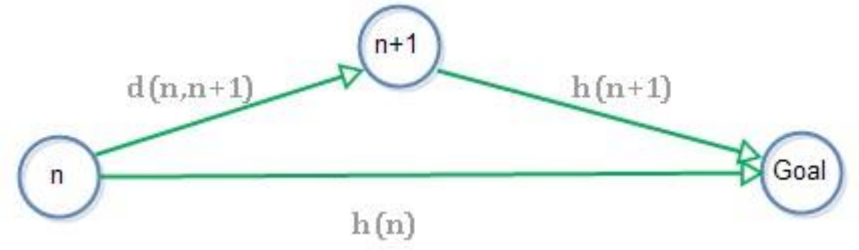

Figure 5.17 : The future path-cost function representation.

It is seen that the time, which is required to find the path between two given points, increases exponentially with the number of nodes. Moreover, the required memory also increases since the algorithm saves all nodes and branches.

The first step in the algorithm is loading map data to the workspace to use in the path-planning algorithm. The information of outside of the LMR's field of view is kept in memory, and the map data is implemented in the algorithm as 2D grid, which shows the coordinates of the nodes and the height values corresponding to those nodes. When the LMR uses its active laser triangulation system and captures an image, the LMR's field of view is updated in the image space. Then, the updated image space is used to reconstruct a new 3D map. If the captured image is used to create a local map, and then it is used to update the current map, the new nodes cannot match the main map's nodes certainly. Therefore, the image space must be updated first in mm metric, and then the main 3D map must be updated.

To navigate the LMR through the reconstructed 3D map, the model must consider the physical properties of the LMR and the kinematic limitations such as its size and ability to rotate. The LMR design has an ability to rotate around its central axis. However, the A* search algorithm does not account neither the physical size of the robot nor its mobility [32]. Therefore, the first step is to check the height values corresponding to each node, and then classify them as obstacles according to the LMR's traversing ability.

The width of the obstacles is extended to consider the LMR as a particle on the map as suggested in [32-35]. Therefore, the obstacle detection and extending function is written and implemented in the algorithm, which considers the size of the LMR and a determined clearance between an obstacle/hollow and the LMR, before the path planning is performed. Figure 5.18 shows the 3D map for the obstacle and hollow detection example, and Figure 5.19 shows the detected nodes before extending for safety. Finally, Figure 5.20 is the extended nodes of the hollows from the example map.

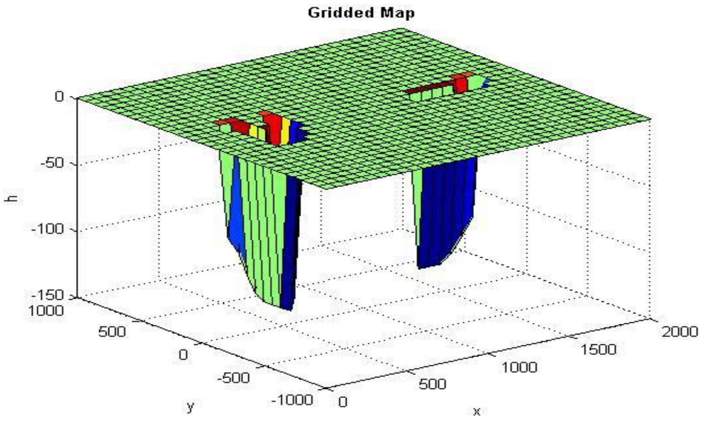

Figure 5.18 : 3D map example for obstacle and hollow.

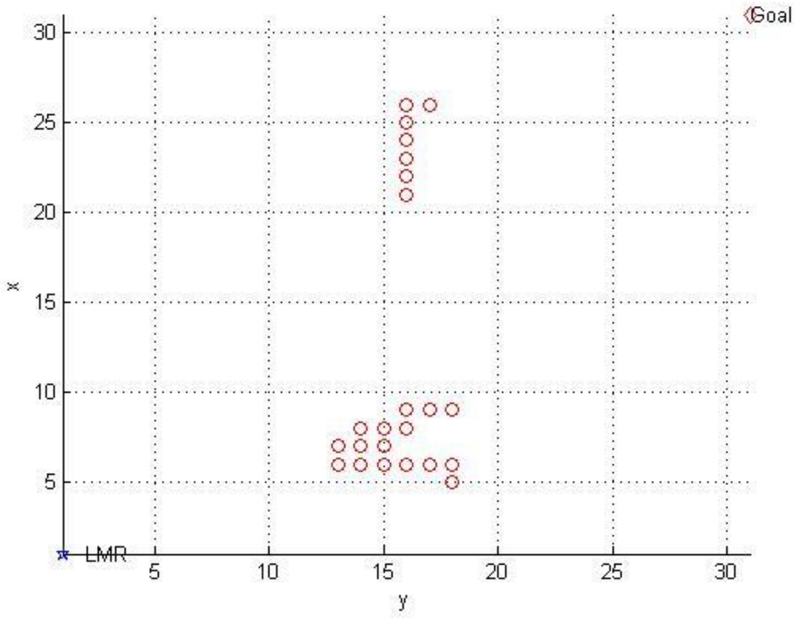

Figure 5.19 : The detected nodes of hollow for possible hazards.

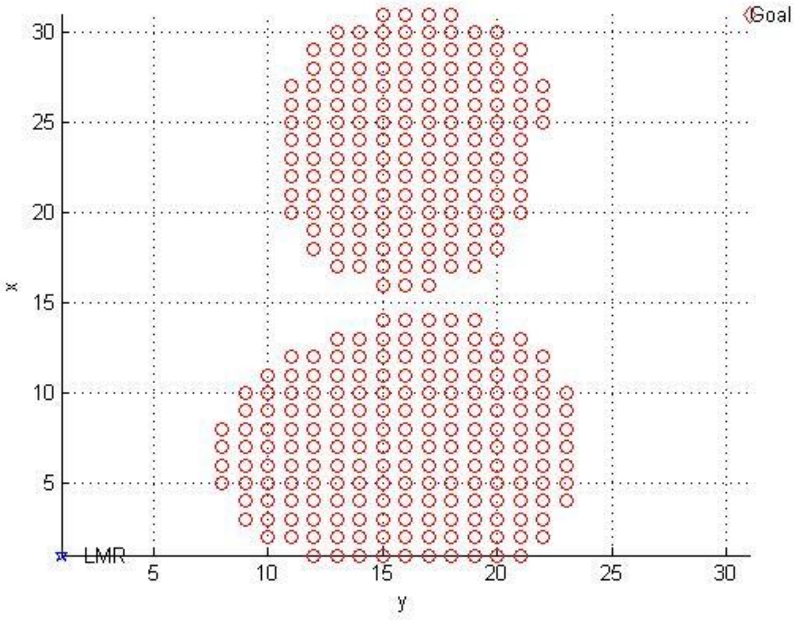

Figure 5.20 : The extended nodes of hollow for possible hazards.

The first written algorithm before A* search was quicker to response; however, it does not give the optimum result which can be seen in Figure 5.21. It used a greedy search, which takes minimum cost value between the nodes into account instead of the total cost from the start position and to the goal position. It uses a heuristic for making locally optimal choices at each stage; however, it was stuck in loops in some situations.

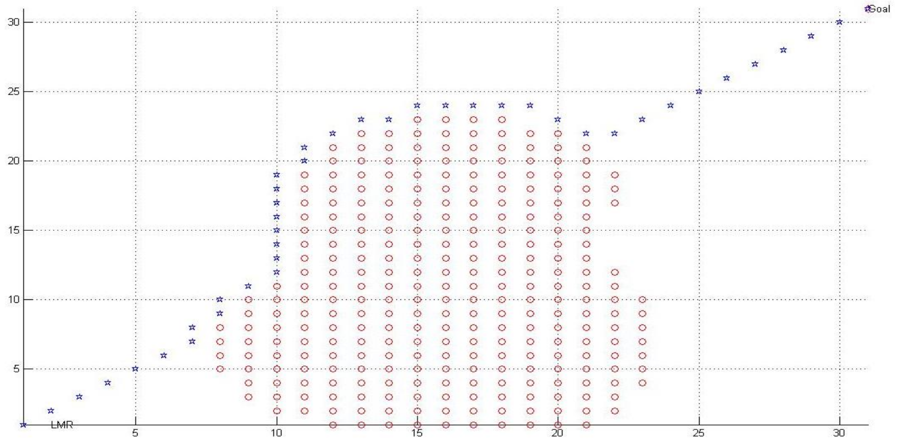

Figure 5.21 : The first algorithm with greedy search.

The LMR tended to head directly to the goal position instead of the top left corner of the hollow nodes, and the planned path is not optimum as it is seen in Figure 5.21 since it calculates the total cost function by summing the Euclidean distance from the initial position and the Euclidean distance to the goal position for each sub-node candidate. In addition, greedy search algorithm was stuck in loop for the second example, it is observed it switched between two nodes as expected, and it was not able to reach the goal. Even though the first algorithm is faster to response, it is not suitable for a lunar micro rover considering the power consumption and time as well. This is the reason why a variant A* algorithm is chosen to be implemented.

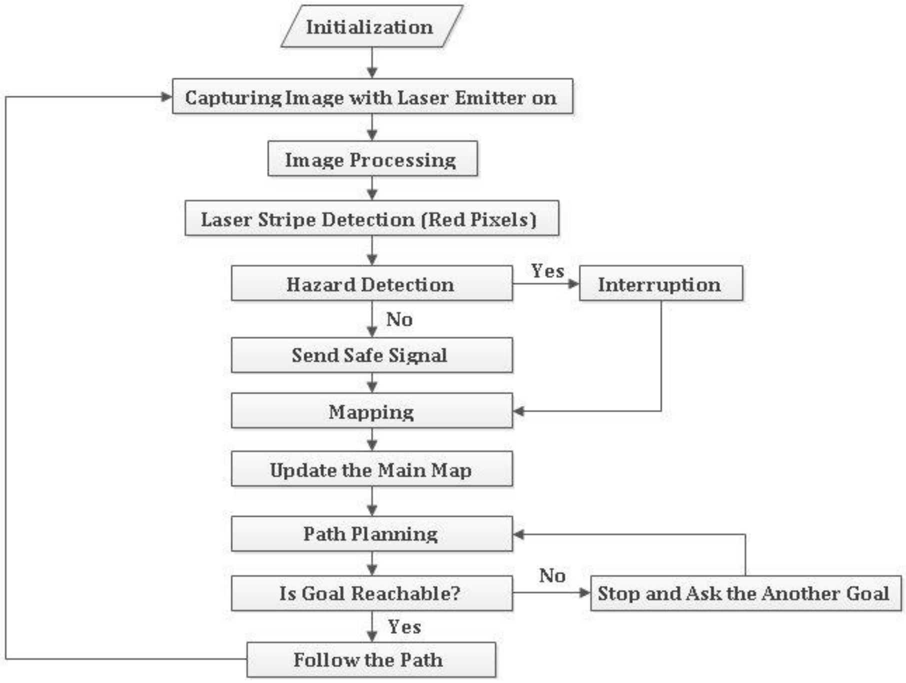
Initialization
Capturing Image with Laser Emitter on
Image Processing
Laser Stripe Detection (Red Pixels)
Hazard Detection
Yes
Interruption
No
Send Safe Signal
Mapping
Update the Main Map
Path Planning
No
Is Goal Reachable?
Stop and Ask the Another Goal
Yes
Follow the Path

Figure 5.22 : Path planning and mapping algorithm flowchart.

The Path Planning Algorithm Steps

---

1. Load the updated 3D map
2. Classify possible obstacle and hollow nodes for hazard detection
3. Expand the detected nodes of the obstacles and hollows
4. Add the expanded nodes into ineligible list
5. Request the initial position of the LMR in x and y axis
6. Request the goal position in x and y axis
7. Plot the detected hazard nodes, the initial position of the LMR and the goal position
8. Check if the initial position node is the goal position
   If YES: Stop the algorithm and report
   If NO: Continue
9. Put the start node on the path list
10. Determine the sub-nodes from eligible list
11. Check the sub-nodes if one of them equal to the goal
    If YES: Stop the algorithm and report the path
    If NO: Continue
12. Calculate h(n), g(n) and f(n) for each sub-node and add them into the path list
13. Find the sub-node with the minimum f(n) value
14. Add previous node(s) to ineligible list for sub-node selection
15. Return to Step 10

As it is seen in the path planning algorithm steps, the written code loads the reconstructed 3D map to the Matlab workspace at first. Then, it classifies possible obstacles and hollow nodes for hazard detection and expands them. After plotting those nodes in red color on a gridded plot, it requests an initial position for the LMR and the goal position. The next step for the path planning is to check whether the initial position and the goal position are equal, and according to that, the algorithm will continue to perform. The ineligible list is created before sub-node candidate selection, and the total costs of sub-node candidates are calculated by the Euclidean distance function. According to those values, sub-node is chosen with the minimum cost.

By checking whether the sub-node is equal to the goal position, the algorithm decides to stop and report or continue performing. If another sub-node is found to be with minimum total cost in the next loop, a new branch is added to the path candidates while the previous one is preserved in the memory. It can be seen that the number of the nodes increases the path candidates to be kept in the memory, which leads to increase in the required memory space exponentially. Unless the available memory is present, the algorithm will delete the path candidate with minimum potential, which has the highest total cost function. The comparison is given in Table 5.2.

Table 5.2 : Comparison of greedy search and a* search algorithms.

Greedy Search Algorithm	A* Search Algorithm
Quicker to response	Slower to response
Incomplete	Complete
Requires less memory space	Requires more memory space
Not Optimal	Optimal

If a graph search algorithm always returns an optimal solution, it is admissible since it chooses the path with the lowest cost (if a solution is present to reach the desired position). On the other hand, A* search algorithm is only admissible if the heuristic h(n) never over-estimates the distance to the goal, which is represented in Figure 14. Therefore, A* search algorithm not only finds a path, if a path exists at all, it also finds the optimal solution with the minimal cost.

At first, A* search algorithm is used to find a path between two points with the node coordinates [10, 10] and [20, 20] to check from the plot since the shortest; therefore the optimum path between two points is a straight line as in Figure 5.23.

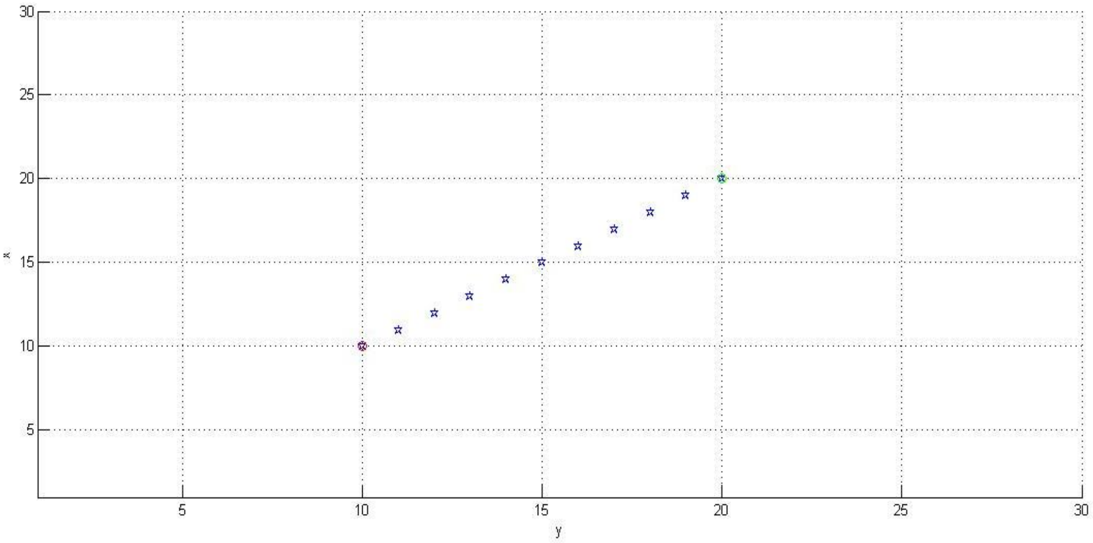

Figure 5.23 : A* search algorithm between two points without any obstacles.

After checking A* search algorithm between two points without any obstacles, more complex path planning tasks are performed to see the performance of the written algorithm. The next Figures are shown to illustrate different tasks.

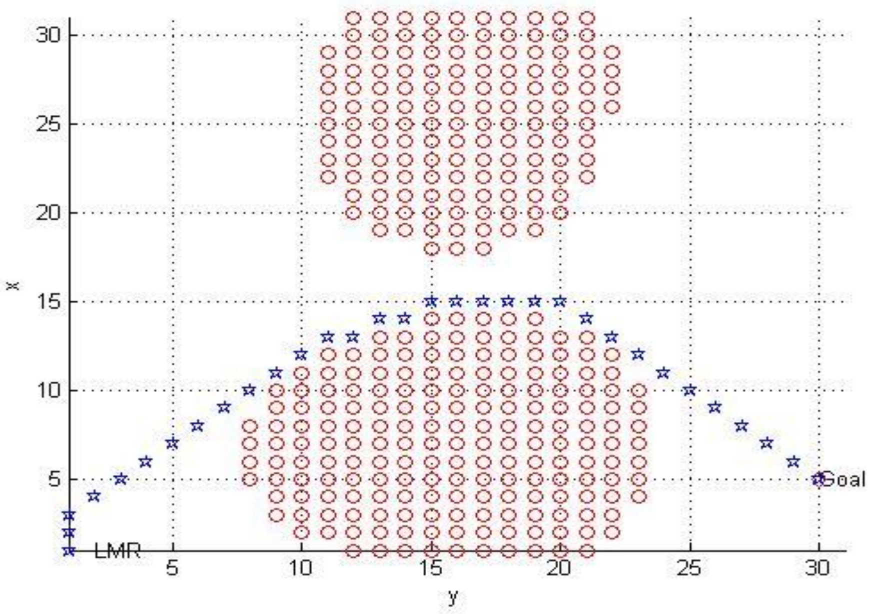

Figure 5.24 : A* search algorithm between two points with obstacles.

Ineligible nodes from the hollows are placed closer in the next task, and the algorithm was able to find its optimal path through a small open area in Figure 5.25.

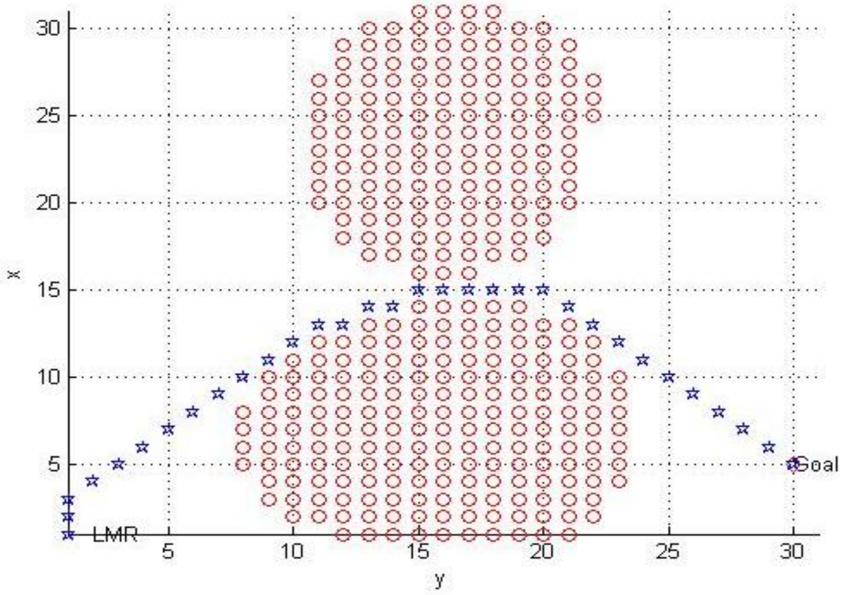

Figure 5.25 : A* search algorithm between two points with denser obstacles.

The next task was chosen as path planning from an initial position to an unreachable goal; therefore, the obstacle nodes are placed closer and surrounded the start position of the LMR. The A* search algorithm investigated all nodes available in the right bottom area in the map (Figure 5.26); however, it stopped performing after no eligible sub-node candidate was available.

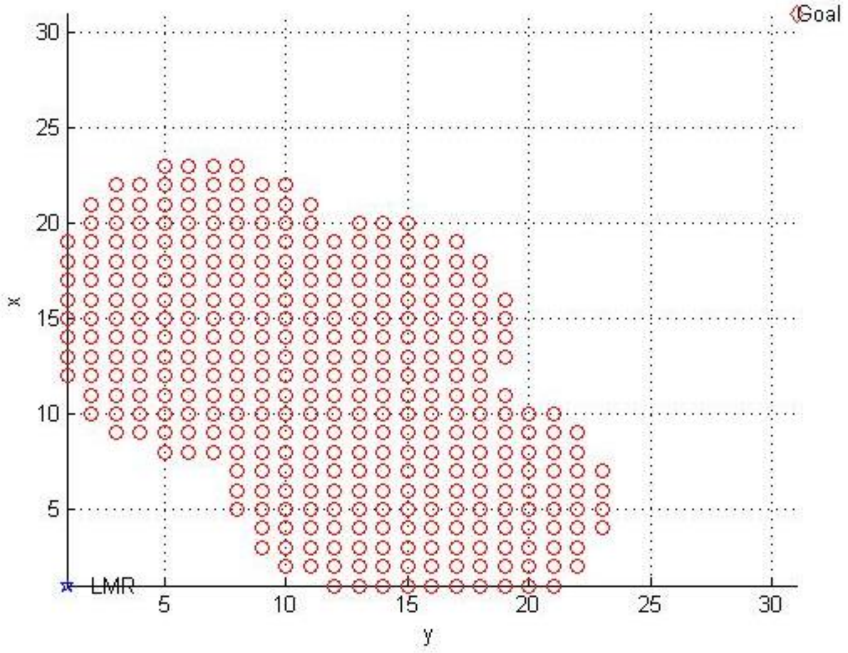

Figure 5.26 : A* search algorithm for unreachable goal destination.

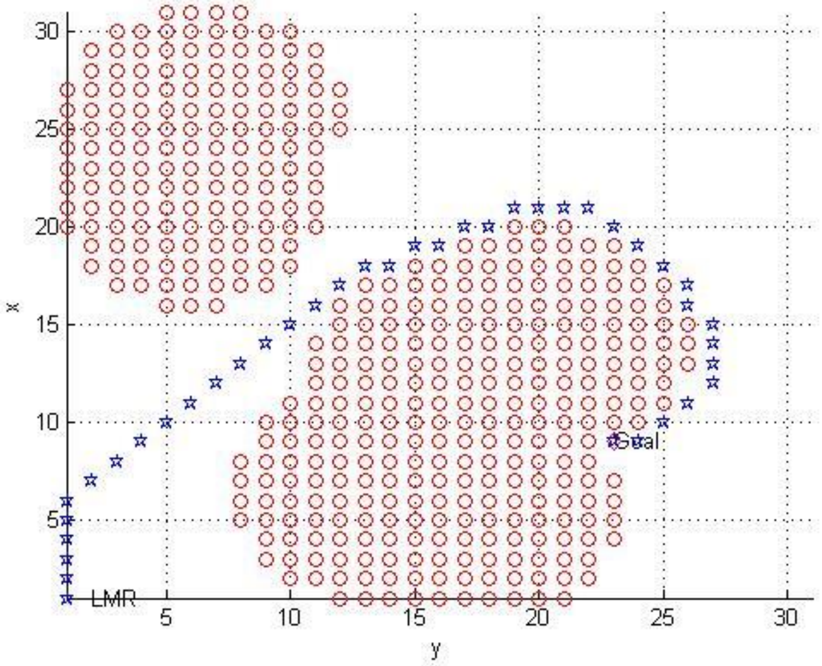

Figure 5.27 : A* search algorithm task example.

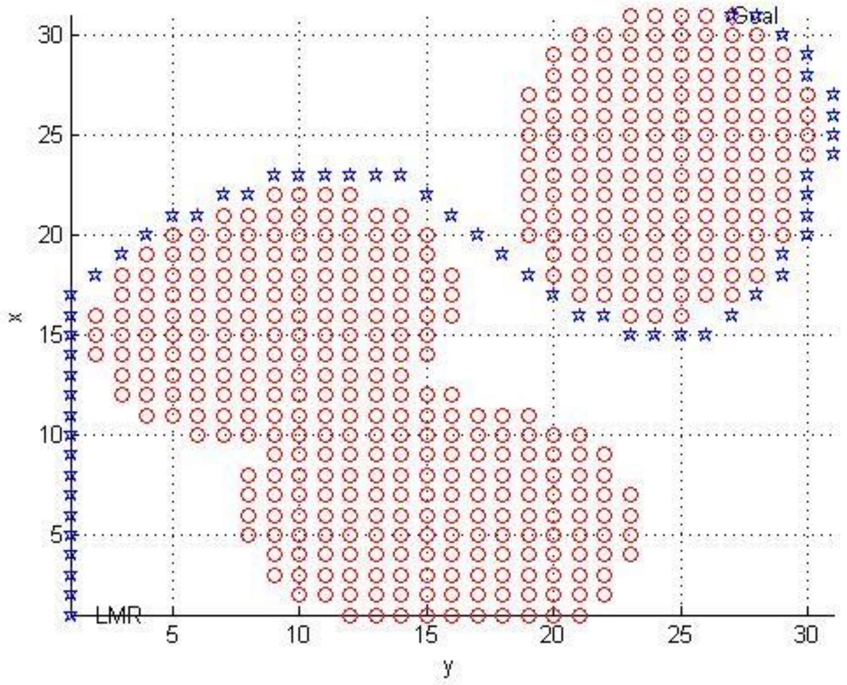

Figure 5.28 : A* search algorithm task example.

The final tasks are illustrated in Figure 5.27 and 5.28, which the first written algorithm failed to perform and stuck in infinite loops when reached at [2, 9], [1, 10] or [1, 11]. On the other hand, A* search algorithm found the optimum path successfully.

5.5 Conclusion

According to the velocity of the LMR, it should be able to plan its path in real-time while the robot observes and map its surroundings while it evades sensed obstacles and hollows for safety and reliability. Active laser triangulation system is expected to be sensitive to noise; hence mapping and path planning algorithm; however, it will be optimized after implementation to the LMR when it is built within our faculty. In addition, active laser triangulation system operates by sensing the reflected red laser from a surface from the red color pixels on the captured image; however, the ambient light variations and the reflectance properties of different surfaces are the main challenges of the system. The ambient light variations are expected to be overcome by using optical filters according to the wavelength of the laser emitter to be used in outdoor environments more accurately.

Active laser triangulation system is desired to be low-cost, low power consuming while having high response speed and high sampling frequency, and it will be used for detecting hazards and mapping the rough terrain.

Following a determined path around an obstacle or a hollow is a common feature of the previous example tasks. It is not a problem in the absence of noise and uncertainties; however, it will be used to measure the performance of the LMR's navigation and path planning system. Then, further optimizations will be performed, and adding stereovision system to the LMR is expected to increase overall performance.

When the LMR uses its active laser triangulation system and captures a new image, the LMR's field of view is updated in the image space. The information of outside of the LMR's field of view is kept in memory, and the map data is implemented in the algorithm as 2D grid, which shows the coordinates of the nodes and the height values corresponding to those nodes. Then, the updated image space is used to update 3D main map. The LMR's field of view will be updated on the main map, and the rest information will be preserved in the memory unchanged. If the captured image is used to create a local map, and then it is used to update the current map, the new nodes cannot match the main map's nodes certainly. Therefore, the image space must be updated first in mm metric, and then the main 3D map must be updated.

The mapping and path planning algorithm considers solely 2D rotation of the LMR; hence the field of view. In the real system, it will use height of the robot's position relative to the reference level, and the orientation data from an onboard inertial measurement unit (IMU) sensor.

Higher grid number represents the surface geometry more accurately; however, it requires longer response time; hence the path planning and obstacle detection. The width and length of the main map and the determined grid number in x and y planer must be kept in the optimum value while considering the response time and available memory capacity of the LMR.

Finally, greedy search algorithm and A* search algorithm is implemented in the main algorithm to compare their performance. Different tasks are given to the path planning algorithms, and if there are no obstacles or hollows, which the robot cannot overcome, both algorithms found the reasonable path. On the other hand, the complication level is increased for the tasks, and A* search algorithm found the optimal path each time, if it exists at all. Therefore, A* search is chosen as the path planning algorithm instead of greedy search.

6. CONCLUSION AND RECOMMENDATIONS

The LMR is designed to be a lightweight platform with high mobility, resistant to high radiation, extreme temperature variations, lunar dust etc. In design process, the most important considerations were mobility and weight limitations. The mass and inertia properties are derived from Solidworks after material selection. In addition, the energy limitations require actuators to be chosen those consume very little power since there will be limited electrical power from solar panels. Onboard computer and battery is expected to keep the electronics warm in order to operate in low temperature. The body structure is designed to have low volume; however, it provides sufficient space for the onboard computer, scientific instruments, actuators, cameras, sensors etc.

The main objective is to obtain a surface sample from the Moon and store it within the micro rover to study in mini laboratory, which is expected to be on the top of the LMR. The sample is desired to have a volume between 1-3 cm^3; therefore, the arm tool is designed based on a handling mechanism; however, this tool can also be replaced with a drill mechanism for subsurface sampling. The main interest of the research is chosen as investigating the ejecta areas on the lunar surface containing both meteor samples as well as Moon’s own material. The primary technologies to be implemented within the LMR are chosen as local mapping, manipulation and sample handling, and path planning.

At the beginning, the design of the LMR was chosen as a 6-wheel system with a rocker-bogie suspension, which has a mechanism as passive rotary joint to attach two links called rocker and bogie. As wheels are free to move up and down on an uneven terrain with the rotary joint, each wheel carry the weight of the LMR equally, but it is much heavier than a 4-wheel suspension, and each extra actuator means more energy consumption and higher hardware requirements. Further considerations and trade-off work lead the design to have a 4-wheel suspension.

The surface sampling activities will be commanded from Earth during the communication windows while the instruments within the mini laboratory analyze samples, and data of the environmental properties such as radiation, ionization, temperature will be gathered as well. The formal mission lifetime is expected to be couple of months if the LMR survives the lunar night. The first phase of the mission will contain primary scientific activities and measurements before the lunar night period; therefore, if the LMR does not survive the lunar night, it will gather and transmit data before it malfunctions.

By only giving input for the links' motions, the joints' torques are derived for the given system, and for the poses, which robotic manipulators cannot reach, the singularity of the Jacobian matrix is observed. In addition, a closed-form dynamic model is obtained which the same to the one is obtained by using DH parameters. The effect of Moon and Earth's gravity ratio is observed in the torques. Since the robotic arms' motion is determined to be slow, Coriolis effect is not strong. Moreover, the profiles of the both torque graphs seem to be very similar; however, the magnitude of the torque's ratio is very close to the ratio of the gravity, which is approximately 1/6.

Active laser triangulation system operates by sensing the reflected 670 nm wavelength radiation laser from a surface from the red color pixels on the captured image; however, the ambient light variations and the reflectance properties of different surfaces are the main challenges of the system. It is desired to be low-cost, low power consuming while having high response speed and high sampling frequency, and it is used for detecting hazards and mapping the rough terrain.

When the LMR uses its active laser triangulation system and captures a new image, the LMR's field of view is updated in the image space. The information of outside of the LMR's field of view is kept in memory, and the map data is implemented in the algorithm as 2D grid, which shows the coordinates of the nodes and the height values. Then, the updated image space is used to renew reconstructed 3D main map. The LMR's field of view is update, and the rest information is preserved in the memory unchanged.

Greedy search algorithm and A* search algorithm is implemented in the main algorithm to compare their performance. Different tasks are given to the path planning algorithms, and if there are no obstacles or hollows, which the robot cannot overcome, both algorithms found the reasonable path. On the other hand, the complication level is increased for the tasks, and A* search algorithm found the optimal path each time, if it exists at all. Therefore, A* search is chosen as the path planning algorithm instead of greedy search.

The next step for this project is to build prototype for verification of the performance and to have a micro-rover platform to work on within our faculty. A passive triangulation system such as stereo-based planner is a reliable choice, and it will be added to the LMR in the future; however, it cannot detect craters and shadows whereas active laser triangulation system is successful. Further investigation on radiation shielding for the LMR will be done according to the environment conditions, it is currently expected to be a multi-layered radiation protection with high density and low-density materials.

REFERENCES

[1] **Buchanan, B.G.** (2006). Brief History of Artificial Intelligence. AI Magazine Magazine AAAI. Vol. ***26***, no. 4 doi: http://dx.doi.org/10.1609/aimag. v26i4.1844.

[2] **Bekey, G., Ambrose, R., Kumar, V., Lavery, D., Sanderson, A., Wilcox, B., Yuh, J., and Zheng, Y.** (2008). Space Robotics. *Robotics: State of the Art and Future Challenges*. pp. 39-68 doi: 10.1142/9781848160071 _0 003.

[3] **Schafer, B., Leite, A.C., and Rebele, B.** (2011). Development Environment for Optimized Locomotion System of Planetary Rovers, *Proceedings of the XIV International Symposium on Dynamic Problems of Mechanics*, São Paulo, Brazil, March 2011**.**

[4] **Katy Levinson.** (2008). Lunar Micro Rover A Major Qualifying Project Report, BSc Thesis, Worcester Polytehnic Institute, USA.

[5] **Crawford, I. A., Anand, M., Cockelle, C. S., Falcke, H., Green, D. A., Jaumann, R., et al.** (2012). Back to the Moon: The Scientific Rationale for Resuming Lunar Surface Exploration. ESA. Planetary and Space Science**.**

[6] **Jaumann, R., Hiesinger, H., Anand, M., Crawford, I.A., et al. (21 authors in total).** (2012). Geology, Geochemistry, and Geophysics of the Moon: Status of Current Understanding. Planetary and Space Science. ***74***, 15-41 doi:10.1016/j.pss.2012.08.019.

[7] **De Rosa, D., Bussey, B., Cahill, J.T., Lutz, T., Crawford, I.A., Hackwill, T., Gasselt, S.V., Neukum, G., Witte, L., McGovern, A., Grindrod, P.M., and Carpenter, J.D.** (2012). Characterisation of potential landing sites for the European Space Agency's Lunar Lander project. *Planetary and Space Science*. Vol. ***74***, Issue 1, ppt: 224-246 doi:10. 1016/ j.pss.2012.08.002.

[8] **Saito, Y., Masaki, N. M., Yokota, S., Takaaki, T., Yamamoto, T., Asamura, K., et al.** (2011). Lunar Plasma Environment. In W. Liu, & M. Fujimoto (Eds.), The Dynamical Magnetosphere. Vol. ***3***, pp. 359-366. Kiruna, Sweden: Springer**.**

[9] **Yokota, S., Saito, Y., Asamura, K., Tanaka, T., Nishino, M. N., Tsunakawa, H., et al.** (2009). First direct detection of ions orginiating from the Moon by MAP-PACE IMA onboard SELENE (KAGUYA). *Geophysical Research Letters.* Vol. ***36***, Issue 11 doi: 10.1029/2009 GL038185.

[10] **Tanaka, T., Saito, Y., Yokota, S., Asamura, K., Nishino, M. N., Tsunakawa, H., et al.** (2009). First in-situ observation of the Moon-originating ions in the Earth's Magnetosphere by MAP-PACE on SELENE

(KAGUYA). *Geophysical Research Letters*. Vol: ***36***, Issue 22 doi: 10.1029/2009GL040682.

[11] **O'Brien, B.** (2008). Direct active measurements of movements of lunar dust: Rocket exhausts and natural effects contaminating and cleansing Apollo hardware on the Moon in 1969, *Geophysical Research Letters*. ***36***, L09201 doi:10.1029/2008GL037116**.**

[12] **Carpenter, J. D., Angerer, O., Durante, M., Linnarson, D., and Pike, W. T. ,** (2010). Life Sciences Investigations for ESA's First Lunar Lander, *Earth, Moon and Planets,* ***107,*** no. 1, pp. 11-23 doi: 10.1007/s11038-010-9375-y.

[13] **Taylor, L.A., Pieters, C.M., Keller, L .P., Morris, R. V., and McKay, D.S.** (2001). Lunar mare soils: Space weathering and the major effects of surface-correlated nanophase Fe, *Journal of Geophysical Research*, ***106***, E11, pp. 27985-28000 doi: 10.1029/2000JE001402.

[14] **Zeynali, O., Masti, D., and Gandomkar, S.** (2012). Shielding Protection of Electronic Circuits Against Radiation Effects of Space High Energy Particles, *Advances in Applied Science Research*, Vol. ***3***, p. 446-551.

[15] **Kuroda, Y., Kondo, K., Nakamura, K., Kunii, Y., and Kubota, T.** (1999). Low Power Mobility System for Micro Planetary Rover Micro 5. *Fifth International Symposium on Artificial Intelligence, Robotics and Automation in Space.* pp.77-82, 1999.

[16] **Sciavicco L., and Siciliano B.** (1995). Modelling and Control of Robot Manipulators. 2nd Ed. UK London: Springer.

[17] **Brookes, M.** (2011). *The Matrix Reference Manual* [online]. Retrieved from: http://www.ee.imperial.ac.uk/hp/staff/dmb/matrix/intro.html.

[18] **Murray R.M., Li Z., and Sastry S. S.** (1994). A Mathematical Introduction to Robotic Manipulation. CRC Press. Retrieved from: http://www.cds.caltech.edu/~murray/mlswiki.

[19] **Rodriquez G., Kreuz, K. and Jain, A.** 1991. A Spatial Operator Algebra for Manipulator Modeling and Control. *International Journal of Robotics Research*. Vol. ***10***, pp. 371-381, August 1991.

[20] **Corke P.** (2011). Robotics, Vision and Control: Fundamental Algorithms in Matlab, Robotic Arm Kinematics (p.137-139). Chennai: Springer.

[21] **Karyot, T.B.** (2010). Introduction to Robotics Lecture Notes. ITU Faculty of Aeronautics and Astronautics

[22] **Yeşiloğlu, S.M.** (2014). Advanced Topics in Robotics Lecture Notes. ITU Faculty of Electrical and Electronic Engineering

[23] **Simmons, R., Henriksen, L., Chrisman, L., and Whelan, G.** (1998). Obstacle Avoidance and Safeguarding for a Lunar Rover, Proc. *AIAA Forum on Advanced Developments in Space Robotics,* Madison WI. August 1998.

[24] **Corke P. (**2011). Robotics, Vision and Control: Fundamental Algorithms in Matlab, Chapter 6: Localization (pp.108). Chennai: Springer.

[25] **Marques, L., Nunes, U., and Almeida, A.T.** (1998). A New 3D Optical Triangulation Sensor for Robotics. *5th International Workshop on Advanced Motion Control,* pp. 512-517 doi: 10.1109/AMC.1998.743589.

[26] **Gan., Z., and Tang, Q.** (2011). Visual Sensing and Its Applications: Integration of Laser Sensors to Industrial Robots. Chapter 1 Introduction: Laser Triangulation Sensor. (p.6). Chennai: Springer.

[27] **Mayer, R.** (1999). Scientific Canadian: Invention and Innovation from Canada's National Research Council. Vancouver: Raincoast Books. ISBN 1-55192-266-5. OCLC 41347212.

[28] **Labecki, P., Rosinski, D., and Skrzypcznski, P.** (2011). Terrain Map Building for a Walking Robot with an Active 2D Range Sensor. *Journal of Automation, Mobile Robotics & Intelligent Systems*, Vol. ***5***, no.3. pp. 67-78.

[29] **Thornton, T.** (1999). A Simple Laser Range Finder. *The Robot Builder*, Vol. ***11***, no. 6. Retrieved from: http://www.rssc.org/sites/default/files/newsletter/jun99.pdf.

[30] **Laubach, S.L., and Burdick, J.W.** (1999). An autonomous sensor-based path-planner for planetary microrovers. IEEE International Conference on Robotics and Automation(ICRA). Vol. ***1***, pp.347,354 doi: 10.1109/ROBOT.1999.770003.

[31] **Hart, P.E., Nilsson, N.J., and Raphael, B.** (1968). A Formal Basis for the Heuristic Determination of Minimum Cost Paths. *IEEE Transactions on Systems Science and Cybernetics*. Vol. ***4***, no.2, pp.100,107 doi: 10.1109/TSSC.1968.300136.

[32] **Otte, M.W., Richardson, S.G., Mulligan, J., and Grudic, G.** (2007). Local path planning in image space for autonomous robot navigation in unstructured environments, International Conference on Intelligent Robots and Systems (IROS). pp. 2819-2826 doi: 10.1109/IROS.2007.4399343.

[33] **Kolski, S., Ferguson, D., Bellino, M., and Siegwart**, **R.** Autonomous driving in structured and unstructured environments. *IEEE Intelligent Vehicles Symposium.* Lausanne, Switzerland & Pittsburgh, USA, 2006.

[34] **Sugiyama, M., Kawano, Y., Niizuma, M., Takagaki, M., Tomizawa, M. and Degawa, S.** (1994). Navigation system for an autonomous vehicle with hierarchical map and planner. *Proceedings of the Intelligent Vehicles '94 Symposium*. pp. 50 – 55 doi: 10.1109/IVS.1994.639469.

[35] **Kelly., A.** (1994). Adaptive perception for autonomous vehicles. Tech. Report CMU-RI-TR-94-18. The Robotics Institute, Carnegie Mellon University, 1994, unpublished.

CURRICULUM VITAE

Name Surname: Necmi Cihan Örger

Place and Date of Birth: İstanbul / 03.09.88

Address: Marmara Mah. Avrasya Cad. 115.Sok. Hanımeli Sitesi A2 Blok Daire: 34
Kat:8 Yakuplu, Beylikdüzü/İSTANBUL 34524

E-Mail: norger@itu.edu.tr

B.Sc.: Astronautical Engineering, Faculty of Aeronautics and Astronautics, Istanbul Technical University

M.Sc.: Astronautical and Aeronautical Engineering (interdis.), Faculty of Aeronautics and Astronautics, Istanbul Technical University

Projects and Theses:

- Solar Sail Deployment System and Plasma Measurement Instrument Designer of the Polar Bee Sail Project (September 2013 – Present)
- Responsible Student for Command and Data Handling subsystem of GaLactic Project Team (February 2012 – September 2012)
- Project GaLactic is designating for the Mission Idea Contest 2, which held by Japan Aerospace Exploration Agency (JAXA).
- Team member of UYARI CanSat Team, (January 2010 – June 2010)
  - ✓ CanSat Competition, All You Can Fly, Madrid, Spain – “Merit Awarded”
  - ✓ CanSat Competition – Texas, USA
- **Undergraduate Thesis:** A Symmetrical Robotic Arm Design Approach with Stereo-Vision Ability for CubeSats (JANUARY, 2013)
  Thesis Advisor: Assoc. Prof. Dr. Turgut Berat KARYOT
- **Master Thesis:** Design of Mobility and Control System of a Conceptual Lunar Micro-Rover (JANUARY, 2015)
  Thesis Advisor: Assoc. Prof. Dr. Turgut Berat KARYOT

List of Publications:

Örger, N. C., Özcan, B., Karyot, T. B. 2014. Gezici Mikro Ay Robotu Prototip Tasarımı, Ulusal Havacılık ve Uzay Konferansı, Ağustos 2014

Çay, Y., Örger, N. C., Kaymaz, Z. 2014. Güneş Yelkeni Ve Manyetik Yelken'in Uydu Teknolojisinde Kullanımı, Ulusal Havacılık ve Uzay Konferansı, Ağustos 2014

Örger, N. C., Karyot, T. B. 2013. A Symmetrical Robotic Arm Design Approach with Stereo-Vision Ability for CubeSats, 6th International Conference on Recent Advances in Space Technologies (RAST), July 2013

Öztürk, D. C. S., Bayar, M., Menteş, E., Gülbahar, Ö., Örger, N. C., Çay, Y., Salmanoğlu, E., Fiances, L. R., Aslan, A. R., Uzay Ortamında Fermentasyon İle Gıda Üretim Tekniklerinin İncelenmesi Ve Geliştirilmesi İçin Bir Nano-Uydu Tasarımı, Ulusal Havacılık ve Uzay Konferansı (National Aviation and Space Meeting), 2012.

Öztürk, D. C. S., Bayar, M., Menteş, E., Gülbahar, Ö., Örger, N. C., Çay, Y., Salmanoğlu, E., Fiances, L. R., Realization of Food Fermentation and Conservation Capability in Space (GaLactic), The 2nd Mission Idea Contest for Micro/Nano Satellite Utilization, 2012.

Accepted Abstracts:

Çay, Y., Örger, N. C., Kaymaz, Z., CubeSailSat to Study Polar Magnetospheric Environment, Asia Oceania Geosciences Society poster presentation, August 2014.

Örger, N. C., Çay, Y., Kaymaz, Z., Solar Sail Design for a Polar Orbiting CubeSat Science Mission, Asia Oceania Geosciences Society poster presentation, August 2014.

Certificates:

Certificate of Participation

CanSat Competition - Amarillo, Texas (June 2010)

Certificate of Merit

The 2nd Mission Idea Contest for Micro/Nano Satellite Utilization, Tokyo (June 2012)

Certificate of Attendance

The 6th International Conference on Recent Advances in Space Technologies, Istanbul (June 2013)

From Completed Coursera Courses:

- Control of Mobile Robots (March 2013, Georgia Institute of Technology)
- Astrobiology and the Search for Extraterrestrial Life (March 2013, The University of Edinburgh)
- Machine Learning (August 2013, Stanford University)
- Confronting The Big Questions: Highlights of Modern Astronomy (April 2014, University of Rochester)
- AstroTech: The Science and Technology behind Astronomical Discovery (July 2014, The University of Edinburg)